Two-Color Interferometry as a Fluctuation Diagnostic on Alcator C-Mod

by

Cale Phillip Kasten

B.S., Engineering Physics (2011)
University of Wisconsin-Madison

Submitted to the Department of Nuclear Science and Engineering
in partial fulfillment of the requirements for the degree of

Master of Science in Nuclear Science and Engineering

at the

MASSACHUSETTS INSTITUTE OF TECHNOLOGY

June 2013

Author .....
Cale P. Kasten
Department of Nuclear Science and Engineering
May 10, 2013

Certified by .....
Anne E. White
Assistant Professor
Thesis Supervisor

Certified by .....
James H. Irby
Principle Research Engineer
Thesis Reader

Accepted by .....
Mujid S. Kazimi
TEPCO Professor of Nuclear Engineering
Chair, Department Committee on Graduate Students

Two-Color Interferometry as a Fluctuation Diagnostic on Alcator C-Mod

by

Cale Phillip Kasten

Submitted to the Department of Nuclear Science and Engineering
on May 10, 2013, in partial fulfillment of the
requirements for the degree of
Master of Science in Nuclear Science and Engineering

Abstract

The two-color interferometer diagnostic on Alcator C-Mod has been upgraded to measure line-integrated electron density fluctuations for turbulence and transport studies. Heterodyne signals from ten vertical-viewing CO_2 laser chords are demodulated relative to a local oscillator using high bandwidth analog in-phase/quadrature electronics, replacing lower bandwidth digital fringe counting electronics. The raw outputs of the high bandwidth electronics, which are proportional to the sine and cosine of the interferometric phase shift, are digitized at up to 10 MHz, which is sufficient for fluctuation analysis. Extraction of the measured phase from the sine and cosine signals is now performed entirely in software, providing the line-integrated electron density at high bandwidth. The interferometer design, calibration, and measurement uncertainty is presented. Measurement uncertainties due to nonlinearities in the analog electronics are found to be comparable to the uncertainties of the previous system.

The interferometer can now resolve line-integrated electron density fluctuations with major-radial wavenumbers below $|k_R| \approx 3.0\ \mathrm{cm}^{-1}$. The new fluctuation measurement capability is used to partially verify the calibration and low-k_R wavenumber response of phase-contrast imaging, to aid in gyrokinetic transport model validation research. Agreement between the two diagnostics is demonstrated for broadband fluctuations and the low-k_R component of the quasi-coherent mode, improving confidence in the calibration of the phase-contrast imaging system. Both diagnostics observe a series of fluctuations during quasi-steady periods of minority heated I-mode plasmas with strong off-axis electron heating. The observed fluctuations are localized to the plasma core using Doppler shift analysis and data from edge fluctuation diagnostics. Transport analysis shows that the fluctuations do not correlate with enhanced thermal transport, and gyrokinetic linear stability analysis shows that the plasma is stable to drift wave turbulence, ruling out the possibility that the observed fluctuations are destabilized drift wave turbulence.

Thesis Supervisor: Anne E. White
Title: Assistant Professor

Acknowledgments

I need to thank my adviser, Prof. Anne White, and reader, Dr. Jim Irby, for their time, effort, and guidance. I am also grateful to Rick Murray, Dan Coronado, Josh Stillerman, Dr. Paul Bonoli, Dr. Nathan Howard, Choongki Sung, Dr. Matt Reinke, and Paul Ennever, each of whom contributed to this research effort. I also thank the entire Alcator C-Mod technical and engineering staff for their operation of the tokamak, and the PSFC and C-Mod administrative staffs, in particular Jessica Coco, for simplifying travel, reimbursements, and funding applications.

The hardware portion of this thesis was supported by the Alcator C-Mod Department of Energy contract (DE-FC02-99ER54512-CMOD). I was personally supported by a Research Assistantship funded partially by Prof. Anne White's Department of Energy Early Career Award (DE-SC0006419), with the remainder coming from the MIT Department of Nuclear Science and Engineering.

Contents

List of Figures

List of Tables

Chapter 1

Introduction

Nuclear fusion holds enormous promise to alleviate the world's ever-expanding need for base-load electrical power. Nuclear fusion reactions were first proposed as a potential peaceful energy source in the 1950s, starting a worldwide research effort to commercialize fusion energy. To do so, a plasma of fusion reactants must be confined and heated to allow the particles time to overcome Coulomb repulsion and fuse, releasing over one million times as much energy as obtainable by chemical processes. Since the late 1960s, the most widely-studied and successful method of confining such a plasma is with a device called a *tokamak*. The word "tokamak" is an English-language transliteration of a Russian acronym meaning "toroidal chamber with axial magnetic field," and that is precisely what it is: a magnetic bottle. A number of technological challenges have slowed the commercialization of tokamak fusion reactors, but improvements in plasma diagnostics and theoretical/computational models continue to push back the boundaries of plasma science, and will hopefully lead to a successful fusion energy reactor.

One of the major challenges associated with tokamak fusion energy research is the problem of fluctuation-driven energy transport out of the plasma. To attempt to understand and mitigate transport, measurements of core fluctuations are needed to compare with theoretical models and codes. Historically, however, diagnostics have had difficulty accessing the core region of high performance fusion plasmas to measure fluctuations. This thesis describes the design and implementation of a new electron

density fluctuation diagnostic based on the existing two-color interferometer (TCI)[1, 2] on the Alcator C-Mod tokamak.[3, 4] The new system provides measurements of line-integrated electron density fluctuations that complement existing fluctuation diagnostics on Alcator C-Mod.

This thesis is presented in the following way. Chapter 1 introduces important background information about transport in tokamaks, the Alcator C-Mod tokamak, and reviews of interferometry-based plasma diagnostics. Chapter 1 also formally introduces the upgraded TCI fluctuation diagnostic and gives background information on mode-conversion/minority-heating (MC/MH) experiments, which are studied later using measurements from the upgraded diagnostic. The physical principles of two-color interferometry are described in Chapter 2. Chapter 3 discusses the implementation of TCI on Alcator C-Mod, including an in-depth description of the upgraded electronics which allow the system to function as a fluctuation diagnostic. The upgraded system is characterized as a fluctuation diagnostic in Chapter 4. The new TCI capabilities are used to partially validate the calibration of another fluctuation diagnostic in Chapter 5. Fluctuation measurements in MC/MH experiments are presented and characterized in Chapter 6. Chapter 7 summarizes the upgrades to the TCI diagnostic and its new operating characteristics, and examines several possible changes which could improve its performance.

1.1 Motivation

A confined plasma will always have gradients in the electron density and temperature profiles, and the presence of gradients leads naturally to diffusive transport out of the confinement region. For the case of an electron temperature gradient (in the absence of any thermal pinch), the temperature will evolve according to the heat diffusion equation,

$$\frac{\partial T_e}{\partial t} = \nabla \cdot (\chi_e \nabla T_e)$$

where χ_e is the electron thermal diffusion coefficient and T_e is the electron temperature. Similar equations can be written for particle and momentum transport; for

particles,

$$\vec{\Gamma} = -D\nabla n + n\vec{v}$$

where $\vec{\Gamma}$ is the particle flux, D is the particle diffusion coefficient, n is the particle number density, and $\vec{v}$ is a convective or pinch velocity. The various diffusion coefficients and pinch velocities can be derived in cylindrical coordinates using classical diffusion theory.

However, a tokamak plasma is not a simple cylinder, and as a result it has much more complicated physics. A tokamak is a cylinder bent so its ends connect into a donut-like shape. The major components of a tokamak are shown in Figure 1-1 and the coordinate system is shown in Figure 1-2. The central transformer coil drives a toroidal electric field which breaks down the gas initially contained in the vacuum vessel (not shown), forming a plasma. The toroidal field coils create a magnetic field which confines the plasma. The electric field drives a toroidal plasma current which creates a small poloidal magnetic field, thus the overall magnetic field topology is helically shaped. Additional coils are used to create a vertical field to stabilize and control the plasma.

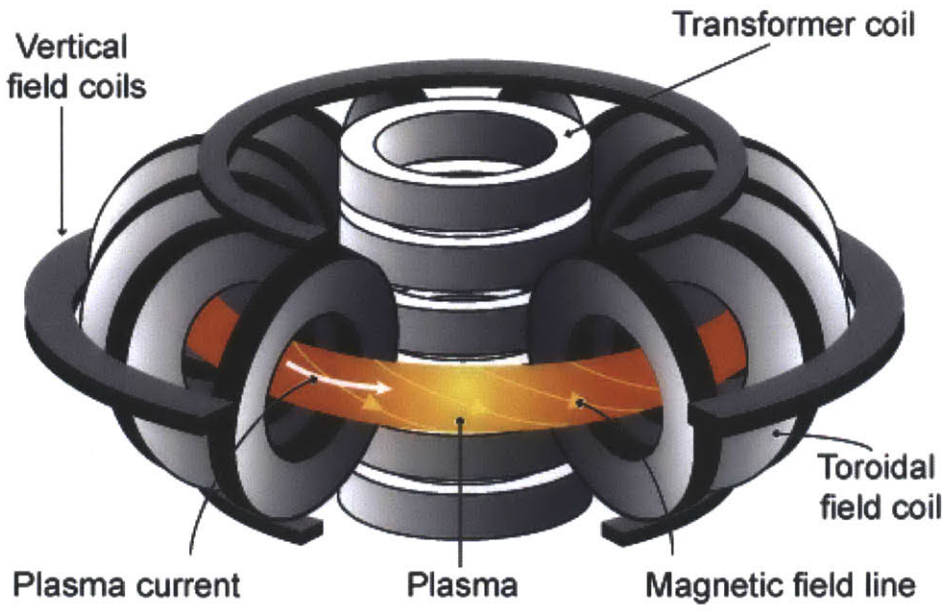

Figure 1-1: Design of a tokamak. Graphic courtesy of General Fusion.[5]

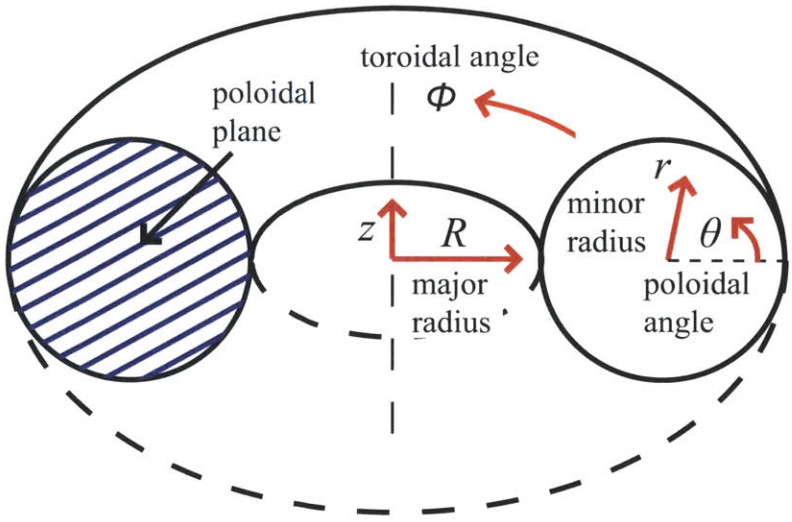

Figure 1-2: Toroidal coordinate system and terminology.

There are critical consequences of the toroidal geometry used to confine a tokamak plasma. The total current density in the toroidal field coils is higher on the inside of the torus than on the outside of the torus, and as a result the toroidal magnetic field has a $1/R$ scaling. The Lorentz force law allows particles to freely stream along magnetic field lines, so an electron driven by the toroidal electric field will sample regions of varying magnetic field strength due to the $1/R$ scaling and helical topology of the field. A fraction of particles with insufficient parallel (to the magnetic field) velocity can become trapped in a magnetic mirror,[6] where a particle is reflected in the high field region, traverses the weak field region, and reflects when it re-encounters the high field region. When these "trapped" particle orbits are projected onto the poloidal plane, they appear banana-shaped, so trapped particle trajectories are called "banana" orbits.

Classical diffusion theory breaks down in the presence of trapped particle banana orbits because they change the perpendicular (to the magnetic field) step-size and timescale of the random-walk diffusion process. Neoclassical theory was developed to account for trapped particle effects,[7] and the result is substantially increased values of the classical diffusion coefficient. Typical orders of magnitude for neoclassical thermal and particle transport coefficients in tokamak plasmas are $\chi_e^{nc}, D_e^{nc} \sim 10^{-3} -$

10^{-2} m^2/s, and typical particle pinch velocities are on the order of $v_e^{nc} \approx 1$ m/s.[8]

Experimental measurements of electron thermal and particle diffusion in tokamak plasmas leads to effective diffusion coefficients on the order of $\chi_e, D_e \approx 1$ m^2/s,[8] which is two to three orders of magnitude higher than neoclassical predictions. Similarly, experimental measurements of particle pinch velocities are an order of magnitude above neoclassical predictions. Plasma confinement is much poorer than neoclassical theory predicts. When plasma confinement properties were first being studied, researchers did not have an adequate hypothesis for the cause of the high levels of transport and simply called it "anomalous." Anomalous transport has since been determined to be mostly fluctuation-driven turbulent transport.[9]

The study of turbulent fluctuations is very important when trying to understand energy transport processes in tokamaks. If plasma turbulence can be understood, then methods of reducing or eliminating deleterious effects can be designed and implemented, increasing the chances of successfully building a fusion energy reactor. Understanding plasma turbulence is a monumental task due to vast differences in the temporal and spatial scales of the fluctuations which drive the turbulent transport.[9] Computationally, it is very difficult to develop codes which can simultaneously predict aspects of turbulence in widely varying spatial and temporal regimes. Experimentally, it can be difficult to access the core region of plasma where many turbulent processes exist, and diagnostics are only sensitive to a small subset of the spatial scales of turbulence present in the plasma. As a result, quantitative interpretation of turbulence measurements, and hence comparisons to theoretical and computational predictions, are very difficult.

Benchmarking theoretical turbulent transport models to experimental turbulence measurements is a major area of fusion energy research, and is the primary goal of the transport model validation community. While theorists and computational physicists improve transport models and simulation capabilities, diagnosticians and experimental physicists continue to develop better turbulence diagnostics. This thesis introduces another diagnostic with several direct and indirect applications to transport model validation research.

Three classes of fluctuation-driven "drift wave" turbulence have been identified as most important in the core of high performance tokamaks. The long wavelength ion temperature gradient (ITG) mode and the intermediate wavelength trapped electron mode (TEM) have each been studied extensively, while the short wavelength electron temperature gradient (ETG) mode is less well understood. The spatial scales of these three modes are presented in Figure 1-3, where k_θ is the poloidal wavenumber of the fluctuation. The linear stability of drift waves such as ITG and TEM in a plasma with interesting electron density fluctuations will be calculated later using gyrokinetic theory[10, 11] as implemented in the GYRO[12] code.

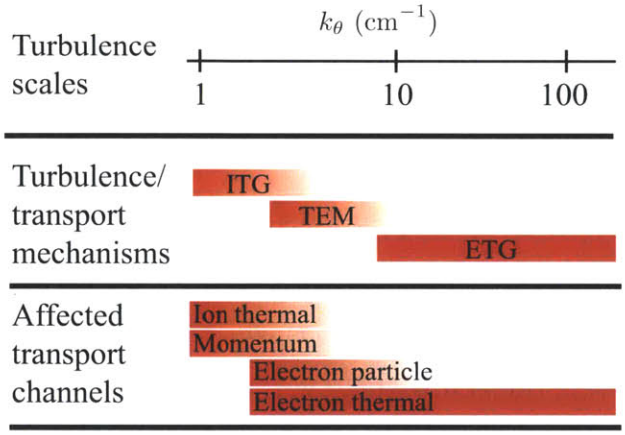

Figure 1-3: Scale-lengths and transport channels for drift wave turbulence: the long-wavelength ion temperature gradient (ITG) mode, the intermediate-wavelength trapped electron mode (TEM), and the short-wavelength electron temperature gradient (ETG) mode. Figure adapted from Fig. 2 in Ref. [9].

1.2 The Alcator C-Mod Tokamak

Alcator C-Mod was built at the Massachusetts Institute of Technology in the late 1980s as an upgrade to the successful Alcator A and C programs.[3, 4] C-Mod is a high-field, diverted tokamak, producing shaped plasmas with significant external radio frequency (RF) heating capability. Primary research themes include plasma transport processes, ion cyclotron radio frequency (ICRF) heating, external current

drive with lower-hybrid waves and ICRF, and plasma-material interactions. The design parameters are summarized in Table 1.1.

Parameter	Typical values
Major radius (R_0)	0.66 m
Minor radius (a)	0.21 m
Elongation (κ)	1.6
Triangularity (δ)	0.4
Toroidal field (B_T)	$\leq$ 8 T
Plasma current (I_p)	$\leq$ 1-2 MA
ICRF heating power	$\leq$ 5 MW
Electron density (n_e)	$\leq 1 \times 10^{21}$ m^{-3}
Electron temperature (T_e)	$\leq$ 10 keV
Ion temperature (T_i)	$T_i \lesssim T_e$ (core)
	$T_i = T_e$ ($r/a \gtrsim 0.8$)
Pulse length	$\leq$ 2 s

Table 1.1: Alcator C-Mod plasma parameters.

In the late 2000s an "improved" confinement (I-mode) regime was accessed on Alcator C-Mod.[13] I-mode exhibits fairly poor particle confinement but very good energy confinement, and both of these characteristics are alluring properties for fusion reactor scenarios. Regimes with good particle confinement characteristics like the "high" confinement mode (H-mode) typically exhibit large instabilities near the plasma edge to regulate impurity accumulation; two examples are edge-localized modes (ELMs)[14] and the quasi-coherent mode (QCM).[15] These instabilities can be detrimental to plasma performance and can increase plasma-material interactions. The I-mode regime has a weakly coherent instability that regulates edge particles, and results in H-mode-like temperature profiles without impurity accumulation.

Alcator C-Mod has a variety of different RF systems to heat the plasma and drive current and rotation. Relevant to this thesis are the ICRF systems which include a field-aligned 4-strap antenna and two conventional antennas which combine to provide up to 5 MW of heating power at frequencies between 50-80 MHz.[16, 17] The ICRF systems are critical for mode-conversion/minority-heating (MC/MH) experiments. With enough power, ICRF waves launched using the 50 MHz antenna can undergo

mode-conversion and heat the plasma, drive flows, or drive current. Additional RF heating power at 80 MHz is needed for the plasma to access I-mode.[13]

C-Mod possesses an impressive suite of plasma diagnostics. Several reflectometry systems operate at different frequencies to measure localized electron density fluctuations.[18] Electron cyclotron emission (ECE) systems measure electron temperature profiles[19] and fluctuations.[20] An x-ray spectroscopy system measures line emission from impurities, providing time-resolved profiles of the ion temperature and plasma rotation.[21, 22] A Thomson scattering diagnostic provides electron density and temperature profiles.[23] Information from reflectometry and x-ray spectroscopy allows partial localization of line-integrated TCI measurements. Profile measurements from the ECE and Thomson scattering systems are also critically important for energy transport calculations and linear stability analysis of turbulence.

1.3 Review of Selected Interferometry Techniques

Apart from plasma current diagnostics and magnetic field pick-up coils, interferometers are some of the most simple and reliable plasma diagnostics. A number of different varieties of interferometers have been used as electron density diagnostics, including various forms of two-color interferometry (TCI) and an internal reference technique known as phase-contrast imaging (PCI). TCI is commonly used for active density feedback control, and PCI is used to measure line-integrated electron density fluctuations and RF physics.

The literature contains descriptions of many different TCI implementations on a plethora of plasma physics experiments, as described below. However, there are very few descriptions of standard external reference interferometers such as TCI being used as fluctuation diagnostics for fusion-grade plasma experiments. When interferometers have been used to measure fluctuations, they have been implemented as interferometric imaging systems.[24] These systems use a different operating principle than the multi-chord interferometer used on Alcator C-Mod, and the difference makes imaging systems much more complicated than multi-chord interferometry.

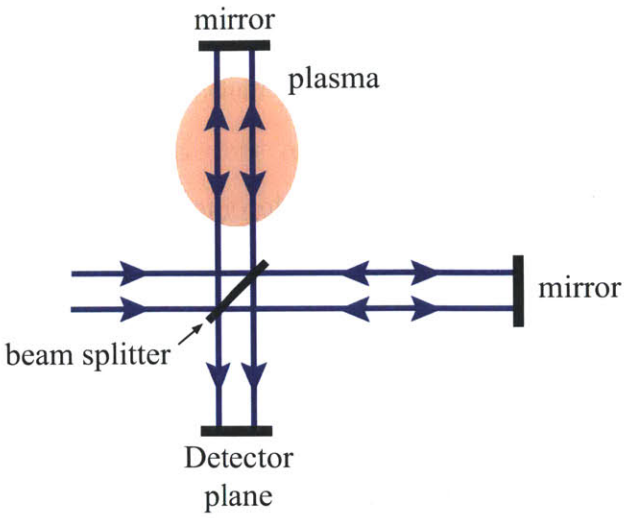

Figure 1-4: Michelson interferometer configuration.

1.3.1 Two-Color Interferometry

Two-color interferometry is the primary density feedback diagnostic used in large tokamak experiments around the world, including Alcator C-Mod. Co-axial radiation at two different wavelengths is sent through the plasma and then detected using a Michelson configuration, as shown in Figure 1-4. The primary wavelength obtains a phase shift from the plasma electron density, but also contains phase shifts due to vibration of optical components. The second wavelength is used to characterize the amount of optical vibration along the beam path, with small contributions from the plasma electron density. Both wavelengths are used together to remove the effects of vibration, leaving only the plasma-induced phase shift which is proportional to the line-integrated electron density. The relevant theory will be described in Chapter 2.

The first TCI implementation on a tokamak was in the late 1970s when a CO_2 and HeNe laser TCI system was designed for the Doublet III tokamak at General Atomics.[25, 26] Since then, similar CO_2-based interferometers have been employed on many tokamaks including DIII-D,[27] Alcator C-Mod,[1] JT60-U,[28] and FTU.[29] CO_2-based interferometers have also been installed on other types of plasma experiments, including the C-2 field-reversed configuration experiment,[30] the TJ-II[31] and LHD[32] stellarators, and the RFX[33] and MST[34] reversed-field pinches. A

two-color dispersion interferometer using a CO_2 laser is currently being designed for the W7-X stellarator.[35] In addition to CO_2-based systems, two-color far-infrared (FIR) interferometers have been employed on the LHD stellarator[36] and the JET tokamak.[37] Millimeter-wave two-color interferometers have been used in the divertor regions of JET[38] and JT60-U.[39] Two-color CO_2-based interferometers are considered to be the most reliable systems today because the CO_2 wavelength has substantially more plasma-induced signal than shorter wavelength lasers, but is not as susceptible to the detrimental effects of beam refraction as longer wavelength systems.

An external reference CO_2 interferometer was used to measure density fluctuations on the LT-4 tokamak in the late 1980s.[24] This was an interferometric imaging system (as opposed to a multi-chord interferometer) employing the Mach-Zender technique. The primary difference between the imaging system and the multi-chord system employed on Alcator C-Mod is the sensitivity to the background (non-fluctuating) density. The interferometer on LT-4 employed a feedback system to remove the background density and maximize the sensitivity of the system to plasma-induced density fluctuations. The TCI system on Alcator C-Mod is a multi-chord Michelson interferometer, not an imaging system, and is sensitive to the background density. As a result, the methods described in Ref. [24] are not applicable to the TCI system on Alcator C-Mod. (The differences are explained in detail in Section 2.5.)

There are many possible choices for secondary lasers in CO_2-based TCI systems. In present-day experiments, the most common choice is a visible HeNe laser ($\lambda = 633$ nm, red). The advantage of HeNe lasers is that the short wavelength is extremely sensitive to vibrational effects but nearly impervious to plasma effects. HeNe lasers are also advantageous simply because they are visible to the human eye, making alignment of the interferometer much simpler. Other wavelengths are equally valid and have advantages in certain situations. For example, next-generation experiments may have darkened windows in diagnostic ports. Obviously, transmission of visible light is reduced through these windows, so alternative wavelengths such as an infrared (IR) HeNe laser ($\lambda = 3.39$ μm) are beneficial.[40] Larger experiments like the proposed Compact Ignition Tokamak and ITER will have substantially larger vibrations than

current experiments, corresponding to a larger phase-shift measured by the secondary laser.[41] In these large devices an interferometer using a short wavelength HeNe laser would have difficulty following all the vibration-induced fringes,[42] but an IR-HeNe laser will perform better due to its longer wavelength.

The literature contains much information on TCI systems with a variety of secondary laser wavelengths. However, regardless of the choice of secondary wavelength, fluctuation measurements at timescales significantly faster than the vibration timescale should always be possible using only the primary laser, with the slowly varying component eliminated using Fourier analysis. The secondary laser is only needed for background line-integrated density measurements and is critical for active density feedback systems, but is not crucial for fluctuation measurements.

1.3.2 Phase-Contrast Imaging

Phase-contrast imaging (PCI)[43, 44] is another interferometry-based electron density diagnostic with several important distinctions from TCI. PCI is an internal reference interferometer that is only sensitive to density fluctuations, whereas TCI uses an external reference and is therefore sensitive to both fluctuations and the background density.

PCI operates in the following way. A laser beam is sent through plasma and a portion of the beam is scattered by density fluctuations. The scattered and unscattered components are focused onto a phase plate which consists of a horizontal groove with a depth equal to one eighth of the probing beam wavelength. The phase plate is shown in Figure 1-5. The unscattered portion of the beam is focused into the groove and the scattered components are focused onto the non-grooved portion of the phase plate. The result is that the unscattered beam travels a path length $\lambda/4$ longer than the scattered beam components. The path length difference is the same as applying a $\pi/2$ phase shift to the unscattered beam relative to the scattered beam. The scattered and unscattered beams are focused together at the detector plane. The interference of the beams results in intensity variations, from which the phase shift due to density fluctuations is derived using a heterodyne technique.[44]

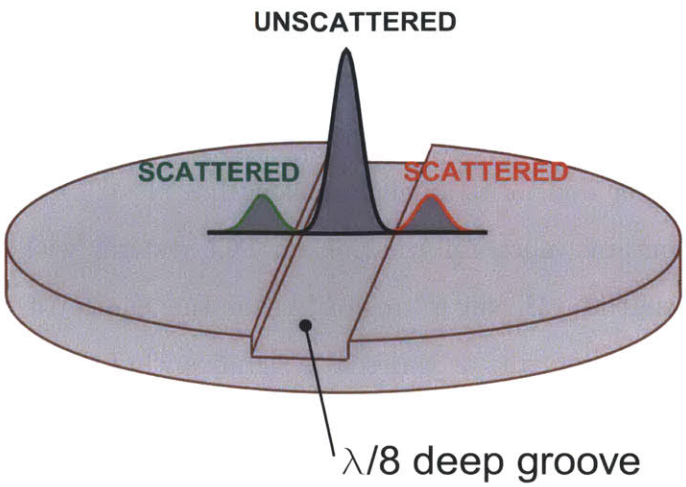

Figure 1-5: Phase-contrast imaging phase plate. Figure is adapted from Fig. 2-9 in Ref. [44].

The presence of the phase plate, while critical for the operation of the diagnostic, also presents a significant limitation. Long wavelength (low wavenumber) electron density fluctuations do not cause substantial beam scattering, so these portions of the scattered beam will still fall within the finite width of the groove in the phase plate. When the scattered components are interfered with the unscattered beam, there will be no beat signals from the long wavelength fluctuations because they also obtained a $\pi/2$ phase shift. As a result, PCI has a low wavenumber cutoff in the measured density fluctuation spectrum.

The details of the PCI wavenumber response vary depending on how the system is configured. In this thesis, quantitative fluctuation data from PCI is only required for comparisons to TCI, in an effort to verify the PCI calibration. When the quantitative data was collected, PCI was optimized to detect electron density fluctuations and the calibrated wavenumber response is shown in Figure 1-6. The major-radial wavenumber (k_R) cutoff extends from zero to $|k_R| \approx 1.5$ cm^{-1}. The diagnostic response peaks at $k_R = \pm 2$ cm^{-1} and drops off to zero at $|k_R| > 15$ cm^{-1}. The response function is symmetric about $k_R = 0$.

The purpose of the PCI implementation on Alcator C-Mod[44] was initially to measure RF wave physics and coherent modes.[45, 46, 47, 48] The RF measurement

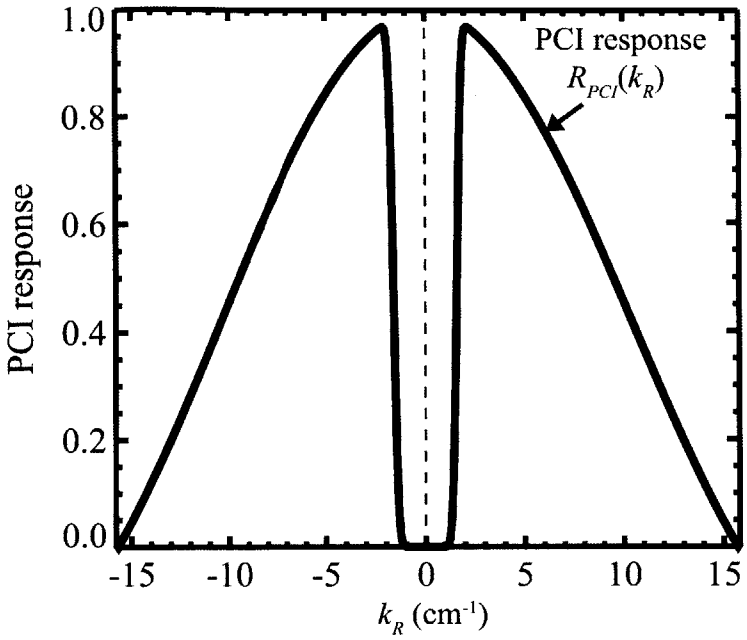

Figure 1-6: PCI wavenumber transfer function as configured for quantitative comparisons to TCI.

capabilities of PCI make the system the primary diagnostic used to measure wave physics in mode-conversion/minority-heating (MC/MH) experiments.[49, 50, 51] The system was upgraded to measure line-integrated electron density fluctuations and quickly became a workhorse fluctuation diagnostic on C-Mod.[52, 53, 54, 55] PCI has a considerably different fluctuation wavenumber sensitivity than the present implementation of TCI, but the two diagnostics are similar enough that they can be quantitatively compared for the purpose of validating the PCI calibration and wavenumber response. This is done in Chapter 5.

1.3.3 TCI as a Fluctuation Diagnostic

It was previously mentioned that PCI is the workhorse fluctuation diagnostic on Alcator C-Mod. Why, then, is a similar line-integrated density fluctuation diagnostic such as TCI even needed when PCI has been proven to be a mature and reliable system? First, PCI must be configured differently depending on whether it is measuring RF physics or electron density fluctuations, and thus it may not provide optimized den-

sity fluctuation measurements when they are desired. The TCI fluctuation diagnostic, once it is further upgraded to match the fluctuation measurement capabilities of PCI, could provide high-quality line-integrated electron density fluctuation measurements in all types of plasmas when PCI may not be available.

Even in plasmas where PCI is optimized as a fluctuation diagnostic, TCI provides additional capabilities. First, the PCI low-k_R cutoff precludes measurement of some low-frequency, low-k_R turbulence and coherent modes which can be detected by TCI. Additionally, TCI provides a second measurement of the same quantity as PCI but at a different toroidal location. If the two diagnostics share a digitizer, they could be used together for correlation analysis to resolve toroidal mode-numbers. Perhaps most importantly, TCI has a very straightforward calibration whereas the PCI calibration procedure is more difficult to implement. Broadband and coherent fluctuations measured by TCI can be used to quantitatively verify the PCI calibration, improving the confidence in transport model validation efforts which compare PCI data to simulations.

Upgrading the TCI diagnostic to measure fluctuations is relatively simple and inexpensive, and can be implemented on other tokamaks which use laser interferometry to measure the line-integrated electron density. The additional hardware which permits TCI to be operated as a fluctuation diagnostic consists solely of new electronics and digitizers.[2] Low bandwidth fringe counting electronics[1] are replaced with high bandwidth analog in-phase/quadrature phase demodulators. The demodulators have two outputs that are proportional to the sine and cosine of the measured phase shift, and are directly digitized at up to 10 MHz with new digitizers. The phase shift is digitally reconstructed in software from the raw sine and cosine signals. This thesis will describe in detail the new electronics and new phase-reconstruction software, and will present the first fluctuation measurements made with the upgraded diagnostic.

1.4 Mode-Conversion/Minority-Heating

One of the most successful methods to reduce turbulent transport in tokamaks is to introduce a plasma flow shear.[56] Flow shear breaks up turbulent eddies and thus decreases the turbulent transport of energy out of the plasma. The ability to control the radial profile of plasma flow is a very important aspect of future fusion energy reactors. Many present-day devices use neutral beam injection to drive plasma rotation, but the efficiency of flow drive scales unfavorably to reactor-relevant regimes.[57, 58] Therefore, alternative methods of driving plasma rotation are currently being studied, including RF techniques.

One popular RF technique is to launch waves with frequencies in the ion cyclotron radio frequency (ICRF) range. The waves propagate into the plasma and then convert into other waves having more efficient energy deposition properties.[59, 60, 61] The presence of minority species, such as hydrogen or helium-3 in the case of a deuterium-majority plasma, is important for efficient transfer of the energy of the waves to the plasma. While some energy is transferred directly to electrons (and majority ions), the waves damp efficiently on the minorities and accelerate them to very high energies. The fast minority population then damps on electrons and ions, transferring the energy to the bulk plasma. In Alcator C-Mod, mode-conversion experiments rely on a helium-3 minority, so the term "minority-heating" also applies to mode-conversion experiments.

The mode-conversion/minority-heating (MC/MH) technique can be used not only to heat the plasma, but also to drive plasma flow[58] and plasma current.[62] Since the location within the plasma where the incoming wave is mode-converted depends on the density and magnetic field of the plasma,[63] there is some amount of external control of where the energy is deposited. Off-axis heating can drive plasma current at a particular radial location, allowing a certain degree of current profile control.[61, 64]

Experiments at Alcator C-Mod have successfully demonstrated the viability of toroidal and poloidal plasma flow drive using mode-converted ICRF waves.[49, 57, 58] Fast magnetosonic waves are launched into the plasma by an ICRF antenna at 50

MHz and are mode-converted into the ion cyclotron wave and the ion Bernstein wave, and these waves damp on minorities and drive plasma flows.[45, 65] Recent I-mode experiments on Alcator C-Mod with ICRF MC/MH flow drive have exhibited very good confinement properties as a result of these flows.[66]

More recently, additional high-performance I-mode experiments were conducted to try and further characterize MC/MH plasmas by searching for neoclassical tearing modes (NTMs), which are suspected to limit plasma rotation.[67] Unfortunately, the available ICRF power at 50 MHz was insufficient to drive any significant mode-conversion plasma flows. Off-axis minority-heating was still strong enough to drive large sawtooth events, which greatly alter the core electron temperature profile on a $20 - 30$ ms timescale. TCI and PCI both detected a series of fluctuations in these discharges which do not have the expected behavior of an NTM. The fluctuations will be described and analyzed in detail in Chapter 6.

Chapter 2

Two-Color Interferometry

The following chapter introduces the theory of two-color interferometry (TCI) and various engineering constraints that are considered when designing a TCI system to measure plasma electron density and fluctuations. TCI takes advantage of the fact that the speed of light varies in media with varying indices of refraction. The difference in speed can be detected by measuring the relative phase shift between light waves traveling through a medium and light traveling through air. When the medium is a plasma, a simple model can be used to relate the relative phase difference between light traveling through the air and through the plasma to the line-integrated plasma electron density. The model is used to inform interferometer design decisions by considering signal levels compared to vibration and refractory effects. A useful reference for more information about interferometer systems is Ref. [68].

2.1 Plasma Model

The goal of this section is to derive an equation relating the observable phase shift of a probe beam to the plasma electron density. To begin, consider the definition of the wavenumber,

$$k = \frac{2\pi}{\lambda} \tag{2.1}$$

where λ is the wavelength of the probe beam. From this expression, it follows that the total phase accrued by a propagating beam, ϕ, at any position x along the direction of propagation is equal to the wavenumber integrated over the total path length traveled by the beam,

$$\phi = \int k(x)dx. \tag{2.2}$$

Interferometry systems have a probing beam traveling through a medium and a reference beam which travels an equivalent path length through air. The detected phase shift is thus the difference between the acquired phase of the reference beam and the acquired phase of the probe beam,

$$\Delta\phi_{meas} = \int \left(k_{probe}(x) - k_{ref}(x)\right) dx. \tag{2.3}$$

This integral is identically zero everywhere along x except where the probe beam travels through plasma. The wavenumber of the reference beam can be found from the dispersion relation of light through air,

$$\frac{\omega}{k_{ref}} = c \tag{2.4}$$

where ω is the angular frequency and c is the speed of light. The wavenumber of the probe beam, k_{probe}, is calculated from the dispersion relation in plasma, which must now be derived. The following derivation is taken loosely from Ref. [69].

The governing equations for electromagnetic waves in any medium are Maxwell's equations,

$$\nabla \times \vec{B} = \mu_0 \vec{j} + \epsilon_0 \mu_0 \frac{\partial \vec{E}}{\partial t} \tag{2.5}$$

$$\nabla \times \vec{E} = -\frac{\partial \vec{B}}{\partial t} \tag{2.6}$$

$$\nabla \cdot \vec{B} = 0 \tag{2.7}$$

$$\nabla \cdot \vec{E} = \rho/\epsilon_0. \tag{2.8}$$

In these equations, $\vec{B}$ is the magnetic field, $\vec{j}$ is the current density, $\vec{E}$ is the electric

field, ρ is the charge density, ϵ_0 is the permittivity of free space, and μ_0 is the vacuum permeability.

To derive the plasma dispersion relation, first take the time derivative of Ampere's Law (Equation 2.5) and the curl of Faraday's Law (Equation 2.6),

$$\nabla \times \dot{\vec{B}} = \mu_0 \dot{\vec{j}} + \epsilon_0 \mu_0 \ddot{\vec{E}} \tag{2.9}$$

$$\nabla \times (\nabla \times \vec{E}) = -\nabla \times \dot{\vec{B}} \tag{2.10}$$

where the time derivatives have now been expressed with dot notation. Combining Equations 2.9 and 2.10 eliminates the magnetic field and gives an expression in terms of only the electric field and the current density,

$$\nabla \times (\nabla \times \vec{E}) = -\mu_0 \dot{\vec{j}} - \epsilon_0 \mu_0 \ddot{\vec{E}}. \tag{2.11}$$

The next step is to eliminate $\vec{j}$ using the definition of current density,

$$\vec{j} = -e n_e \vec{v}_e \tag{2.12}$$

where e is the fundamental charge, n_e is the electron density, and $\vec{v}_e$ is the electron velocity. Ion motion has been neglected due to its significantly higher inertia compared to electrons. Taking the time derivative of the current density (Equation 2.12) and substituting into Equation 2.11 yields,

$$\nabla \times (\nabla \times \vec{E}) = \mu_0 n_e e \dot{\vec{v}}_e - \epsilon_0 \mu_0 \ddot{\vec{E}}. \tag{2.13}$$

The time derivative of the electron velocity can be eliminated using the momentum balance equation,

$$n_e m_e \dot{\vec{v}}_e = -n_e e(\vec{E} + \vec{v}_e \times \vec{B}) \tag{2.14}$$

where m_e is the electron mass. Applying a vector calculus identity and substituting

Equation 2.14 into Equation 2.13 gives,

$$\nabla(\nabla \cdot \vec{E}) - \nabla^2 \vec{E} = -\frac{\mu_0 n_e e^2}{m_e}(\vec{E} + \vec{v}_e \times \vec{B}) - \epsilon_0 \mu_0 \ddot{\vec{E}}. \tag{2.15}$$

Equation 2.15 is linearized assuming that there are no mean flows ($\vec{v}_{e,0} = 0$). The first-order equation is

$$\nabla(\nabla \cdot \vec{E}_1) - \nabla^2 \vec{E}_1 = -\frac{\mu_0 n_e e^2}{m_e}(\vec{E}_1 + \vec{v}_{e,1} \times \vec{B}_0) - \epsilon_0 \mu_0 \ddot{\vec{E}}_1 \tag{2.16}$$

where $\vec{E}_1$ is the electric field induced by the probe beam and $\vec{v}_{e,1}$ is the response of the electrons to the probe beam. Now the plane-wave approximation is applied which assumes small amplitude sinusoidal oscillations in all the perturbed quantities,

$$\vec{E}_1, \vec{v}_{e,1} \sim e^{i(\vec{k}\cdot\vec{r} - \omega t)}.$$

The plane-wave approximation allows the following substitutions for operators acting on an arbitrary function f,

$$\begin{aligned} \nabla f &\rightarrow i\vec{k} f \\ \nabla \cdot \vec{f} &\rightarrow i\vec{k} \cdot \vec{f} \\ \nabla^2 f &\rightarrow -k^2 f \\ \frac{\partial}{\partial t} f &\rightarrow -i\omega f. \end{aligned}$$

With these substitutions, Equation 2.16 becomes

$$-\vec{k}(\vec{k} \cdot \vec{E}_1) + k^2 \vec{E}_1 = -\frac{\mu_0 n_e e^2}{m_e}(\vec{E}_1 + \vec{v}_{e,1} \times \vec{B}_0) + \epsilon_0 \mu_0 \omega^2 \vec{E}_1. \tag{2.17}$$

Now several assumptions are made concerning the orientation of $\vec{E}$, $\vec{k}$, and $\vec{B}$. First, the wave vector and the background magnetic field are assumed to be perpendicular. This is a justifiable assumption for this thesis because in the interferometer implementation on Alcator C-Mod, the probe beam is passed vertically through the

plasma. The direction of propagation is thus perpendicular to the toroidal magnetic field, and since the toroidal field dominates the direction of the total magnetic field, the assumption that $\vec{k} \perp \vec{B}_0$ is justified.

Next, it is assumed that the probe beam consists of transverse waves, which means that the wave vector is perpendicular to the oscillating electric field. On Alcator C-Mod, the probe beam consists of electromagnetic waves from a laser, and since all electromagnetic waves are transverse waves, the assumption that $\vec{k} \perp \vec{E}_1$ is justified.

Finally, it is assumed that the oscillating electric field is parallel to the background magnetic field, $\vec{E}_1 \parallel \vec{B}_0$. This assumption is not immediately justifiable, but will be revisited later.

Applying these assumptions to Equation 2.17 greatly simplifies the expression once a coordinate system is specified. The background magnetic field is chosen to be in the z-direction, $\vec{B}_0 = B_z\hat{z}$. This choice of axes forces the wave field to be in the z-direction as well, $\vec{E}_1 = E_1\hat{z}$. The wave vector $\vec{k}$ is always perpendicular to $\vec{E}_1$, so $\vec{k} \cdot \vec{E}_1 = 0$. Since there is only a z-component of the background magnetic field, there will be no z-component of the cross product between the field and $\vec{v}_{e,1}$. The result is that the z-component of Equation 2.17 becomes,

$$k^2 E_1 = -\frac{\mu_0 n_e e^2}{m_e} E_1 + \epsilon_0 \mu_0 \omega^2 E_1. \tag{2.18}$$

This equation is typically written in a clearer way using expressions for the speed of light, c, and the electron plasma frequency, ω_{pe},

$$\begin{aligned} c^2 &= 1/\epsilon_0 \mu_0 \\ \omega_{pe}^2 &= \frac{n_e e^2}{\epsilon_0 m_e}. \end{aligned} \tag{2.19}$$

With these expressions Equation 2.18 can be rewritten as

$$(c^2 k^2 + \omega_{pe}^2 - \omega^2) E_1 = 0. \tag{2.20}$$

For a nontrivial wave field E_1, the term in parenthesis must be zero, giving the plasma

dispersion relation,

$$\omega^2 = \omega_{pe}^2 + c^2 k^2. \tag{2.21}$$

The wave described by the dispersion relation in Equation 2.21 is known as the *ordinary* mode or O-mode wave.

Relaxing the requirement that $\vec{E}_1 \parallel \vec{B}_0$ would allow the oscillating electric field to have components in both the x- and y-directions (elliptical polarization). A thorough treatment of this case is given in Ref. [69], and the dispersion relation for such a wave is found to be,

$$\frac{c^2 k^2}{\omega^2} = 1 - \frac{\omega_{pe}^2}{\omega^2} \frac{\omega^2 - \omega_{pe}^2}{\omega^2 - \omega_h^2} \tag{2.22}$$

where $\omega_h^2 = \omega_{pe}^2 + \omega_{ce}^2$ is the upper hybrid frequency and $\omega_{ce} = eB/m_e$ is the electron cyclotron frequency. Waves satisfying the dispersion relation given by Equation 2.22 are called *extraordinary* modes or X-modes. To determine the validity of the assumption made in the derivation of the O-mode dispersion relation (that $\vec{E}_1 \parallel \vec{B}_0$), the relative magnitudes of the various frequencies can be analyzed. First, rewrite Equation 2.22 as,

$$\begin{aligned} c^2 k^2 &= \omega^2 - \omega_{pe}^2 \frac{\omega^2 - \omega_{pe}^2}{\omega^2 - \omega_h^2} \\ c^2 k^2 &= \omega^2 - \omega_{pe}^2 \frac{1 - \omega_{pe}^2/\omega^2}{1 - \omega_h^2/\omega^2}. \end{aligned} \tag{2.23}$$

Typical C-Mod plasmas have a magnetic field below $B_0 \sim 8$ T and an electron density below $n_e \sim 10^{21}$ m^{-3}. These parameters give the following order of magnitude values for the frequencies appearing in Equations 2.21 and 2.22:

$$\omega_{ce}^2 = \left(\frac{eB}{m_e}\right)^2 = \left(\frac{(1.6 \times 10^{-19})(8)}{9.1 \times 10^{-31}}\right)^2 \sim 2 \times 10^{24} \text{ (rad/s)}^2 \tag{2.24}$$

$$\omega_{pe}^2 = \frac{n_e e^2}{\epsilon_0 m_e} = \frac{(10^{21})(1.6 \times 10^{-19})^2}{(8.85 \times 10^{-12})(9.1 \times 10^{-31})} \sim 3 \times 10^{24} \text{ (rad/s)}^2 \tag{2.25}$$

$$\omega_h^2 = \omega_{pe}^2 + \omega_{ce}^2 \sim 5 \times 10^{24} \text{ (rad/s)}^2 \tag{2.26}$$

The squared frequency of a CO_2 probe beam is,

$$\omega^2 = (2\pi f)^2 = (2\pi c/\lambda)^2 \sim 3 \times 10^{28} \text{ (rad/s)}^2. \tag{2.27}$$

The ratios of ω_{pe}^2/ω^2 and ω_h^2/ω^2 that appear in Equation 2.23 will be on the order of $10^{-3} - 10^{-4}$, which is much less than one. Thus Equation 2.23 is approximately given by,

$$c^2k^2 \approx \omega^2 - \omega_{pe}^2 \tag{2.28}$$

which is just the simple O-mode dispersion relation of Equation 2.21. Thus, the assumption that $\vec{E}_1 \parallel \vec{B}_0$ was justified because the contribution from other polarizations results in an equivalent dispersion relation when applied to Alcator C-Mod plasmas.

With the O-mode dispersion relation derived and the assumptions behind it justified, the phase shift due to the probe beam propagating through the plasma can finally be calculated from Equation 2.3. The wave number of the probe beam is calculated from the O-mode dispersion relation (Equation 2.21),

$$k_{probe} = \frac{1}{c}\sqrt{\omega^2 - \omega_{pe}^2}.$$

It was previously shown that $\omega^2 >> \omega_{pe}^2$ (Equations 2.26 and 2.27), allowing a simple approximation for the wave number in the plasma,

$$\begin{aligned} k_{probe} &= \frac{\omega}{c}\sqrt{1 - \frac{\omega_{pe}^2}{\omega^2}} \\ k_{probe} &\approx \frac{\omega}{c}\left(1 - \frac{1}{2}\frac{\omega_{pe}^2}{\omega^2}\right). \end{aligned} \tag{2.29}$$

The wavenumber of the reference arm outside the plasma is calculated from the dispersion relation of electromagnetic radiation in air (Equation 2.4),

$$k_{ref} = \omega/c. \tag{2.30}$$

The integrand of Equation 2.3 can now be computed using Equations 2.29 and 2.30,

$$\begin{aligned}
\Delta\phi_{meas} &= \int (k_{probe} - k_{ref})\, dx \\
\Delta\phi_{meas} &= \frac{\omega}{c}\int \left(1 - \frac{1}{2}\frac{\omega_{pe}^2}{\omega^2} - 1\right) dx \\
\Delta\phi_{meas} &= -\frac{e^2}{2\epsilon_0 m_e \omega c}\int n_e(x) dx. \qquad (2.31)
\end{aligned}$$

In the last step, the expression for the electron plasma frequency (Equation 2.19) was substituted. The electron density, n_e, will vary along the path length of the probe beam through the plasma and must remain inside the integral.

Many interferometer systems for high-performance fusion plasmas use lasers as the radiation source for the probing beam. Lasers are typically specified by their wavelength, not their frequency, so the final form of the phase shift (Equation 2.31) is rewritten using the relation between frequency and wavelength, $\omega = 2\pi f = 2\pi c/\lambda$,

$$\Delta\phi = -\frac{\lambda_{probe} e^2}{4\pi\epsilon_0 m_e c^2}\int n_e(x) dx. \qquad (2.32)$$

The combination of constants in Equation 2.32, $e^2/4\pi\epsilon_0 m_e c^2$, is known as the classical electron radius and has a value of $r_e = 2.82 \times 10^{-15}$ m. The integral expression is the plasma electron density integrated along the path traveled by the probing wave, thus interferometers are known as "line-integrated" density diagnostics. On Alcator C-Mod the probe beam is passed vertically through the plasma twice, so the final expression for the phase shift is,

$$\Delta\phi = -2 r_e \lambda_{CO_2}\int n_e dz \qquad (2.33)$$

where the generic coordinate x has been replaced with the vertical coordinate z and the probe beam wavelength has been specified as the CO_2 laser wavelength equal to 10.6 μm.

2.2 TCI Design Considerations

In Section 2.1 it was shown that a probing wave traveling through plasma will acquire a phase shift, relative to a reference beam traveling through air, that is proportional to the line-integrated electron density of the plasma. Measurements of line-integrated densities are very useful for plasma control and feedback, studies of magnetohydrodynamics and confinement properties, and studies of small fluctuations relevant to turbulent transport. It is therefore important to determine the plasma-induced phase shift very precisely.

In practice, several difficulties arise when designing and implementing an interferometry system for line-integrated density measurements. Optical elements used to direct the probing beam through the plasma can vibrate, introducing significant phase shifts due to path length changes. Probing radiation can refract when it encounters a spatially varying refractive index in the direction perpendicular to its direction of propagation. Significant refraction can cause a beam to lose its coherence, distorting the detected signal. In severe cases refraction can cause the beam to deflect off of the detector plane entirely, resulting in a complete loss of signal.

Three important and competing factors must be considered when designing an interferometer system. There must be sufficient plasma-induced signal to exceed the noise floor of detection electronics, the effects of vibration must be mitigated, and refraction must be reduced to acceptable levels. The requirements that these three factors place on the design of an interferometer system are now examined.

2.2.1 Signal

As derived in Section 2.1, the plasma-induced phase shift is proportional to the wavelength of the probe beam and the line-integrated plasma electron density. A typical line-integrated electron density in Alcator C-Mod is 1×10^{20} m^{-2}, and the detector and electronics noise has been measured to be about 5° (87 mrad). With this information, a constraint on the probe beam wavelength can be determined from Equation

2.33,

$$\begin{aligned} 0.087 \text{ rad} &<< |\Delta\phi| = 2r_e\lambda_{CO_2}(1 \times 10^{20} \text{ m}^{-2}) \\ \Rightarrow \lambda_{probe} &>> 0.15 \ \mu\text{m}. \end{aligned} \tag{2.34}$$

The wavelength of the probe beam must be significantly larger than 150 nm, due to noise introduced by the TCI detectors and electronics and the plasma properties of Alcator C-Mod.

2.2.2 Vibration

The effect of vibrating optical components is best explained with a diagram. Figure 2-1 shows two different optical paths, one with a mirror that is not vibrating (top) and the other with a mirror that vibrates a total distance l (bottom). The radiation reflecting off of the vibrating mirror will travel a different distance than the radiation reflecting off of the non-vibrating mirror. For example, when the vibrating mirror is in the position $l/2$, as shown in Figure 2-1, the radiation reflecting off of the vibrating mirror will travel a distance l *less* than the radiation reflecting off the non-vibrating mirror. If $l = \lambda$, the beam reflecting off the non-vibrating mirror will accrue an additional 2π phase shift compared to the radiation reflecting off the non-vibrating mirror. A simple expression relates the length-scale of the vibration, l, and the wavelength, λ, to the vibration-induced phase shift, ϕ_v,

$$\phi_v = \frac{2\pi l}{\lambda}. \tag{2.35}$$

The effect of a vibrating mirror on the phase shift of the probing wave scales as the inverse of the wavelength of the probing wave.

2.2.3 Refraction

A probing beam can be refracted when it encounters a spatially-varying index of refraction in the direction perpendicular to its direction of propagation. Refraction

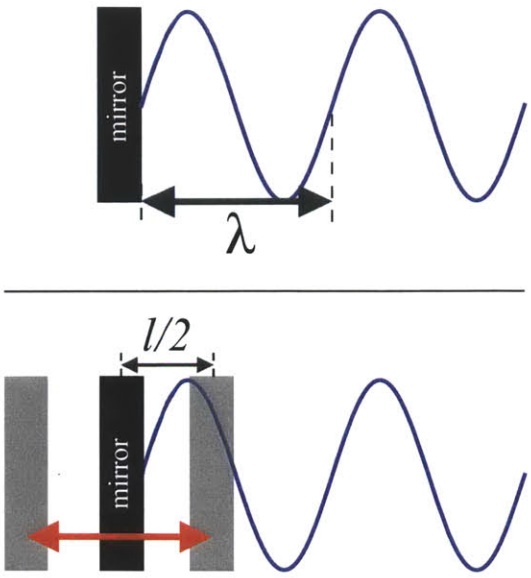

Figure 2-1: Diagram showing how a vibrating optical element (bottom) affects the phase shift of a reflected wave. The bottom mirror vibrates about its center point with length $l/2$. When the vibrating mirror is at the position $l/2$, as shown, the radiation reflecting off the vibrating mirror will travel a total path length l less than the radiation reflecting off the non-vibrating mirror (top). As a result, the radiation from the non-vibrating mirror accrues an additional 2π phase shift compared to the radiation reflecting off the vibrating mirror.

in a simple slab geometry is shown in Figure 2-2. The angle of refraction can be calculated from the definitions made in the slab geometry of Figure 2-2,

$$\sin\theta = \frac{dx}{dy}. \tag{2.36}$$

The length dx is just the length along the direction of propagation of the wave. This length is related to the accrued phase of the wave, $d\phi$,

$$dx = d\phi\frac{\lambda}{2\pi}. \tag{2.37}$$

The expression for the angle of deflection can be written in terms of the derivative of the phase shift in the direction perpendicular to the wave propagation by combining

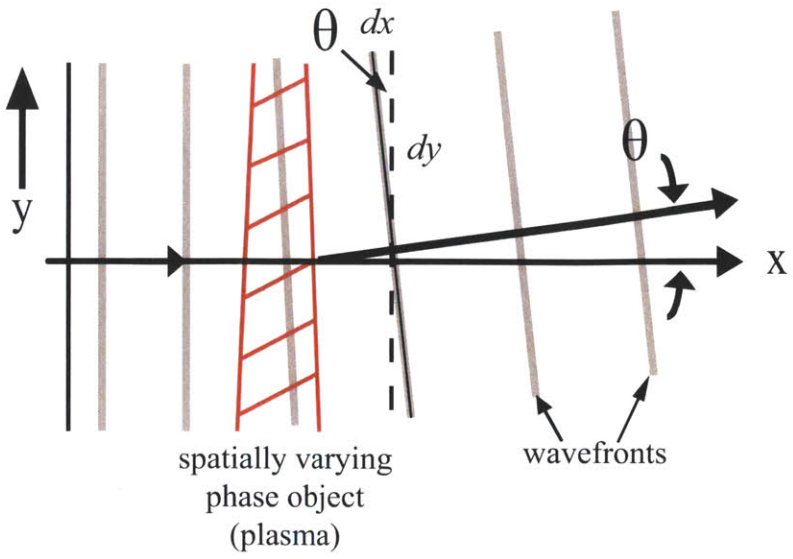

Figure 2-2: Diagram showing how a wave refracts when it encounters a phase object that varies spatially in the direction perpendicular to the wave propagation direction. The angle, θ, through which the wave refracts depends on the strength of the spatial variation of the phase object.

Equations 2.36 and 2.37. Using the small-angle approximation,

$$\sin\theta \approx \theta = \frac{dx}{dy} = \frac{\lambda}{2\pi}\frac{d\phi}{dy}. \tag{2.38}$$

The expression for the phase shift through the plasma, $d\phi$, is known from Equation 2.33. The refracted angle is thus related to the line-integrated electron density derivative in the direction perpendicular to the beam propagation direction,

$$\theta = -2r_e\frac{\lambda_{CO_2}^2}{2\pi}\int\frac{dn_e}{dy}dx. \tag{2.39}$$

The angle of refraction of a probe beam encountering a density gradient is proportional to the square of the wavelength of the probe beam and the line-integral of the density gradient in the direction perpendicular to the direction of beam propagation. (A more robust calculation in a realistic geometry can be found in Ref. [70], but the calculation in slab geometry is sufficient for the purposes of this thesis.)

Refraction is responsible for two detrimental effects: loss of beam coherence at

the detector face and outright loss of signal. Loss of beam coherence is shown in Figure 2-3. To remain coherent, the phase shift across the transverse direction of the wave must not exceed a critical value, usually π.[68] The phase shift across the wavefront is the derivative of the phase shift in the transverse direction multiplied by the transverse distance of the wavefront, d,

$$\pi > \Delta\phi_{wavefront} = d\frac{d\phi}{dy}. \tag{2.40}$$

The derivative, $d\phi/dy$, is again calculated using Equation 2.33, leading to the following condition on the probe beam wavelength,

$$\lambda < \frac{\pi}{2r_e d}\left[\int \frac{dn_e}{dy}dx\right]^{-1}. \tag{2.41}$$

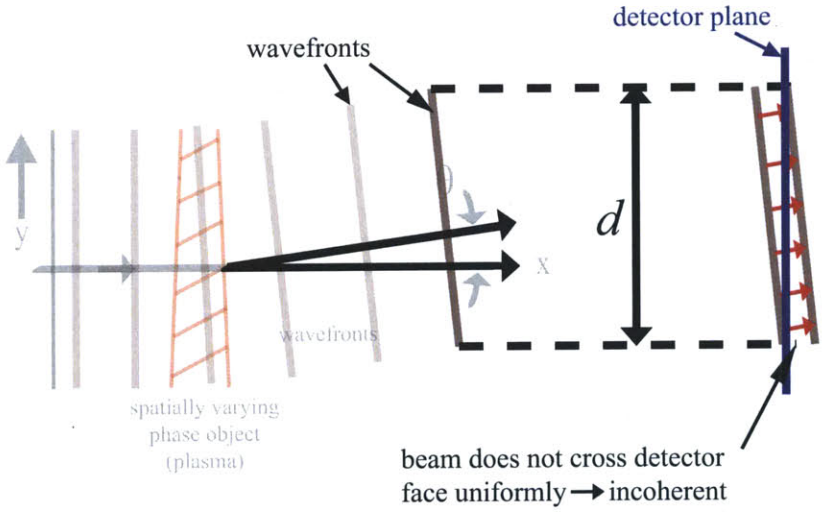

Figure 2-3: Diagram showing how a refracted wave can lose coherence across a detector.

Some values can be used to give a rough approximation of the wavelength constraint for a "worst-case" scenario in a tokamak plasma. The transverse distance of the beam, d, is about 10 cm. The steepest transverse density gradient occurs in the pedestal region, where one edge of the beam will be in plasma while the other remains

in vacuum. The transverse gradient is approximately,

$$\frac{dn_e}{dy} \approx \frac{1 \times 10^{20}\ \mathrm{m}^{-3}}{d}.$$

The distance of propagation, dx, is approximately the pedestal width which is about 1 cm. With these parameters, the wavelength constraint is approximately,

$$\lambda < 557\ \mu\mathrm{m}. \tag{2.42}$$

Refraction can also cause the probe beam to completely miss the detector plane, but the wavelength requirement arising from this condition is less constraining than for the beam to remain coherent.

2.2.4 Discussion

The probing beam wavelength requirements arising from beam refraction and signal-to-noise considerations is 0.15 μm $<< \lambda <$ 557 μm. Ideally, the chosen wavelength will be near the center of this range and will be a laser that is commercially available and, preferably, inexpensive. CO_2 lasers at $\lambda = 10.6$ μm are widely available and fall safely within the required wavelength range, far from coherence and signal-to-noise limitations.

However, vibration effects have not yet been considered. On Alcator C-Mod, a typical optical mirror vibration has a length scale of about 10 μm. At a wavelength of 0.15 μm, this corresponds to 420 rads of vibrational signal but only 0.087 rads of plasma-induced signal for a line-integrated density of 1×10^{20} m^{-2}. This is an unacceptable ratio of vibrational to plasma-induced signal, and thus short-wavelength laser systems are not an option. At 557 μm there is only 0.1 rads of vibrational signal and 314 rads of plasma-induced signal. This is a very lucrative signal-to-noise ratio, but in Alcator C-Mod plasmas the refraction effects would still be significant at 557 μm, especially during violent plasma phenomena like disruptions. Thus, near-millimeter-wave interferometer systems are also not viable.

The CO_2 wavelength of 10.6 μm has 5.9 rads of vibrational signal and 6.0 rads of plasma-induced signal. By itself, this is an unacceptably high level of error. However, recall that the short 0.15 μm wavelength was virtually insensitive to the plasma but highly sensitive to vibrational effects. A short wavelength laser could therefore be used to characterize the vibration effects while another laser is used to measure plasma-induced effects (with contamination by vibration). The effects of vibration are removed from the plasma-probing beam, providing a great measurement of the plasma line-integrated density. This technique is called two-color interferometry.

2.3 Vibration Compensation

Using two different wavelengths to measure only the plasma-induced phase shift is very straightforward in theory and can be easily demonstrated. Two lasers with different wavelengths are assumed to measure both vibrational and plasma-induced phase shifts,

$$\phi_{1,meas} = \phi_{1,v} + \phi_{1,p} \tag{2.43}$$

$$\phi_{2,meas} = \phi_{2,v} + \phi_{2,p}. \tag{2.44}$$

The subscripts v and p correspond respectively to the vibrational and plasma-induced components of the total measured phase shift, which is denoted with the *meas* subscript.

In Section 2.1 the plasma-induced phase shift was shown to be proportional to the wavelength of the probing beam. With this information the plasma-induced components of the two wavelength measurements can be related by,

$$\phi_{2,p} = \frac{\lambda_2}{\lambda_1}\phi_{1,p}. \tag{2.45}$$

Similarly, in Section 2.2 it was shown that the vibrational component of the phase shift is proportional to the inverse of the wavelength. With this information the

vibrational components of the two wavelengths can be related by,

$$\phi_{1,v} = \frac{\lambda_2}{\lambda_1}\phi_{2,v}. \tag{2.46}$$

The system is now completely determined in terms of measured quantities and wavelengths. Solving for $\phi_{1,p}$, the plasma-induced phase shift of one wavelength, will yield the necessary expression to subtract off the vibrational component. First, solve Equation 2.44 for the plasma-induced phase shift:

$$\phi_{1,p} = \phi_{1,meas} - \phi_{1,v}.$$

Defining $\alpha = \lambda_2/\lambda_1$ and using Equation 2.46 gives,

$$\phi_{1,p} = \phi_{1,meas} - \alpha\phi_{2,v}.$$

Solving Equation 2.44 for $\phi_{2,v}$ and substituting gives,

$$\phi_{1,p} = \phi_{1,meas} - \alpha(\phi_{2,meas} - \phi_{2,p}).$$

Substituting Equation 2.45 and solving for $\phi_{1,p}$ gives the final expression,

$$\phi_{1,p} = \frac{\phi_{1,meas} - \alpha\phi_{2,meas}}{1-\alpha^2}. \tag{2.47}$$

Since longer wavelengths are more sensitive to plasma-induced phase shifts, the subscript 1 is taken to be the signal derived from the longer wavelength laser and the subscript 2 is the shorter wavelength measurement. An example of the success of two-color vibration subtraction is shown in Figure 2-4. The blue line is the measured phase shift in Alcator C-Mod using a 10.6 μm CO_2 laser and the red line is the measured phase shift using a 633 nm helium-neon (HeNe) laser multiplied by the α-factor. The black line is the plasma-induced phase shift calculated with Equation 2.47. The black line is proportional to the line-integrated electron density using Equation 2.33, where the negative sign has already been applied for visual clarity.

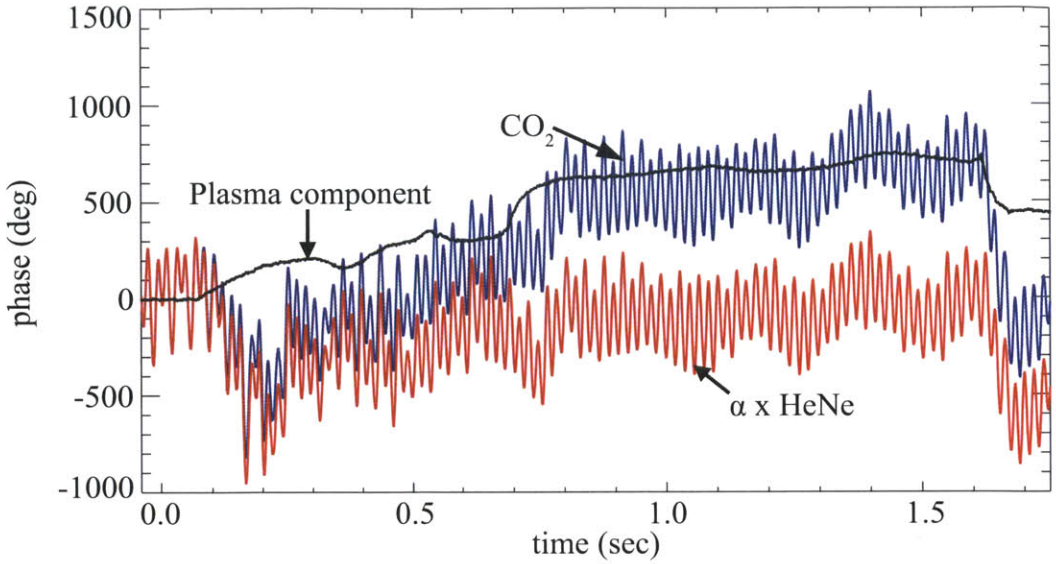

Figure 2-4: Example of successful two-color vibration subtraction. The blue line is the measured phase shift using a 10.6 μm CO_2 laser and the red line is the measured phase shift using a 633 nm helium-neon (HeNe) laser (multiplied by $\alpha = \lambda_{CO_2}/\lambda_{HeNe}$). The black line is the plasma-induced signal calculated with Equation 2.47.

2.4 Measurement of TCI Phase Shift

Phase measurements at optical frequencies are very difficult, so typically an optical heterodyne detection technique is applied. In heterodyne detection interferometry, the plasma and reference arms are given a slight frequency difference using a nonlinear optical element called an acousto-optic modulator (AOM). The electric fields of the plasma and reference arms can be written generally,

$$\begin{aligned} E_p(t) &= E_p \cos(\omega t - \phi) \\ E_r(t) &= E_r \cos(\omega t + \Delta\omega_{LO} t). \end{aligned}$$

The quantity ω is the frequency of the laser and ϕ is the phase shift acquired from traversing the plasma (and also due to vibration). The frequency $\Delta\omega_{LO}$ is the heterodyne frequency difference imparted by the AOM. "LO" stands for Local Oscillator, which is the RF source used to drive the AOM and impart the frequency difference to the plasma and reference arms.

The detectors used to measure the recombined plasma and reference arms are sensitive to the intensity of the combined signal, not the electric field. The detected power density is thus proportional to $E(t)^2$, where $E(t) = E_p(t) + E_r(t)$ is the sum of the electric fields of the plasma and reference arms,

$$P \propto E_r^2 \cos^2(\omega + \Delta\omega_{LO})t + E_p^2 \cos^2(\omega t - \phi) + 2E_r E_p \cos(\omega t + \Delta\omega_{LO} t) \cos(\omega t - \phi).$$

Using the product-to-sum trigonometric identity,

$$\cos A \cos B = \frac{\cos(A - B) + \cos(A + B)}{2}$$

the detected power density equation can be rewritten as,

$$P \propto E_r^2 \cos^2(\omega + \Delta\omega_{LO})t + E_p^2 \cos^2(\omega t - \phi) + E_r E_p \Big(\cos(\Delta\omega_{LO} t + \phi) + \cos(2\omega t + \Delta\omega_{LO} t - \phi) \Big). \quad (2.48)$$

In this equation, ω is an optical frequency in the THz range and $\Delta\omega_{LO} = 2\pi f_{LO}$ is the local oscillator frequency, which is $f_{LO} = 40$ MHz on Alcator C-Mod.[1] The signal of interest is the 40 MHz heterodyne signal with the plasma (and vibration) induced phase shift, ϕ. A simple bandpass filter around 40 MHz removes the high frequency components (as well as spurious harmonics of the 40 MHz signal arising from the use of nonlinear optics). The resulting signal has a dc component, but the oscillating component is,

$$P \propto \cos(\Delta\omega_{LO} + \phi). \quad (2.49)$$

The final filtered signal is proportional to only the 40 MHz LO oscillation, and the plasma (and vibration) induced phase shift can be extracted by comparing this signal to the LO. The phase demodulation relative to the LO is accomplished with the electronics described in Chapter 3.

2.5 Multi-chord vs. Imaging Interferometry

There is often confusion about the difference between a standard interferometer and an interferometric imaging system. The former measures both the total phase shift and phase fluctuations along a chord, providing measurements of the line-integrated electron density and fluctuations. Imaging systems detect only line-integrated electron density fluctuations.

The output of a single detector element of an interferometric imaging system is,[24]

$$V(t) \propto \cos(\phi - \delta\phi), \tag{2.50}$$

where ϕ is the phase difference between the plasma and reference arms and $\delta\phi$ is due to electron density fluctuations. The quantity ϕ, which in a standard interferometer system is a measured quantity, is instead held constant at $\pi/2$ using feedback control. By holding ϕ constant at this value, the overall system sensitivity to fluctuations is maximized; the voltage signal becomes,

$$\begin{aligned} V(t) &\propto \cos(\pi/2 - \delta\phi) \\ \Rightarrow V(t) &\propto \sin(\delta\phi). \end{aligned} \tag{2.51}$$

For small fluctuations typically found in tokamak plasmas, to a good approximation Equation 2.51 becomes,

$$V(t) \propto \delta\phi. \tag{2.52}$$

The output voltage of the detector is proportional to the fluctuating phase, which is proportional to the fluctuating density. Thus, an array of detectors will effectively image the (line-integrated) electron density fluctuations.

Now consider a standard interferometer system used to measure the background electron density, such as the TCI system on Alcator C-Mod. From Equation 2.49, the output of a detector is proportional to the cosine of the LO phase and the plasma-

induced phase,

$$V(t) \propto \cos\left(\Delta\omega_{LO} + \phi + \delta\phi\right) \tag{2.53}$$

where the plasma-induced phase has now been explicitly separated into background and fluctuating components, and vibration effects have been neglected. Chapter 3 will describe an analog technique of removing the LO signal, which is possible because it is well-known from an external source. This process transforms a single detector output into two signals,

$$\begin{aligned} V_1(t) &\propto \cos\left(\phi + \delta\phi\right) \\ V_2(t) &\propto \sin\left(\phi + \delta\phi\right). \end{aligned} \tag{2.54}$$

Unlike with an imaging system, where ϕ is well-known because it is set externally, in a standard interferometer system ϕ is an unknown quantity; in fact, it is a desired measurement. Thus, the fluctuating component cannot be separated from the background component. As a result, the output signals do not form an image of the fluctuating phase wavefront. Instead, the fluctuating phase must be determined from Fourier analysis.

Interferometric imaging systems are complicated to implement because of the requirement to keep $\phi = \pi/2$.[24] The beam path must be completely isolated from sound and vibration effects, and beam quality requirements are stricter than for standard interferometers. When successfully implemented, however, imaging systems are very sensitive to electron density fluctuations, having sensitivities approaching the levels of phase-contrast imaging.[44] In contrast, standard interferometers are very simple to implement, and vibration effects can be mitigated. The cost of that simplicity, however, is reduced sensitivity. Despite some lost sensitivity, standard interferometers can still be used to measure line-integrated electron density fluctuations, as the remainder of this thesis will demonstrate.

Chapter 3

TCI Experimental Design

The two-color interferometer (TCI) diagnostic on Alcator C-Mod has been in use since 1988[1] but was last described in detail in 1994,[71] and in the ensuing two decades several significant changes have been made.[2] Section 3.1 describes the hardware and optics in use in 2012, and Section 3.2 outlines the basic electronics. A significant electronics upgrade which provides the capability to measure electron density fluctuations is described in Section 3.3. The new electronics require a revamped post-processing analysis routine, which is introduced in Section 3.4.

3.1 Hardware

The TCI optics system is shown in Figure 3-1. The primary radiation source is a 60 W, horizontally polarized, continuous wave CO_2 laser tuned to the 10.6 μm line. The laser is very sensitive to atmospheric changes, so a piezo-electric tuner (PZT) was installed to control the length of the cavity and thus the stability of the laser. Laser stability is monitored by splitting the output power with a 50/50 beam splitter and directing half the power to a detector. The detector signal is monitored from the control room and the voltage of the PZT is adjusted to maintain laser stability. Typically the PZT needs to be adjusted during the beginning of a run day when the temperature of the test cell is equilibrating, but the laser will usually stabilize and remain well-behaved for long periods of time thereafter.

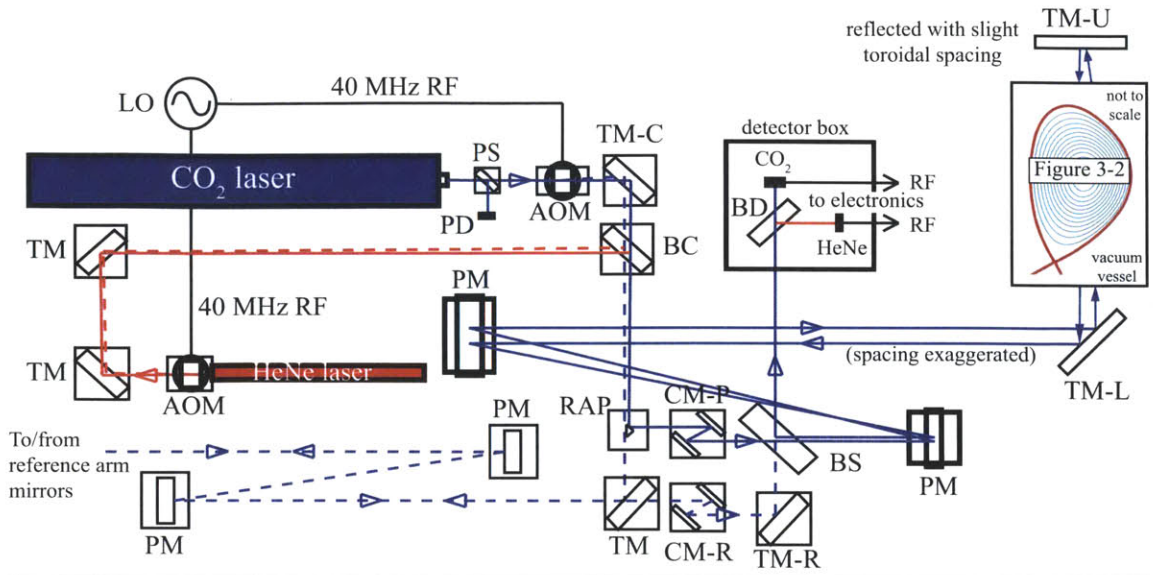

AOM	Acousto-Optic Modulator	PM	Parabolic Mirror
BC	Beam Combiner	PS	Power Splitter
BD	Beam Divider	RAP	Right-Angle Prism
BS	Beam Splitter	TM	Turning Mirror
CM-P	Cylindrical Mirror - Plasma arm	TM-C	Turning Mirror - CO_2
CM-R	Cylindrical Mirror - Reference arm	TM-L	Turning Mirror - Lower
LO	Local Oscillator	TM-R	Turning Mirror - Ref.
PD	Power Detector	TM-U	Turning Mirror - Upper

Figure 3-1: TCI optics layout.

The portion of the CO_2 beam not directed to the power detector travels through a water-cooled acousto-optic modulator (AOM) or "Bragg cell." Inside the AOM, a longitudinal acoustic wave is driven through a germanium crystal by a high-power radio-frequency (RF) source. The acoustic wave acts as a moving diffraction grating and imparts a frequency offset to the diffracted beam that is equal to the RF source frequency. The AOM (NEOS Technologies model no. N37040-6-10.6-NI) has a 6 mm nickle-plated aperture and transmits $\sim$ 90% of incident 10.6 μm light. The AOM is driven by a 50 W, 40 MHz "local oscillator" (LO) (NEOS Technologies 19040.00-50DSA05-REF). Roughly half of the laser power incident on the AOM is diffracted an angle of 77 mrad with a 40 MHz frequency offset (the first-order beam), and the remaining power is not shifted or diffracted (the zero-order beam).

The vibration compensation is accomplished with a 633 nm helium-neon (HeNe) laser. The HeNe beam is sent through an AOM driven by the same RF source as the CO_2 AOM. The beam is split into zero- and first-order beams with a 40 MHz frequency offset. Because of the different wavelengths, the first-order HeNe beam has a much smaller diffraction angle than the first-order CO_2 beam. The zero- and first-order HeNe beams are made co-axial with the zero- and first-order CO_2 beams (respectively) by two 4 in. diameter BK7 90° turning mirrors coated with Enhanced Protected Silver (EPS). The mirrors steer the beams onto a set of two zinc-selenide (ZnSe) beam combiners (BCs) coated to reflect greater than 90% of the 633 nm light and pass more than 90% of the CO_2 light.

After the zero- and first-order CO_2 beams exit the AOM, they hit a pair of 0.75 in. diameter BK7 glass turning mirrors coated with Protected Gold (OptoSigma no. 033-4650). The mirrors have greater than 95% reflection at 10.6 μm. After reflecting off the gold-coated turning mirrors, the zero- and first-order beams are aligned with the zero-and first-order HeNe beams. Each beam passes through the ZnSe BCs where they join the zero- and first-order HeNe beams.

The combined CO_2 and HeNe beams travel toward a right-angle prism made of EPS-coated BK7 glass. The zero-order beam hits the right-angle prism and is directed toward the plasma arm, and the first-order beam misses the prism and is directed toward the reference arm.

After reflecting off the right-angle prism, the plasma arm is expanded with a pair of N-BK7 cylindrical mirrors with EPS coatings. The beam first hits a plano-convex cylindrical mirror (Melles Griot no. 01 LCP129) with a +38.1 mm focal length, which expands the beam in the vertical (major-radial) direction. The beam is then partially collimated with a plano-concave cylindrical mirror (Melles Griot no. 01 LCN012) with a -300 mm focal length. At this point the beam is an ellipse approximately 5 cm high and 7 mm wide. Next the beam reflects off a pair of BK7 parabolic mirrors with EPS coatings. The parabolas provide additional vertical expansion and also a small amount of horizontal (toroidal) expansion, and the resulting beam is collimated. At this point the beam is approximately 10 cm high and 1 cm wide. After the second

parabolic mirror the beam is sent to an EPS-coated 90° BK7 turning mirror located directly below the Alcator C-Mod vacuum vessel. The beam is turned upward where it travels through a vacuum window, the C-Mod vessel, and another vacuum window, as shown in the upper right corner of Figure 3-1. The size and position of the beam through the plasma (to scale) is shown in Figure 3-2.

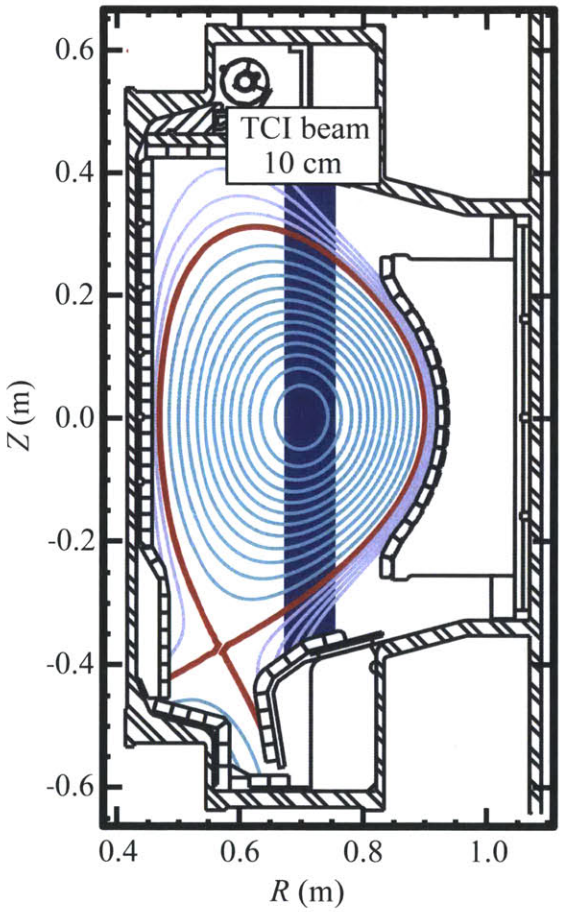

Figure 3-2: TCI beam size and position through the plasma.

The vacuum windows are made of ZnSe and have anti-reflective coating which transmits greater than 98% of the CO_2 light and greater than 92% of the HeNe light. At the top of the Alcator C-Mod vessel, the beam hits an EPS-coated BK7 mirror which sends the beam back through the vacuum vessel with a slight toroidal displacement. The beam is down-collimated by both parabolic mirrors, but does not

reach the cylindrical mirrors because the slight toroidal displacement instead directs the beam to a beam splitter. The beam splitter reflects $\sim 50\%$ of the CO_2 light and $\sim 50\%$ of the HeNe light. The beam is reflected 90°, combines with the reference beam, and travels toward a box which houses detectors.

After missing the right-angle prism, the reference arm first hits a 90° turning mirror and is directed to a pair of EPS-coated BK7 parabolic mirrors which slightly expand the beam. From the parabolas, the beam is directed to a series of EPS-coated 4 in. diameter BK7 turning mirrors. The total path length of the reference arm is matched to within 1 cm of the plasma arm by adjusting the spacing of the 4 in. mirrors. The final mirror is oriented for $\sim 180°$ reflection. The reference beam is given a slight horizontal displacement by the final mirror which allows the beam to miss the first turning mirror on its return path. The beam instead hits two EPS-coated BK7 cylindrical mirrors: first a plano-convex mirror (Melles Griot no. 01 LCP136, $f = +60$ mm), then a plano-concave mirror (Melles Griot no. 01 LCN012, $f = -300$ mm). The cylindrical mirrors match the size of the reference beam to the size of the plasma beam after the cylindrical optics in the plasma arm. After exiting the cylindrical mirrors, the reference beam is directed to the beam splitter with another turning mirror. The turning mirror reflects 95% of the CO_2 beam and 90% of the HeNe beam, allowing 10% of the HeNe portion to pass through. The back surface of the mirror has an anti-reflective coating optimized to transmit 99.9% of the HeNe wavelength. The portion of the HeNe beam which passes through the mirror hits a position sensor that is used for feedback control. The rest of the reference arm passes through the beam splitter, where it is made co-linear with the plasma arm.

The recombined plasma and reference arms enter the detector box and hit a ZnSe beam divider, where the CO_2 and HeNe beams are separated and directed onto their respective detectors. The CO_2 detector consists of an array of ten mercury-cadmium-telluride (HgCdTe) semiconductors custom-manufactured for Alcator C-Mod by Boston Electronics Corporation with detectors from Vigo System S.A. The dimensions of the HgCdTe detector array are shown in Figure 3-3. Each semiconductor element has an active area of 2×2 mm^2, and elements are separated by 4 mm

(center-to-center). The voltage responsivity is between $0.1 - 0.13$ V/W, the voltage noise density is less than 1 nV/Hz$^{1/2}$ and the detectivity is between $2.1 - 2.7 \times 10^7$ cmHz$^{1/2}$/W. The CO_2 detector array is placed directly after the ZnSe beam-splitter in the detector box, so each detector element maps to a specific plasma major radius within the beam fan shown in Figure 3-2.

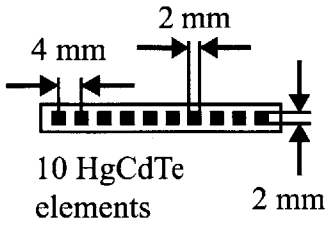

Figure 3-3: The dimensions of the 10 element mercury-cadmium-telluride (HgCdTe) CO_2 detector array.

The HeNe detector is an array of four fiber optic cables which collect light from discrete points along the HeNe beam and couple the light to four avalanche photodiodes (APDs) (RCA Electronics no. C30950FL). The APDs have a voltage responsivity of $1 - 2$ V/W, and the four HeNe channels are chosen to map to positions 3 through 6 of the CO_2 array. The only purpose of the HeNe channels is to characterize the vibration-induced phase-shift. The vibration effects come mostly from the upper and lower mirrors (TM-U and TM-L in Figure 3-1), with some additional magnetic field-induced vibrations of the optical table. The vibrational effects are mostly linear, so four HeNe channels are more than sufficient to characterize the vibration of optical elements across all ten CO_2 channels; typically only two HeNe channels provide adequate vibration subtraction.

3.2 Electronics

The CO_2 and HeNe detectors are sensitive to the power in the combined plasma arm and reference arm signals, which is modulated at the 40 MHz local oscillator frequency with higher frequency and dc components (Equation 2.48). The phase shift between the plasma and reference arms is hidden within the 40 MHz modulation at this stage.

The signals from the detectors follow the path outlined in Figure 3-4. First the signals are amplified with automatic gain control (AGC) amplifiers (RHG Electronics Laboratory no. EST40A22DB). The AGC amplifiers have a maximum voltage gain of around 80 dB and are used to increase the amplitude of the electronic signals from the millivolt range to the volt range. The AGCs also contain an 11 MHz wide 40 MHz bandpass filter which eliminates low- and high-frequency components, leaving a signal modulated by only the 40 MHz local oscillator (LO),

$$x(t) \propto \cos\left(\Delta\omega_{LO} t + \phi\right) \tag{3.1}$$

where $\Delta\omega_{LO} = 2\pi(40 \times 10^6)$ s^{-1} and ϕ is the plasma-induced phase shift (with contributions from vibrations).

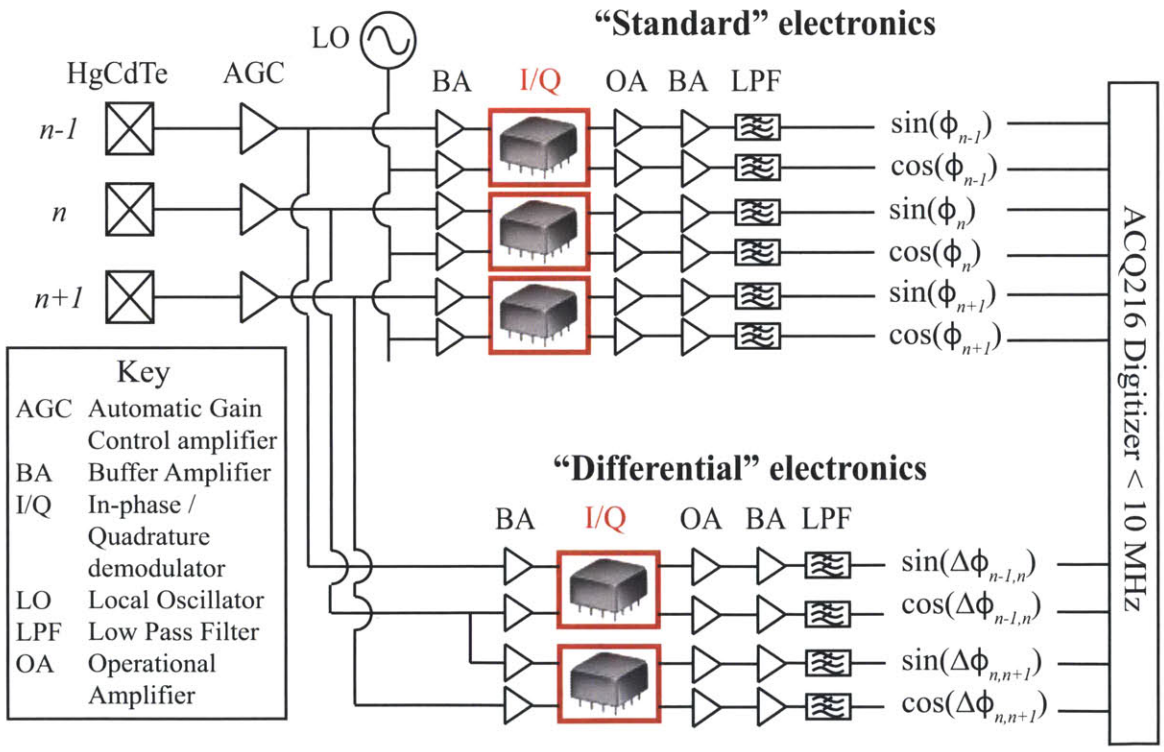

Figure 3-4: TCI electronics schematic.

After being amplified and filtered in the AGCs, the signals are split, with part of the power going to the "standard" electronics and the rest to the "differential" electronics. The standard electronics are used to measure the line-integrated electron

density and fluctuations. In the standard electronics branch, the signals are first amplified with a buffer amplifier (Texas Instruments no. BUF634). The buffer amplifiers allow the signals and the LO to be fed to the differential system without a significant loss of signal power. After amplification each signal is sent to an input of an analog in-phase/quadrature (I/Q) mixer (Mini-Circuits no. MIQC-60WD), where it is mixed with the 40 MHz LO signal. The outputs of the I/Q mixer are proportional to the sine and the cosine of the phase shift of the plasma arm relative to the reference arm, which contains both vibrational and plasma-induced components. The sine and cosine outputs are amplified with a high speed, high bandwidth operational amplifier (Analog Devices no. AD829) and another buffer amplifier (Texas Instruments no. BUF634), and are then digitized at up to 10 MHz (D-tAcq Solutions no. ACQ216). The phase shift and line-integrated electron density are calculated in software.

The differential electronics are used to measure the line-integrated electron density gradient and fluctuations. This system is not the topic of this thesis, but more information can be found in Appendix B.

The signals from the HeNe detectors are sent through the same electronics as the standard CO_2 electronics described above, but they are not fed to a differential system. The four HeNe channels are demodulated relative to the 40 MHz local oscillator and are digitized with the same digitizers as the CO_2 signals.

Several digitizer channels were observed to occasionally return a bad data point in a time series. Typical signals are in the 1-3 volt range, and periodically a digitizer channel would include a data point near the rail voltage of ± 10 volts. These events are very rare, occurring less than ten times in 4×10^7 data points. Replacing or fixing the digitizer channels exhibiting these errors was not practical or necessary for this error rate, so the errors are simply replaced with the average of the two data points immediately before and after the bad point.

3.3 Phase Demodulators

The I/Q phase demodulators were the most significant hardware change made to the TCI diagnostic over the course of this thesis work, and as a result considerable effort was made to fully characterize them. The outputs of an I/Q module are most generally described by,

$$I(t) = A_1 \sin(\phi(t) + d\phi_1) + dA_1 \tag{3.2}$$

$$Q(t) = A_2 \cos(\phi(t) + d\phi_2) + dA_2. \tag{3.3}$$

The amplitudes, A_i, can be adjusted by changing the gains of the amplifiers following the demodulators shown in Figure 3-4. The gains are set so that A_1 and A_2 are equal. A demodulator may also have an inherent phase offset, $d\phi_i$, and dc offset, dA_i. All of these quantities contribute to the overall phase calculation, as is now shown.[72]

The phase from the I and Q signals contains the measured phase, ϕ, and an error, $\delta\phi$,

$$\phi + \delta\phi = \tan^{-1}(I/Q). \tag{3.4}$$

An expression for $\delta\phi$ can be derived if $\delta\phi$ and $d\phi_i$ are assumed to be small. First, using the following trigonometric identities,

$$\sin(A+B) = \sin A \cos B + \sin B \cos A \tag{3.5}$$

$$\cos(A+B) = \cos A \cos B - \sin A \sin B \tag{3.6}$$

the expressions for I and Q (Equations 3.2 and 3.3) can be expanded in Equation 3.4,

$$\phi + \delta\phi = \tan^{-1}\left(\frac{A_1[\sin\phi\cos d\phi_1 + \cos\phi\sin d\phi_1] + dA_1}{A_2[\cos\phi\cos d\phi_2 - \sin\phi\sin d\phi_2] + dA_2}\right). \tag{3.7}$$

Introducing the small angle approximations, $\sin\epsilon \approx \epsilon$ and $\cos\epsilon \approx 1$, Equation 3.7 can

be rewritten as,

$$\phi + \delta\phi = \tan^{-1}(D) \tag{3.8}$$

$$D = \frac{A_1\left[\sin\phi + d\phi_1\cos\phi\right] + dA_1}{A_2\left[\cos\phi - d\phi_2\sin\phi\right] + dA_2}. \tag{3.9}$$

Taking the tangent of each side of Equation 3.9 and applying the identities given by Equations 3.5 and 3.6 gives,

$$\begin{aligned} D &= \tan(\phi + \delta\phi) = \frac{\sin(\phi + \delta\phi)}{\cos(\phi + \delta\phi)} \\ &= \frac{\sin\phi\cos\delta\phi + \sin\delta\phi\cos\phi}{\cos\phi\cos\delta\phi - \sin\phi\sin\delta\phi} \\ &= \frac{\sin\phi + \delta\phi\cos\phi}{\cos\phi - \delta\phi\sin\phi} \end{aligned} \tag{3.10}$$

where the approximation that $\delta\phi$ is small has been applied in the final step. Equation 3.10 can be solved for $\delta\phi$, yielding an expression for the phase error as a function of the measured phase, ϕ, and the amplitudes, offsets, and phase imbalances of the I/Q module,

$$\delta\phi = \frac{D\cos\phi - \sin\phi}{D\sin\phi + \cos\phi}. \tag{3.11}$$

This is an important result because it shows that the phase imbalance is not simply the inherent imbalance of the demodulators ($d\phi_i$), but actually depends periodically on the measured phase. In the absence of plasma there can still be a phase shift due to vibration, so even with zero plasma electron density there will be an observed density oscillation that depends on the measured vibrational phase shift.

Analytically determining the phase error of an I/Q module as a function of the measured phase requires knowledge of the values of A_i, dA_i, and $d\phi_i$. The first two quantities, the amplitude and dc offset, are easily measurable. The third quantity, the inherent phase imbalance of a demodulator, is not easy to measure directly. Instead, the total phase error as a function of the measured phase is inferred from calibration data.

The calibration procedure is shown schematically in Figure 3-5. First, two 5

dBm signals with a slight frequency offset (1 kHz) are sent into each input of an I/Q module. The output signals are directly digitized, giving oscillating signals from which the amplitudes and dc offsets can be computed. Each period of the I and Q

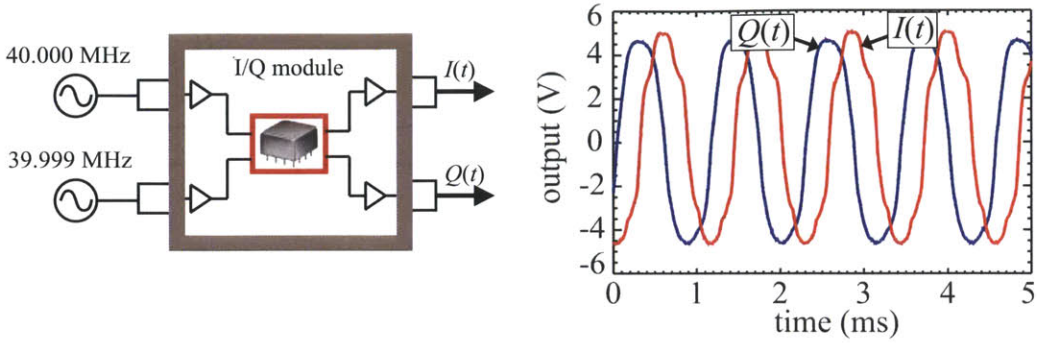

Figure 3-5: TCI I/Q module calibration.

signals shown in Figure 3-5 are first ensemble averaged with every other period. The amplitude is then taken to be one-half of the voltage between the peak and trough of the ensemble averaged wave period, and the dc offset is the mean of the ensemble averaged wave period. The most recent calibration results are shown in Figure 3-6. The important things to note are that the dc offsets are small (less than 2% of the amplitudes) and that the amplitudes of the I and Q outputs for a given chord are almost identical (by design), and therefore the phase imbalance $\delta\phi$ is expected to be small.

The amplitudes of the modules for chords located in the center of the CO_2 detector array (chords $4-7$) are smaller than for chords near the edges of the array. The gains of the I/Q modules are adjusted so that the output signal power from each chord is roughly equal to all other chords when the input signal is derived from the CO_2 beam. Since the CO_2 laser beam has a Gaussian profile, it has more power in the center of the beam than at the edge. Therefore, the gains of the I/Q modules must be turned down for the central chords so the total amplitude matches the signals from the outer chords. When calibration data is taken, the input signal amplitudes are the same for all chords, so the central channels returned a lower amplitude due to the lower gain values.

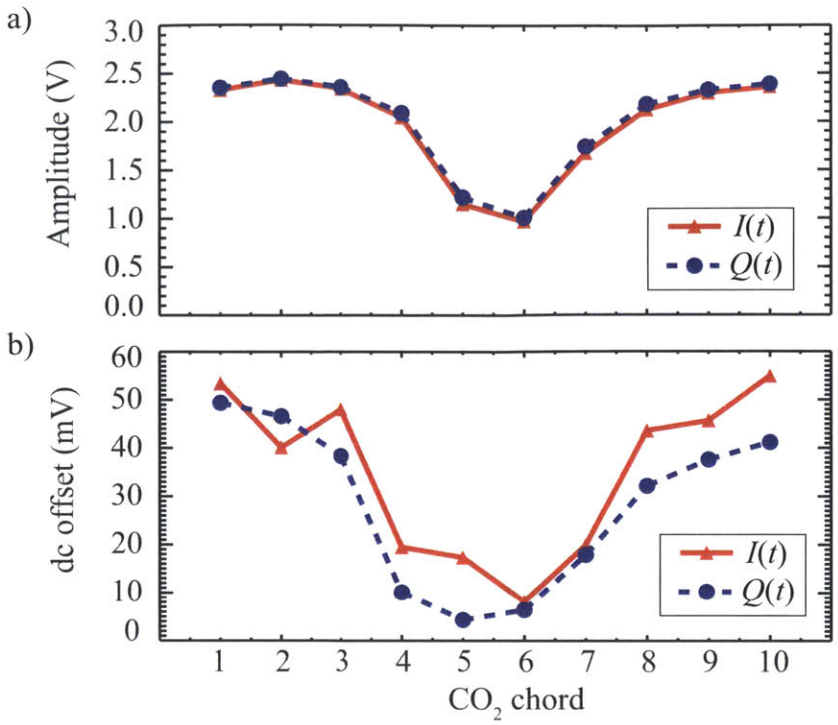

Figure 3-6: TCI I/Q module calibration: (a) amplitudes and (b) offsets. Note that the ordinate ranges differ.

The amplitudes and dc offsets have the trends shown in Figure 3-6 regardless of the choice of intermediate frequency or power of the input signals, provided that the input powers of the two signals are nearly the same. Experimentally, this means that as long as the two input signals analyzed by an I/Q module have similar amplitudes, the I/Q module will have the same phase behavior as observed during the calibration.

The phase of the calibration signals is shown in Figure 3-7. The two-argument IDL arctangent function used to compute the phase is limited to the range between $-180°$ and $+180°$, so the raw phase signal contains many discontinuities, as shown in Figure 3-7(a). Since the phase is derived from two input signals with an $f = 1$ kHz frequency offset, the true phase relationship that should be measured by an I/Q module is known for each period. For any time between the start of the i-th period ($t = t_i$) and the end of that period ($t = t_i + T$), the expected phase is,

$$\phi_{expected} = 2\pi f(t_i + T - t) - \pi$$

where $T = 1/f$ is the period. The expected phase for a single period is shown in red in Figure 3-7(b).

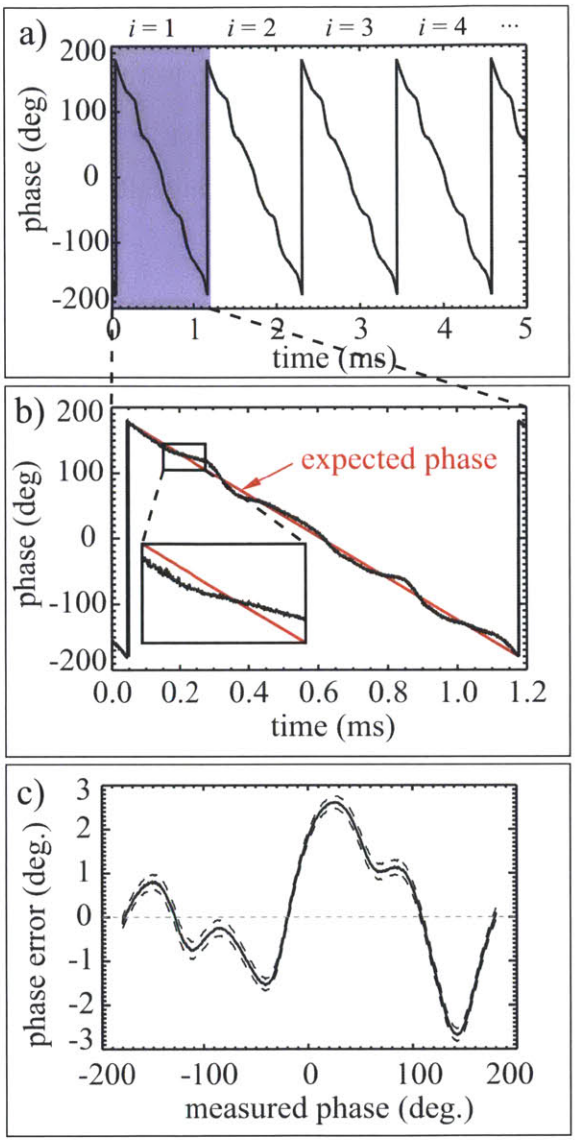

Figure 3-7: TCI I/Q module phase calibration. (a) The raw output of $\tan^{-1}(I/Q)$. (b) A single period of the raw phase signal with the true phase plotted in red. (c) The difference between the true phase and measured phase is the phase error.

The phase imbalance, $\delta\phi$, is determined by ensembling the data from all the periods in a time series and subtracting the measured phase from the expected phase; the result is shown in Figure 3-7(c). All the I/Q modules used in the TCI system have phase errors similar to the one shown. Mini-Circuits quotes a typical phase imbalance

of 1.0° with a maximum of 5°; the quoted values have been verified.

It is thus shown that the phase imbalance is indeed a function of the measured phase as predicted by Equation 3.11. As a result, apparent density fluctuations should appear due to vibration measurements even in the absence of plasma.[72] Such oscillations are observed. Figure 3-8(a) is a line-integrated electron density trace, and Figure 3-8(b) shows a density oscillation occurring after the plasma discharge has ended at $t \sim 1.9$ s.

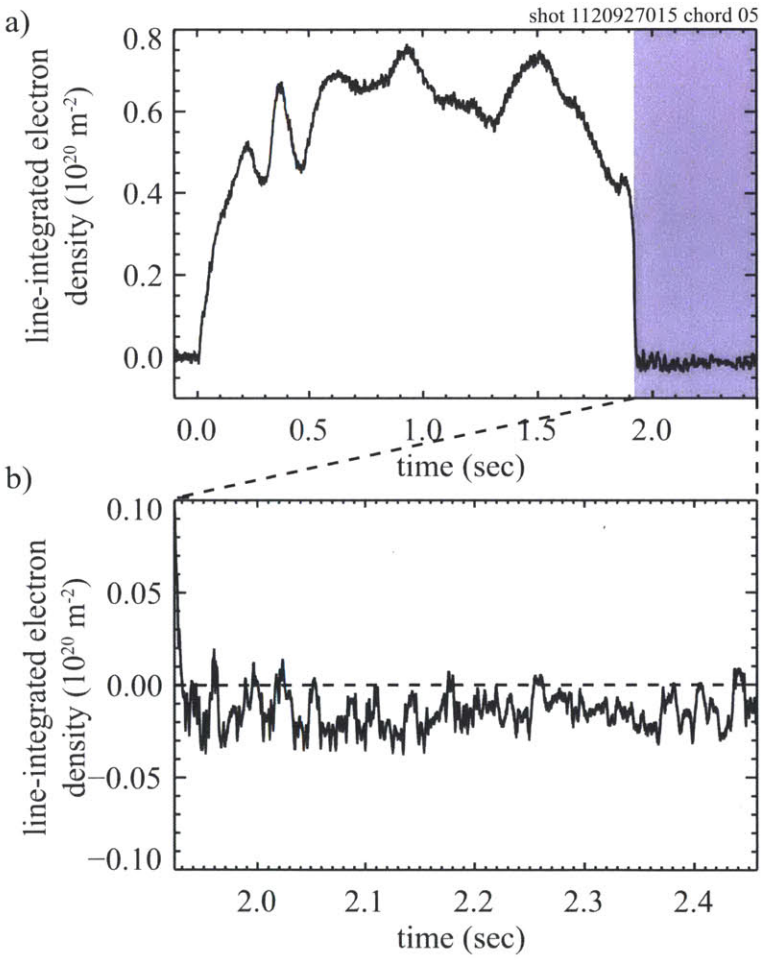

Figure 3-8: (a) Line-integrated electron density measured by a single TCI chord. (b) A density oscillation occurs after the plasma ends.

Visually, there appears to be a recurring feature in the density oscillation at a timescale typical of optical vibrations, which supports the idea that the I/Q module phase imbalance is affecting the measured data as vibrational fringes are detected.

To quantify the I/Q module-induced oscillation, a measurement of the vibration is needed. Data collected from a HeNe channel, which is unaffected by changes in plasma conditions, is used to calculate the optical vibration distance, l, using Equation 2.35,

$$l = \frac{\phi_{HeNe}\lambda_{HeNe}}{2\pi}.$$

The vibration distance is then used with Equation 2.35 to determine the phase shift measured by the CO_2 beam due only to vibrations. This is an independent prediction of the expected phase shift measured by the CO_2 beam in the absence of plasma.

The expected CO_2 phase measurement calculated from vibration data (the "measured phase") is compared to the phase error calculated from post-plasma line-integrated electron density data in Figure 3-8(b) using Equation 2.33. These two time series - the expected measured phase derived from vibrational data and the measured phase error derived from line-integrated density data - have a one-to-one mapping to each other because they are both functions of time, so they can be plotted as a scatter plot. This is done in Figure 3-9. Each triangle represents the phase shift from vibrational data and from line-integrated density data for a single time point in the region following the plasma discharge. The solid red line is a moving average of the phase data with standard deviation given by the dashed red lines. The solid blue line is the calibrated phase error of the I/Q module used to collect the data.

The data trend in Figure 3-9 matches the calibration of the I/Q module reasonably well, which suggests that it should be possible to remove some of the effects of the I/Q module phase imbalance. Unfortunately, in practice this has been difficult to implement because other noise sources tend to obscure the effects of the I/Q module. The quality of the TCI data is currently extremely sensitive to the alignment of the interferometer due to lack of power in the reference arm. The slightest misalignment introduces additional noise. In addition, there remains spurious electronics noise that is not related to the I/Q modules. External noise sources ruin the coherence between the errors inferred from vibration measurements and the errors observed from post-plasma density fluctuations.

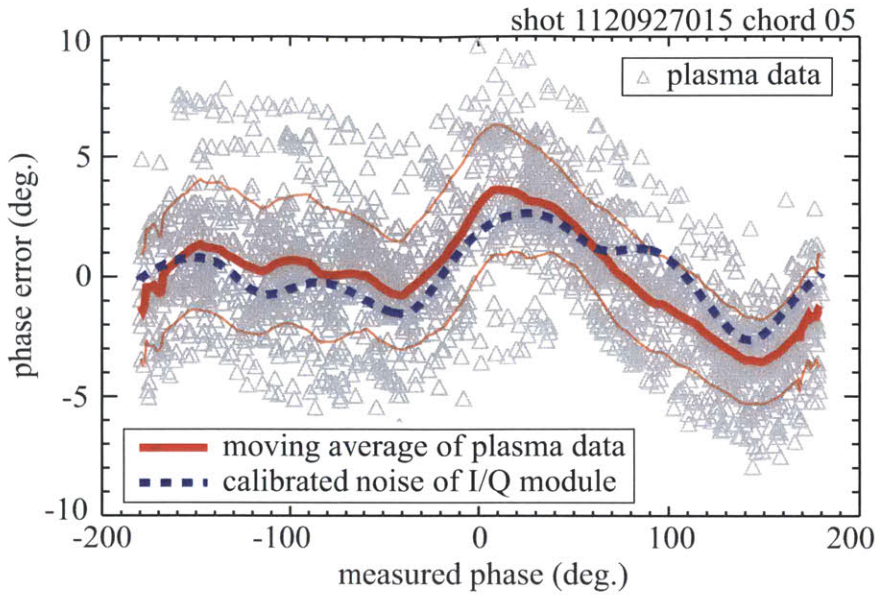

Figure 3-9: A scatter plot of experimental TCI phase measurements. The vertical axis is the CO_2 phase derived from post-plasma line-integrated electron density measurements, and the horizontal axis is the CO_2 phase derived from HeNe vibration measurements. Each gray triangle corresponds to a single time point in the region shown in Figure 3-8(b). The solid red line is the moving average of the data, with error given by the thin red lines. The dashed blue line is the calibrated phase imbalance of the I/Q module.

Since the effects of the phase imbalance introduced by the I/Q modules cannot be robustly removed from line-integrated electron density signals, the best available phase measurement is Equation 3.4, $\phi + \delta\phi = \tan^{-1}(I/Q)$, with uncertainty given by $\delta\phi$. The quoted uncertainty is $|\delta\phi| \leq 5°$, which corresponds to a line-integrated density of $\pm 1.5 \times 10^{18}$ m^{-2}. This is the dc error which takes into account sub-kilohertz phase imbalances; the uncertainty associated with electron density fluctuations will be lower, and will be discussed in Chapter 4.

3.4 Software

As mentioned in Section 3.3, the phase calculation from digitized I/Q module outputs is performed in software with a two-argument arctangent function which is limited to $-180°$ to $+180°$. Phase shifts due to plasma electron density alone can be sufficient

to exceed this range, and when the effects of vibration and an arbitrary phase offset are introduced, the range is always exceeded. The HeNe signals always exceed the range due to their extreme sensitivity to vibration. As a result, the raw output from an arctangent function contains many discontinuities which must be adjusted to give a smooth line-integrated electron density trace. An example of the raw output of an arctangent function is shown in Figure 3-10.

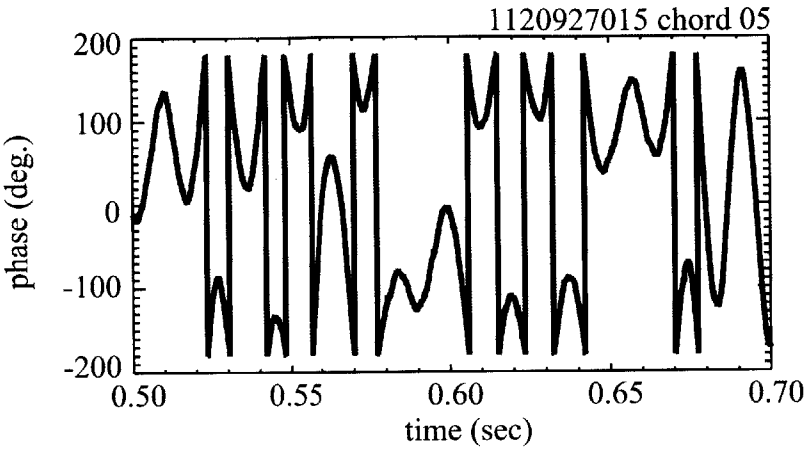

Figure 3-10: Raw output from the two-argument IDL arctangent function with the digitized sine and cosine signals as inputs.

A routine was developed to correct phase discontinuities. First, the routine subtracts adjacent phase values and stores the indices where the magnitude of the difference exceeds π. The sign of the difference is also stored. The phase at the locations where the discontinuities occur is adjusted serially beginning at the start of the time series. A counter is incremented positively (negatively) if the discontinuity goes from a positive (negative) phase to negative (positive) phase. The counter thus keeps track of the total number of positive (or negative) fringes detected by the I/Q module, which determines the total amount of phase correction applied at each discontinuity. The result of the phase correction process is shown in Figure 3-11. The black line is the corrected phase measurement and the red line is the raw output of the arctangent function.

The new software handles a number of other tasks, including extrapolating the HeNe phase data to the CO_2 chord positions, optimizing vibration subtraction, and

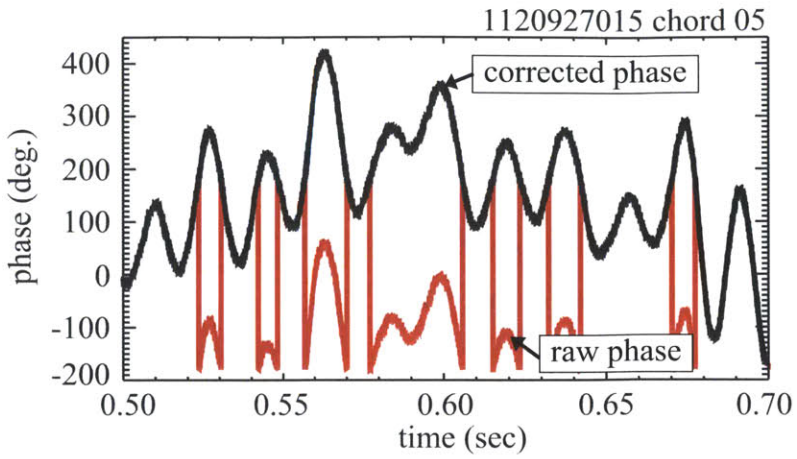

Figure 3-11: The corrected phase from the two-argument IDL arctangent function output.

handling poor quality data. The routine is explained in detail in Appendix A.

Chapter 4

Characterization as a Fluctuation Diagnostic

The following chapter describes the fluctuation sensitivity and wavenumber resolution of the upgraded two-color interferometer. The uncertainty at the fluctuation measurement time scale due to the new phase demodulation electronics is described, and the analysis techniques used to extract fluctuation information from TCI measurements are presented with examples.

4.1 Sensitivity and Resolution

Diagnostics which measure fluctuations at several different spatial locations can be analyzed using data from only a single channel or with data from multiple channels. The wavenumber sensitivity and resolution will vary depending on the method of analysis. However, regardless of the type of analysis being performed, only two TCI hardware components are responsible for the wavenumber sensitivity and resolution. The dimensions of the CO_2 detector array and the magnification provided by the two parabolic mirrors described in Section 3.1 completely determine the spatial resolution of the diagnostic.

The CO_2 detector array dimensions were described in Section 3.1 and are repeated here: a single chord has a width equal to 2 mm and is located 4 mm from adjacent

chords. Figure 4-1 shows how the CO_2 beam gets expanded with a magnification $M \sim 2.5$ by parabolic mirrors. The beam expansion increases the chord spacing and width by the factor M in the plasma, so the true major-radial extent of a single chord is 2 mm $\times$ M = 5 mm and the chord spacing is 4 mm $\times$ M = 1.0 cm.

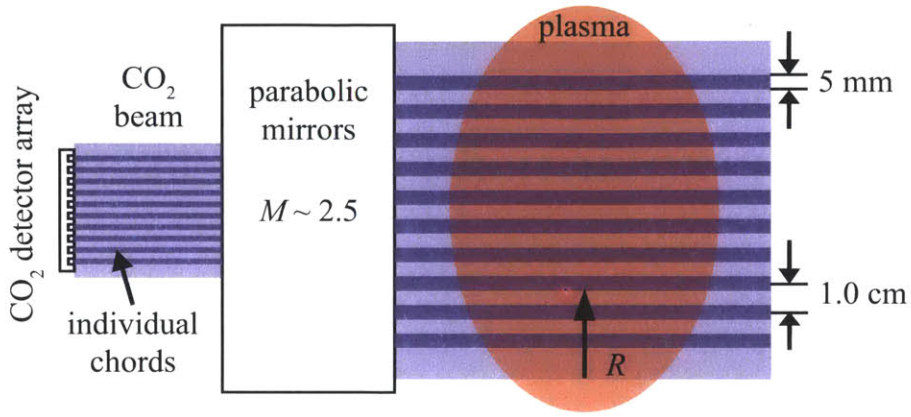

Figure 4-1: The TCI chord spacing through the plasma is determined by the magnification of the parabolic mirrors and the dimensions of the CO_2 detector array.

A detector that is sensitive to the total power incident on its active area will be most sensitive to fluctuations that have a wavelength greater than the width of the detector. A single TCI detector is therefore sensitive to fluctuation wavelengths ranging from infinite (the background density) to λ = 5 mm when M = 2.5. Thus, the wavenumber sensitivity of a single chord, $k_{R,sc}$, is,

$$k_{R,sc} \leq \frac{2\pi}{\lambda} = \frac{2\pi}{0.5 \text{ cm}} = 12.6 \text{ cm.}^{-1} \tag{4.1}$$

When multiple TCI chords are correlated with each other, different spatial scales can be resolved. The outermost chord had very low signal levels for the data collected in this thesis and did not provide any meaningful data, so it is omitted from further analysis. The maximum resolvable wavelength corresponds to the wavenumber resolution, Δk_R. For N = 9 chords spaced a distance of ΔR = 1.0 cm, the wavenumber resolution is,

$$\Delta k_R = \frac{2\pi}{\lambda_{max}} = \frac{2\pi}{N\Delta R} = 0.7 \text{ cm.}^{-1} \tag{4.2}$$

Positive and negative wavenumbers correspond to different directions of propagation in tokamak plasmas and are thus important to differentiate. For an odd number of chords, the maximum resolvable wavenumber while maintaining the ability to resolve direction is,

$$|k_R|_{max} = \frac{N-1}{2}\Delta k_R = 2.8 \text{ cm.}^{-1} \tag{4.3}$$

The resolved wavenumbers are,

$$k_R = -|k_R|_{max} + \Delta k_R \times i \qquad (i = 0, N-1). \tag{4.4}$$

4.2 Uncertainty at Fluctuation Time Scale

Similar to the background density measurements presented in Section 3.3, fluctuation measurements also have uncertainty due to errors in the phase measurement. The uncertainty is determined by examining the phase error of the I/Q demodulators at the fluctuation time scale. Drift-wave fluctuations have frequencies greater than 10 kHz and are typically below $\tilde{n}_e L \leq 10^{17}$ m^{-2}, corresponding to a phase fluctuation of $\tilde{\phi} = \pm 0.17°$ (from Equation 2.33). (Magnetohydrodynamic fluctuations below 10 kHz may also be of interest, but are not the topic of this thesis.) The uncertainty in the phase calculation of fluctuation measurements due to I/Q module phase errors is,

$$\delta\tilde{\phi} = \frac{d\phi_{err}}{d\phi_{meas}}\tilde{\phi} \tag{4.5}$$

where ϕ_{err} is the phase error introduced by an I/Q module, as shown in Figure 3-7(c), and ϕ_{meas} is the measured phase. The derivative is used because it is the difference in the phase error over the range of the fluctuation that matters, not the absolute value of the error. The absolute value of the error is just a constant (non-fluctuating) phase offset that does not contribute to high frequency fluctuations. However, changes in the phase error due to fluctuating phase measurements can introduce uncertainty in the measured phase.

Figure 4-2(b) is $\delta\tilde{\phi}$, the phase error introduced by an I/Q module at the phase

fluctuation scale, calculated from the data in Figure 3-7(c). The average magnitude of $\delta\tilde{\phi}$ is 0.008° with a standard deviation of 0.006°. The quoted uncertainty value is the mean plus one standard deviation, 0.014°, which corresponds to a line-integrated density fluctuation uncertainty of $\tilde{n}_e L = \pm 4.1 \times 10^{15}$ m^{-2}.

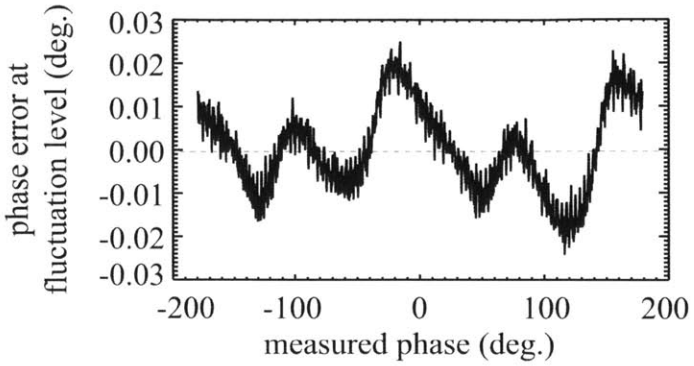

Figure 4-2: The phase uncertainty introduced by an I/Q module at the fluctuation scale, calculated with Equation 4.5 and the data from Figure 3-7(c).

The quoted uncertainty value is conservative for two reasons, and therefore it represents the upper bound on the uncertainty of line-integrated electron density fluctuations. First, the uncertainty analysis assumes that the demodulation electronics are always performing near their most nonlinear operating point, when in reality the electronics usually perform more linearly and thus do not contribute substantially to the uncertainty. Determining exactly where an I/Q module is operating is computationally intensive, so the conservative uncertainty estimate is given in lieu of more demanding analysis. Second, the uncertainty analysis assumes that every measured fluctuation is 10^{17} m^{-2}, but most measured fluctuations are below this level. Since the uncertainty scales with the fluctuation level (Equation 4.5), the calculation is almost always an overestimate.

Uncorrelated noise is also present in the TCI system, but varies from shot to shot depending on the stability of the CO_2 laser and on changes in alignment that occur due to drift of optical components. The TCI digitizers are triggered slightly before plasma breakdown to collect information about uncorrelated noise in the frequency ranges relevant to turbulence measurements. Typically, uncorrelated noise levels are

very close to line-integrated electron density fluctuation levels. When alignment is very poor, the noise can exceed fluctuation-induced signals. Methods to improve diagnostic performance will be discussed in Chapter 7.

4.3 Calculation of Fluctuation Spectra

Before TCI fluctuation measurements can be presented, several common data analysis techniques must be introduced. The power spectral density of a signal (or the "autopower spectrum") is the simplest fluctuation analysis technique, giving a measurement of how much signal power falls at a specific frequency. The autopower spectrum of a time series taken at a single spatial location, $x(R_i, t)$, is simply the normalized Fourier transform of the signal,

$$S(R_i, f) = \left| \frac{1}{\sqrt{T}} \int_{t_1}^{t_2} x(R_i, t) \exp\left(-i2\pi f t\right) dt \right|^2 \tag{4.6}$$

where $T = t_2 - t_1$ is the time interval over which the Fourier transform is computed and R_i indicates that the spectrum is calculated for only the i-th radial chord.[73] When $x(R_i, t)$ is a line-integrated electron density signal, the units of $S(R_i, f)$ are $\mathrm{m}^{-4}/\mathrm{Hz}$, and are typically renormalized to $\mathrm{m}^{-4}/\mathrm{kHz}$. The autopower spectrum can be integrated over a frequency range to determine the amount of fluctuation power in a certain frequency band.

Several factors influence the choice of the time interval, T, over which the Fourier transform is computed. Most importantly, the plasma equilibrium must not be changing significantly over the interval, and 1-10 ms is generally a good choice. Fast Fourier transform (FFT) algorithms require the number of samples in the signal to be a power of 2, so the rate of digitization of the signal must be considered. TCI signals are digitized at 2 MHz, so a Fourier transform period of 1 ms requires 2000 samples. The nearest power of 2 is $2^{11} = 2048$ samples, corresponding to a FFT period of $T = 1.024$ ms. The choice of the period of the Fourier transform affects the frequency resolution of the fluctuation signal. The frequency resolution is $\Delta f = 1/T \approx 1$ kHz for

$T = 1.024$ ms, which is acceptable.

By choosing a period that is short compared to the plasma discharge length, a series of spectra can be computed over different intervals and the results plotted against frequency and time. The result is a color contour plot like the one shown in Figure 4-3, which shows the autopower spectrum, $S(R_i, f)$, of a single TCI chord. The color corresponds to the magnitude of the spectrum, which is directly related to the line-integrated electron density fluctuation level measured by a single TCI chord. The spectrum shows both broadband and coherent features.

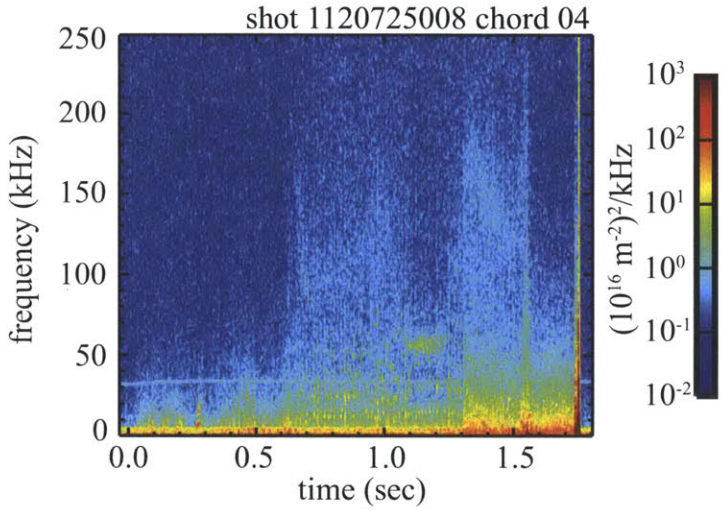

Figure 4-3: Example autopower spectrum, $S(R_4, f)$, from TCI chord 04. The spectrum shows broadband and coherent features at a variety of frequencies.

A single chord does not contain any information about the radial mode structure of the fluctuations. TCI has multiple chords providing line-integrated electron density measurements at different major radii. By spatially Fourier transforming the signals from all the chords, the major-radial wavenumber (k_R) spectrum of the fluctuations can be resolved. The k_R spectrum is calculated by,

$$S(f, k_R) = \left| \frac{1}{\sqrt{T}} \frac{1}{\sqrt{\Delta R}} \int_{R_1}^{R_N} \left[\int_{t_1}^{t_2} x(R,t) \exp\left(-i2\pi f t\right) dt \right] \exp\left(ik_R R\right) dR \right|^2 \qquad (4.7)$$

where R_1 and R_N are the first and last TCI chords, and ΔR is the chord spacing. $S(f, k_R)$ is very useful for determining the properties of turbulence in the plasma. An

example from an H-mode discharge is given in Figure 4-4, showing spatially resolved fluctuations. The spectrum on the left of Figure 4-4 is from phase-contrast imaging, and the spectrum on the right is from TCI. PCI and TCI qualitatively agree.

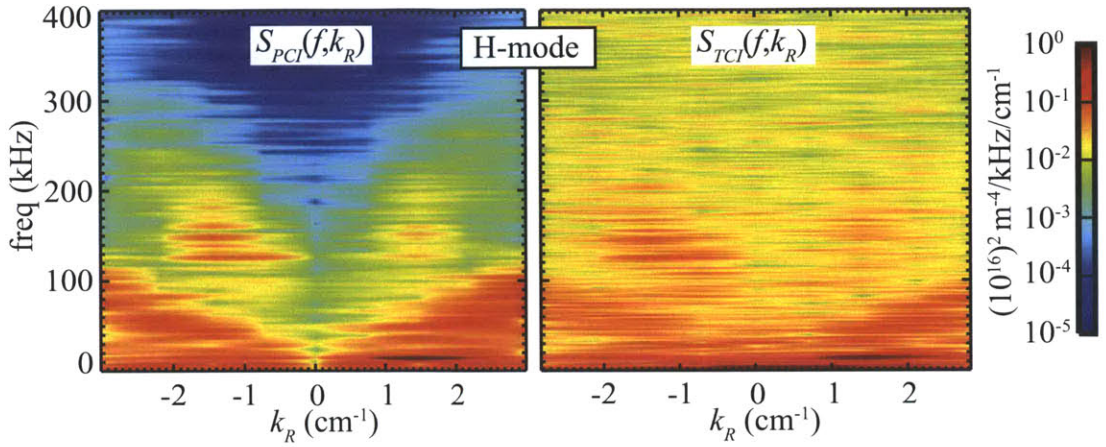

Figure 4-4: Example PCI (left) and TCI (right) $S(f, k_R)$ spectra showing spatially-resolved broadband turbulence.

After presenting TCI fluctuation spectra in comparison with PCI spectra in Figure 4-4, it is immediately clear that the PCI spectra has much lower uncorrelated noise than TCI. Not shown in Figure 4-4 is that the limited TCI k_R range severely reduces its ability to resolve fluctuations in Alcator C-Mod plasmas. The PCI spectrum extends out to $|k_R| \lesssim 12$ cm^{-1}, and broadband fluctuations extend out to these k_R values. High noise levels and limited k_R resolution make quantitative comparisons between TCI and PCI difficult. Quantitative comparisons will require either a very strong fluctuation exceeding the TCI noise, or a reduction of TCI noise levels. Attempts to decrease the noise levels have not been completed (several possible methods are discussed in Chapter 7), but strong fluctuations can be found in certain plasma discharges.

An additional requirement for quantitative comparisons is that the PCI and TCI diagnostics must be carefully filtered so that their wavenumber responses and sensitivities match. Quantitative comparisons, and their implications for phase-contrast imaging, are the topic of Chapter 5.

Chapter 5

Comparison between TCI and PCI

Phase-contrast imaging (PCI) is one of the primary electron density fluctuation diagnostics on Alcator C-Mod, and has been providing high-quality line-integrated electron density fluctuation measurements since the mid-2000s.[52] One of the most important applications of the PCI diagnostic has been quantitative comparisons with plasma simulation codes like GYRO.[12, 53, 54, 55] Such work is part of validation of simulations, and is critically important for fusion energy research.[74] Unless a code can accurately predict turbulence parameters like the fluctuation amplitudes and wavenumber spectra measured in today's experiments, there can be no confidence in the code's predictions for future experiments.

Clearly, quantitative validation studies require highly accurate density fluctuation data, but the absolute calibration of PCI fluctuation measurements is very difficult.[43, 44, 75] Additionally, diagnostics like PCI have limited spatial resolution and a non-linear response to fluctuations at different spatial scales. Thus, PCI does not measure the exact same quantities computed by turbulence simulation codes. To compare PCI to turbulence codes like GYRO, a synthetic diagnostic has been developed to filter the simulated fluctuation data as if it was measured by the experimental PCI diagnostic.[76] The experimental wavenumber response, as determined by PCI calibration, is a critical aspect of the synthetic diagnostic, but is difficult to independently verify.

In sharp contrast to the difficult PCI calibration procedure, the two-color inter-

ferometry (TCI) absolute calibration is well-understood. Thus, there is high confidence in the quantitative fluctuation levels measured by TCI. The regions of plasma sampled by TCI and PCI are shown in Figure 5-1, and the capabilities of each system are highlighted in Table 5.1. PCI samples a broader region of plasma and has many more chords than TCI, which increases its wavenumber range. The PCI resolution in wavenumber space, however, is comparable to that of TCI. The similarity in wavenumber resolution allows fluctuation measurements from TCI and PCI to be quantitatively compared, which can improve the confidence in the PCI absolute calibration and wavenumber response. By appropriately filtering the fluctuation spectra of both diagnostics and comparing the resulting fluctuation amplitudes, the PCI wavenumber response and absolute calibration can be verified.

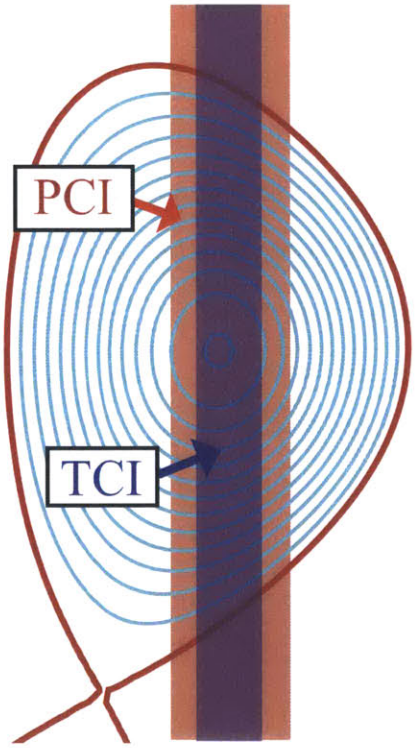

Figure 5-1: Regions of plasma sampled by PCI and TCI.

Diagnostic	Signal	Chords	Dig. rate	Max. k_R	Δk_R
PCI	$\int \tilde{n}_e(z)dz$	32 (31)	5 MHz	11.7 cm^{-1}	0.73 cm^{-1}
TCI	$\int (n_e(z) + \tilde{n}_e(z))dz$	10 (9)	2 MHz	2.83 cm^{-1}	0.71 cm^{-1}

Table 5.1: PCI and TCI capabilities. The PCI specifications are given for the system as configured with a 1.1 mm phase plate groove. PCI and TCI each have one chord that is not operational.

5.1 PCI calibration and wavenumber response

Several important effects reduce the response of the phase-contrast imaging diagnostic to electron density fluctuations of different major-radial wavenumbers. PCI relies on a grooved plate to impart a phase shift to the unscattered portion of the beam, and this phase shift provides the reference signal to the scattered portion of the beam. However, long wavelength (low-k_R) fluctuations produce only a small amount of scattering. The weakly scattered component of the beam can fall within the groove of the phase plate and obtain the same phase shift as the reference signal. As a result, all information about low-k_R fluctuations is lost.

The low-k_R wavenumber response of phase-contrast imaging systems has been calculated analytically by Coda.[43] The low-k_R calculation takes into account Gaussian beam profiles and diffraction from an aperture stop, as well as the effect of the phase plate. The low-k_R response is calculated to be,

$$R_{low-k_R}(k_R) \propto \int_{-a}^{+a} \frac{\sin(k_c x)}{\pi x} e^{-x^2/\omega_0^2} [1 - \cos k_R x]\, dx \tag{5.1}$$

where a is the radius of the aperture stop, ω_0 is the Gaussian beam waist, k_c is a critical wavenumber below which the response is cut off, and x is the radial coordinate of the aperture stop. A reasonable approximation to this formula is provided by Rost (with $\alpha = 2$),[76]

$$R_{low-k_R}(k_R) = 1 - \exp[-(k_R/k_{R,min})^{\alpha}]. \tag{5.2}$$

The contributions to the PCI response from the phase plate, diffraction effects, and Gaussian beam profile effects are now parameterized by two quantities: $k_{R,min}$, which

represents the minimum detectable wavenumber of the PCI system, and α, which characterizes how rapidly the response drops off near the minimum wavenumber. The exponent, α, has been generalized from the value provided in Ref. [76] so that the experimentally measured low-k_R response can be matched. When PCI is configured with the 1.1 mm groove phase plate, as it is for the data used in this thesis, $k_{R,min} \approx 1.7$ cm^{-1} and $\alpha = 10$.

PCI also has a high-k_R wavenumber response which is a result of finite sample volume effects.[77] Figure 5-2 illustrates the effect of detecting a fluctuation with a finite sample volume. The narrow volume, V_1, sees a very small component of the fluctuation, so the signal measured by a power-sensitive detector will be resolved as the fluctuation oscillates. However, the larger volume, V_2, will not detect the fluctuation at all because the positive and negative components will cancel on the detector face. Intermediate-size sample volumes will have varying amounts of resolution, and the result is a wavelength (and hence wavenumber) dependent diagnostic response.

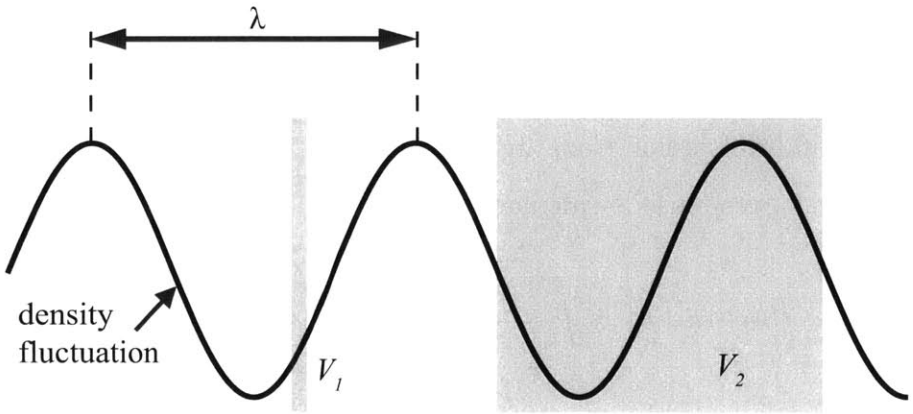

Figure 5-2: Finite sample volume effect. Figure adapted from Fig. 1 in Ref. [77].

The PCI wavenumber response due to finite sample volume effects has also been calculated analytically by Coda.[43]. The calculation assumes that the signal from a detector centered at x is the surface average of the power flux incident on a circle of

radius r through the plasma,

$$\begin{aligned} R_{fsv}(k_R) &= \frac{1}{\pi r^2}\int_{-r}^{+r} 2\sqrt{r^2-x^2}e^{-ik_R x}dx \\ \Rightarrow R^B_{fsv}(k_R) &= \frac{2J_1(k_R r)}{k_R r} \end{aligned} \tag{5.3}$$

where J_1 is a first-order Bessel function.[43] A simpler model assumes a Gaussian wavenumber response with an e-folding length equal to half the width of a single detector element,[77]

$$R^G_{fsv}(k_R) = \exp\left(-\left(k_R d_R\right)^2/2\right) \tag{5.4}$$

where $d_R = 0.75$ mm is the detector width.

The Bessel function response model (Equation 5.3) takes the surface average of the power flux over the detector area through the plasma, and will therefore depend on the imaging characteristics of the PCI system. The PCI system on Alcator C-Mod has a major-radial array of 32 rectangular mercury-cadmium-telluride (HgCdTe) detectors. Each element is 0.75 mm in the major-radial dimension and 1.0 mm in the other dimension, and is separated from adjacent elements by 1.0 mm. Each detector element gets magnified and imaged onto the plasma mid-plane.[44, 75] The magnification is calculated from the ratio of the chord spacing through the plasma to the detector spacing (1.0 mm). The chord spacing through the plasma is determined from a pre-plasma calibration,[44] and is 2.709 mm. The magnification of the PCI system is thus $M = 2.709$. The circular radius, r, over which the average is calculated in the Bessel function model is taken to be half the major-radial width of the detector image in the plasma. After magnification, $r = M \times d_R/2 = 1.02$ mm.

The PCI wavenumber response can now be written explicitly by multiplying the low-k_R and high-k_R response models together. The Gaussian model ($R_{PCI,G}$) is calculated by multiplying Equations 5.2 and 5.4, and the Bessel function model ($R_{PCI,B}$)

is calculated by multiplying Equations 5.2 and 5.3,

$$R_{PCI,G} = \left(1 - \exp\left[-\left(\frac{k_R}{1.7\ \text{cm}^{-1}}\right)^{10}\right]\right) \exp\left[-\frac{(k_R \times 0.075\ \text{cm})^2}{2}\right] \quad (5.5)$$

$$R_{PCI,B} = \left(1 - \exp\left[-\left(\frac{k_R}{1.7\ \text{cm}^{-1}}\right)^{10}\right]\right) \frac{2J_1\,(0.102\ \text{cm} \times k_R)}{0.102\ \text{cm} \times k_R}. \quad (5.6)$$

Equations 5.5 and 5.6 are plotted in Figure 5-3; these are the theoretical PCI response curves based on Bessel function and Gaussian models.

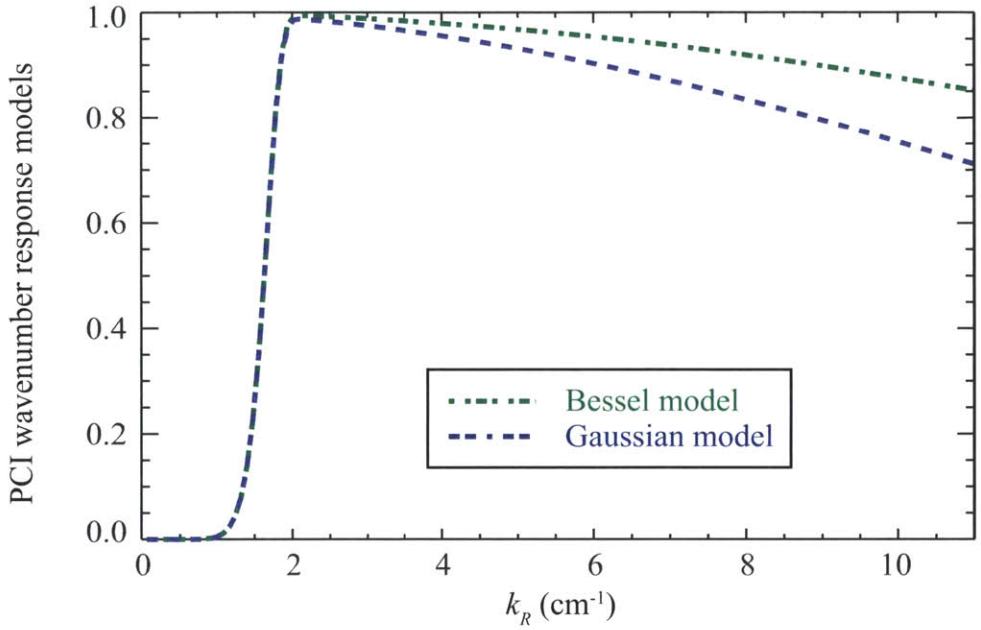

Figure 5-3: Theoretical PCI response curves for Gaussian and Bessel function models.

There are significant differences, particularly at high-k_R, between the Gaussian and Bessel function models. The true wavenumber response model must be determined by calibrating the PCI system. To do this, the absolute PCI response to fluctuations must also be measured.

The absolute PCI calibration is measured by sending a sound wave with a known k_R and pressure into gas and measuring the response with the PCI system.[44] The result for a given k_R value is shown in Figure 5-4. The horizontal axis is the PCI channel number. The vertical axes are the measured pressure wave amplitude (in mV,

left) and the reference pressure wave amplitude (in 10^{16} m^{-2}, right). The blue crosses correspond to the measured amplitude from a given PCI chord, and the red line is the pressure wave amplitude. The relationship between the two vertical axes defines the absolute calibration. For the case shown in Figure 5-4, 1 mV of measured amplitude corresponds to 0.150×10^{16} m^{-2} of fluctuation amplitude at $k_R = 2.73$ cm^{-1}.

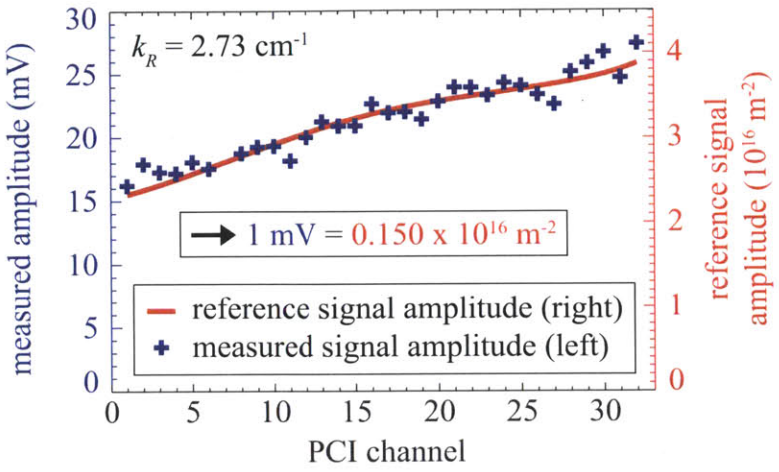

Figure 5-4: PCI absolute calibration for a single k_R value. The blue crosses are the measured amplitude of the sound wave (left axis), and the red line is the true sound wave amplitude (right axis). The relationship between the axes defines the absolute calibration, which in this case is 1 mV $= 0.150 \times 10^{16}$ m^{-2}. Figure adapted from Fig. 11(b) in Ref. [78].

The PCI wavenumber response has been determined by scanning the frequency of the sound wave (and thus its wavenumber). An example is shown in Figure 5-5. Figure 5-5(a) shows the sound wave amplitude (right axis) and the measured amplitude (left axis) as a function of the wavenumber of the sound wave. The wavenumber response is calculated by normalizing the measured data to the sound wave amplitude. This is done for a different experiment with a slightly different absolute calibration in Figure 5-5(b). The curve is a Bessel function model adjusted to fit the normalized data.

The curve in Figure 5-5(b), the data-matched Bessel function model, can be further normalized to the absolute calibration value. The result is the quoted PCI wavenumber response function, which is symmetric about $k_R = 0$. The quoted wavenumber response function for the PCI configuration used in this thesis is pro-

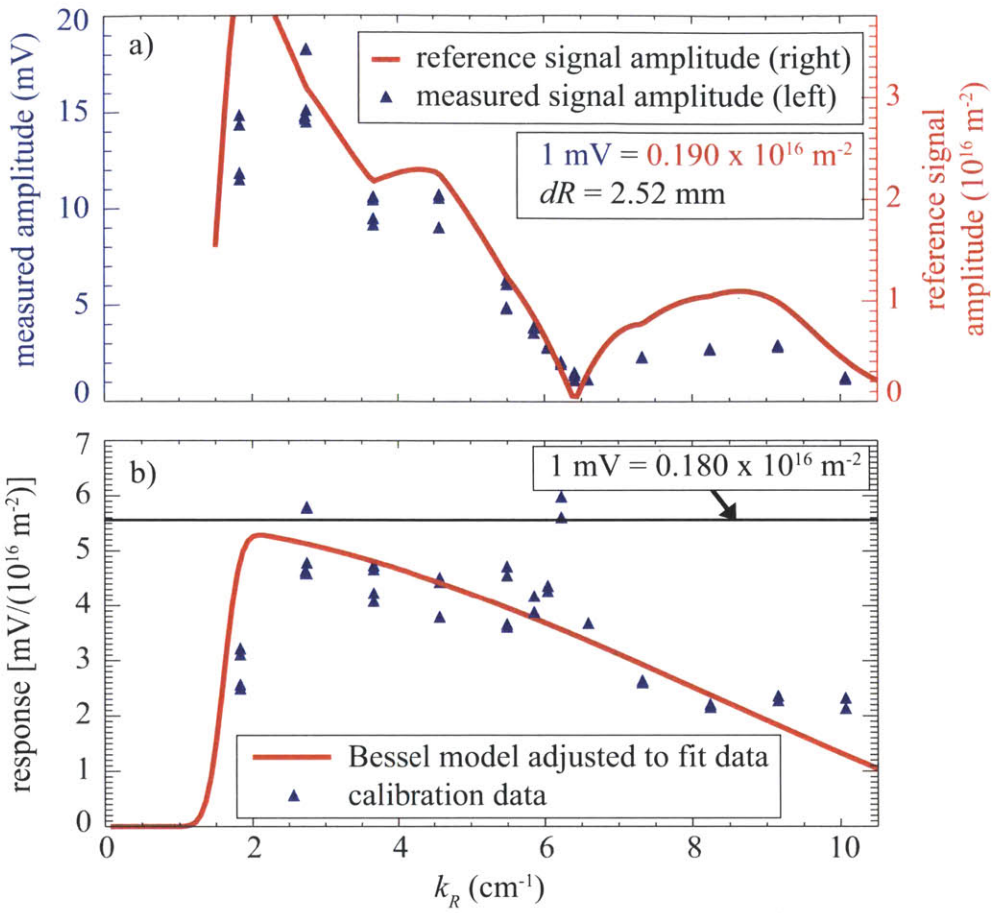

Figure 5-5: Example of a PCI wavenumber response calibration. (a) Measured data for multiple k_R values, taken by varying the frequency of the sound wave. The blue diamonds are the measured amplitude of the sound wave (left axis), and the red line is the true sound wave amplitude (right axis). (b) The ratio of the blue triangles to the red line from (a). The absolute calibration value is a straight line. The red line is fit to the calibration data using a Bessel function model. Figure adapted from Fig. 12 in Ref. [78].

vided as an IDL array of data points.[79] (The full data set is given in Table C.1 in Appendix C.) The data-matched Bessel function wavenumber response is plotted with the Gaussian and Bessel function models (Equations 5.5 and 5.6) in Figure 5-6. There is a large discrepancy between the theoretical models and the data-matched Bessel function model.

To match the theoretical curves with the data-matched model, the parameters of the theory must be adjusted. It is hypothesized that the effective size of a single

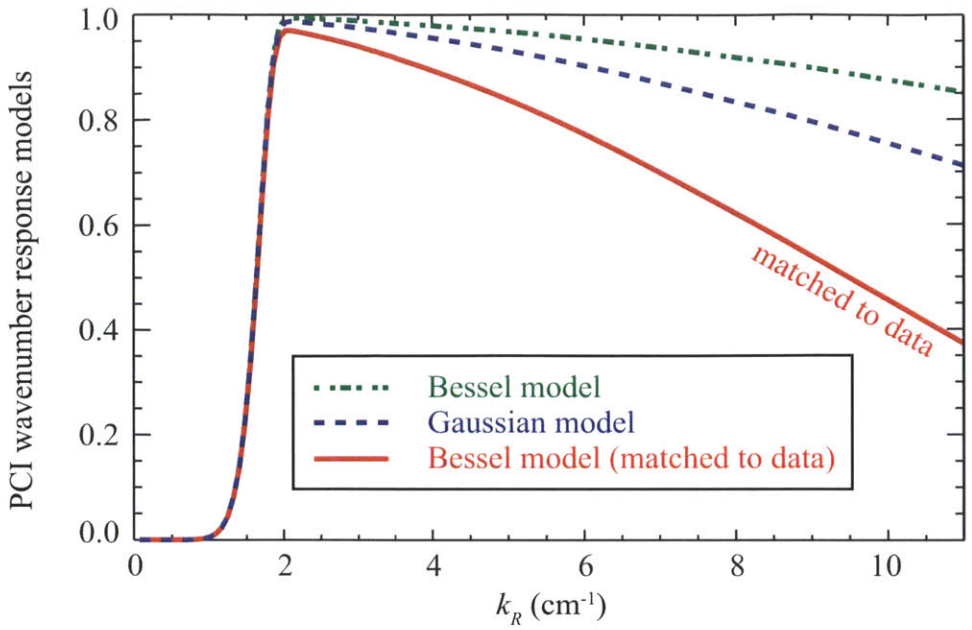

Figure 5-6: Theoretical and data-matched PCI response curves. The data-matched (solid red) curve is plotted from data given in Appendix C.

detector element is larger than the true size.[78] This is a reasonable hypothesis, because the Gaussian model arbitrarily used a value for the e-folding length equal to half the detector width, which is not necessarily true. For the Bessel function model, the effective detector size through the plasma was modeled to be circular, when in reality the detector is rectangular. The following adjustments bring the theoretical curves into agreement with the data-matched Bessel function model,

$$\begin{aligned} R_{PCI,G} &: d_R \rightarrow 1.59 d_R \\ R_{PCI,B} &: r \rightarrow 2.3r. \end{aligned} \tag{5.7}$$

The results are plotted in Figure 5-7. The most-accurate model, the Bessel function model, is given explicitly by,

$$R_{PCI}(k_R) = \left(1 - \exp\left[-\left(\frac{k_R}{1.7 \text{ cm}^{-1}}\right)^{10}\right]\right) \frac{2J_1\left(0.235 \text{ cm} \times k_R\right)}{0.235 \text{ cm} \times k_R}. \tag{5.8}$$

The data-matched curve, which to a great approximation is Equation 5.8, is the curve

used in PCI synthetic diagnostics, and will be applied to the TCI data for verification.

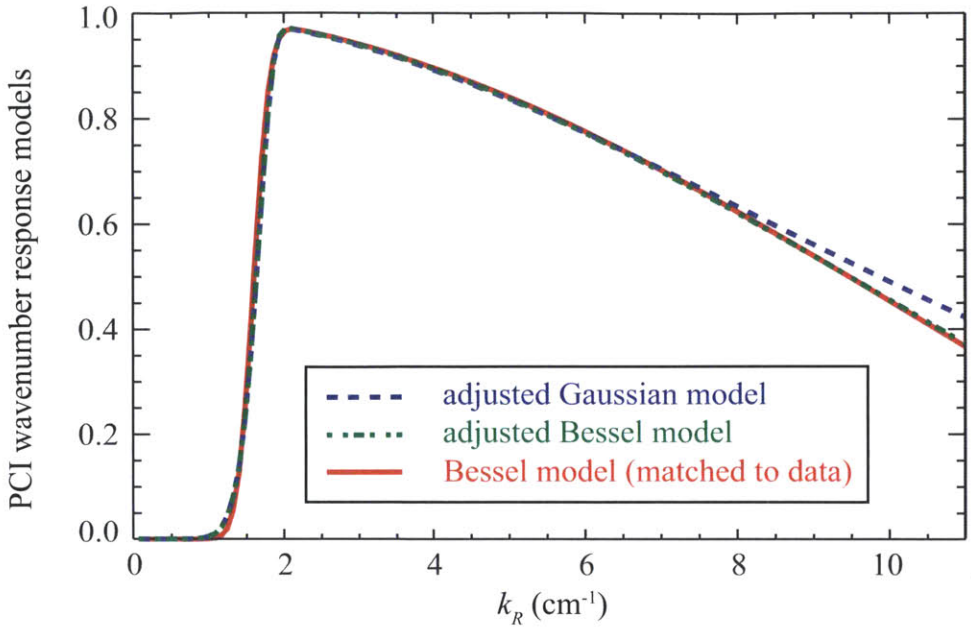

Figure 5-7: Adjusted theoretical and experimental PCI response curves. The data-matched (solid red) curve is plotted from data given in Appendix C.

One possibly significant observation to note here is that the Bessel function model shown in Figure 5-7 is slightly below the Gaussian model at high-k_R. Examining Figure 5-5(b), it appears that the calibration data is consistently above the data-matched (Bessel function) curve in the high-k_R region, which may indicate that a Gaussian model more accurately describes the PCI wavenumber response. Unfortunately, TCI is not sensitive to fluctuations at such high k_R, so no conclusions can be drawn about which model is preferable between the Gaussian and Bessel function models.

5.2 TCI calibration and wavenumber response

In contrast to the difficult PCI absolute calibration, the TCI calibration is much simpler because there is no low-k_R cutoff in the wavenumber response. Instead, TCI is completely sensitive to infinite wavelength fluctuations, so the wavenumber response is unity at $k_R = 0$. The absolute calibration is given by Equation 2.33. There will still be finite sample volume effects which attenuate fluctuations with shorter wavelengths.

The same two models used for the PCI high-k_R wavenumber response are applied to TCI, but no low-k_R response is needed. The Bessel function model requires knowledge of the TCI optics magnification and the detector size. The magnification was found in Chapter 4 to be $M = 2.5$, and the detector width is $d_R = 2.0$ mm. The Bessel function model is,

$$R_{TCI,B}(k_R) = \frac{2J_1(k_R r)}{k_R r} \tag{5.9}$$

with $r = M \times d_R/2 = 0.25$ cm. The Gaussian model is,

$$R_{TCI,G}(k_R) = \exp\left(-\left(k_R d_R\right)^2/2\right) \tag{5.10}$$

with $d_R = 0.2$ cm. One additional model, a flat wavenumber response, provides an upper bound for the TCI response,

$$R_{TCI,F}(k_R) = \begin{cases} 0, & |k_R| > k_{R,max} \\ 1, & |k_R| \leq k_{R,max} \end{cases} \tag{5.11}$$

where $k_{R,max} \approx 3.0$ cm^{-1}. The three TCI wavenumber response models are plotted in Figure 5-8. These models will be applied to PCI fluctuation spectra for quantitative verification of the PCI calibration.

Before proceeding with the quantitative comparison between PCI and TCI fluctuation measurements, it should be noted that the TCI wavenumber response has not been calibrated. However, fluctuations with wavenumbers near $k_{R,max}$ are routinely observed, with little or no apparent drop in intensity. This suggests that the high wavenumber cutoff is at least comparable to the predictions given by Equations 5.9 and 5.10.

5.3 Diagnostic Filtering

Fluctuation measurements made with PCI and TCI are quantitatively compared for the quasi-coherent mode (QCM) and for broadband fluctuations. To do this,

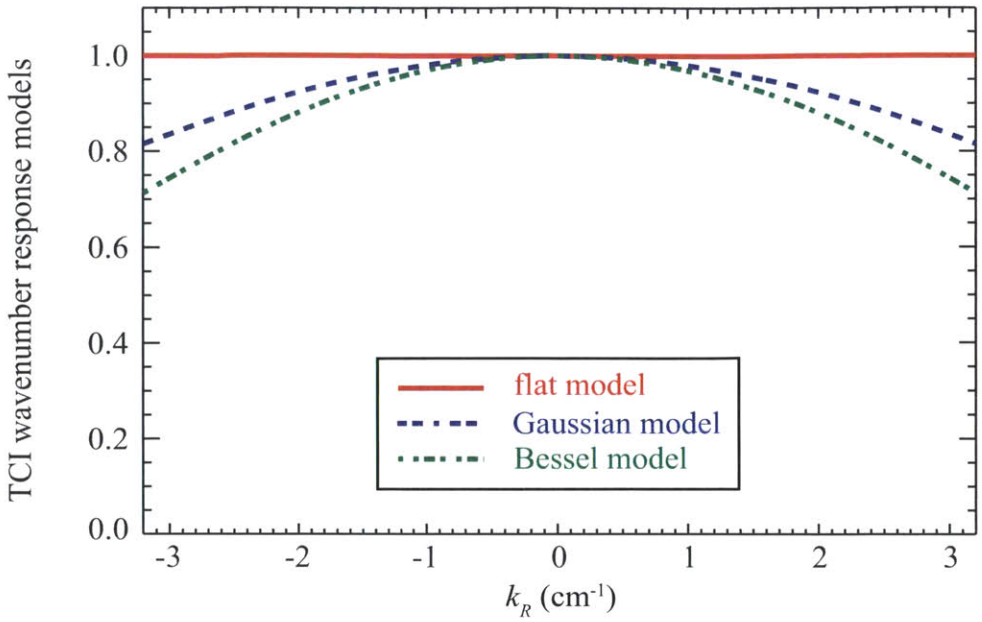

Figure 5-8: TCI wavenumber response models.

first the spectra must be computed with Equation 4.7. The PCI spectra, S_{PCI}, is calculated from data stored in the Alcator C-Mod data tree that already has the absolute calibration factor applied. PCI resolves fluctuations with wavenumbers from $-12\ \text{cm}^{-1} \lesssim k_R \lesssim 12\ \text{cm}^{-1}$, but the TCI spectra, S_{TCI}, is limited to $-3.2\ \text{cm}^{-1} \lesssim k_R \lesssim 3.2\ \text{cm}^{-1}$. However, both diagnostics have nearly the same wavenumber resolution, with $\Delta k_R \approx 0.72\ \text{cm}^{-1}$ (Table 5.1). The similarity in resolution allows a simple interpolation over wavenumbers, which truncates the PCI spectra to the TCI wavenumber range. The result of this process for the QCM discharge is shown in Figure 5-9, and for broadband fluctuations in Figure 5-10.

The next step is to apply the PCI response function to the TCI data. To do this, the $S_{TCI}(f, k_R)$ array is multiplied by the PCI data-matched Bessel function model, given approximately by Equation 5.8. The TCI response models are also applied to the PCI spectra. This must be done separately for each TCI model, by multiplying $S_{PCI}(f, k_R)$ by Equations 5.9, 5.10, and 5.11. The result of this process is shown for the TCI spectra in Figure 5-11. Due to the fairly flat wavenumber response for all TCI response models, the effect of filtering the PCI spectra with the TCI models is

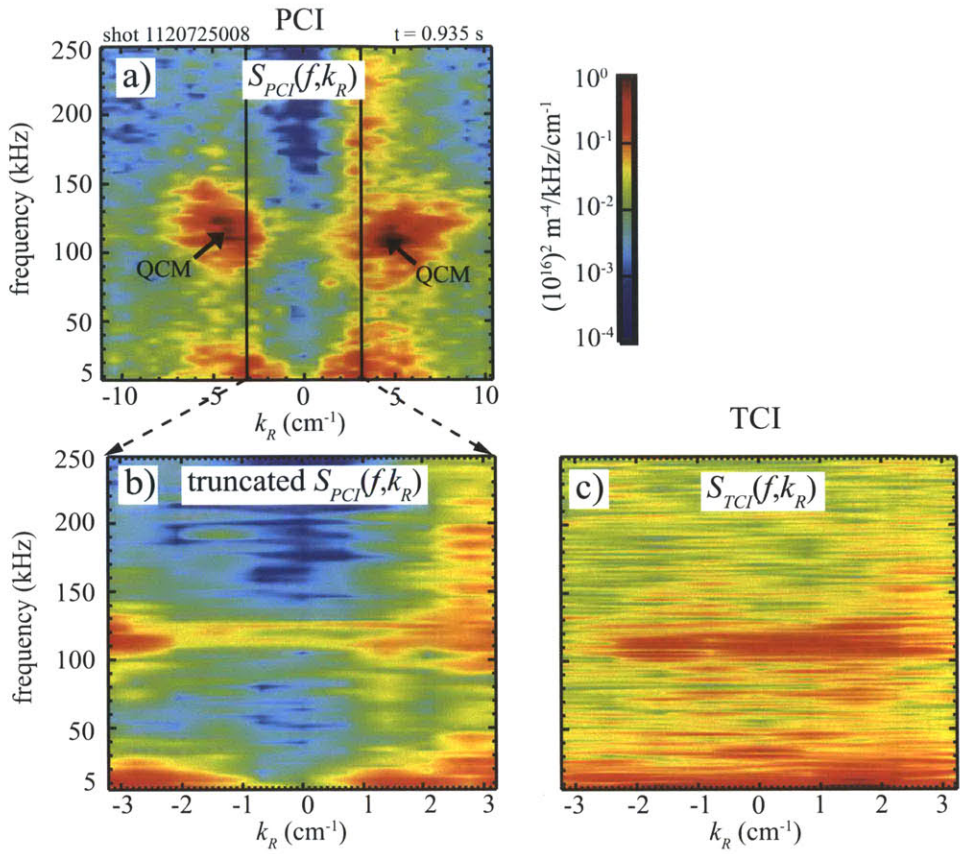

Figure 5-9: (a) PCI $S(f, k_R)$ spectra with TCI wavenumber range overlaid. (b) PCI spectra interpolated onto TCI wavenumber range. (c) TCI spectra.

not visually obvious; the resulting PCI spectra need to be integrated to see the effects of the TCI models.

Now that the PCI and TCI spectra have been filtered to replicate the response properties of each other, they can be quantitatively compared. To do this, the spectra are integrated over appropriate frequency ranges (f_1, f_2), and over the entire remaining wavenumber range $(-k_{R,max}, k_{R,max})$. $k_{R,max}$ is about 3.2 cm^{-1} for the QCM discharge and about 2.9 cm^{-1} for the broadband fluctuations, due to slight differences in the TCI chord spacing on the two different run days. Explicitly, the line-integrated

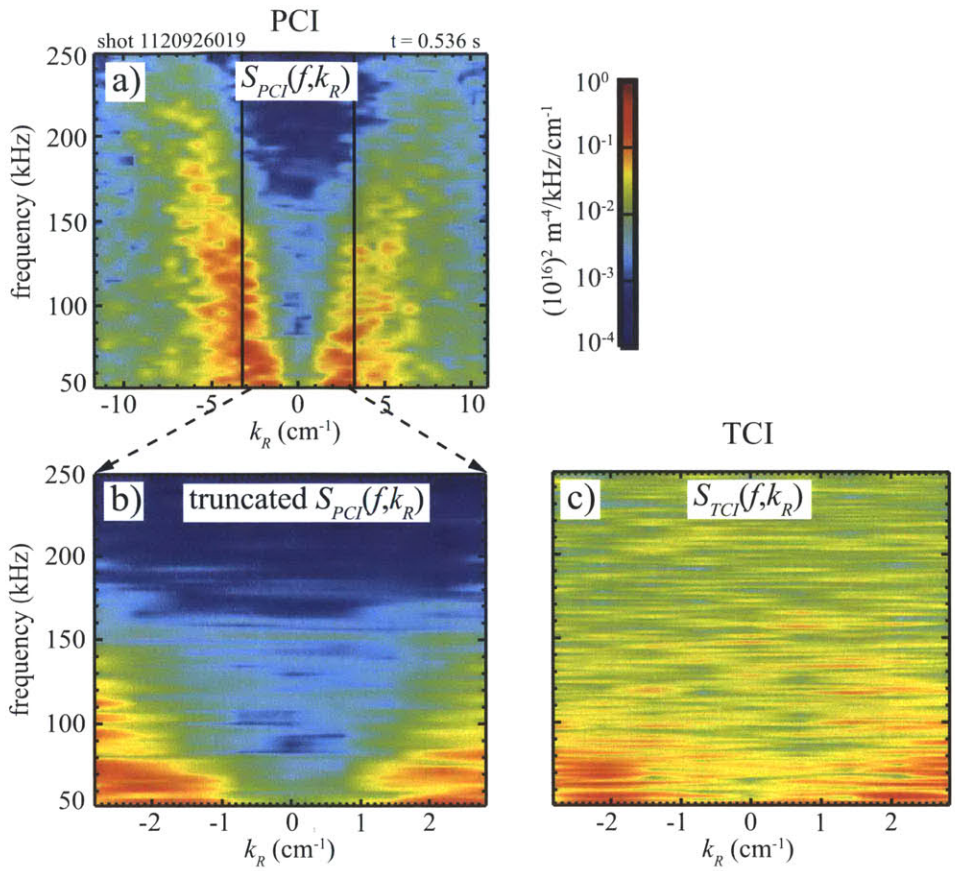

Figure 5-10: (a) PCI $S(f, k_R)$ spectra with TCI wavenumber range overlaid. (b) PCI spectra interpolated onto TCI wavenumber range. (c) TCI spectra.

electron density fluctuation amplitudes are calculated with,

$$(\tilde{n}_e L)^2_{PCI} = \int_{f_1}^{f_2} \int_{-k_{R,max}}^{k_{R,max}} S_{PCI}(f, k_R) R_{TCI}(k_R) dk_R df \tag{5.12}$$

$$(\tilde{n}_e L)^2_{TCI} = \int_{f_1}^{f_2} \int_{-k_{R,max}}^{k_{R,max}} S_{TCI}(f, k_R) R_{PCI}(k_R) dk_R df \tag{5.13}$$

where R_{TCI} and R_{PCI} indicate that the spectra, S_{PCI} and S_{TCI}, have been filtered.

The result of applying Equations 5.12 and 5.13 to the filtered broadband spectra are shown in Figure 5-12. The spectra are integrated from $f_1 = 50$ kHz to $f_2 = 150$ kHz. This is the range of frequencies where the broadband fluctuations greatly exceed the TCI noise levels for the majority of the discharge. PCI data is only available after $t = 0.4$ s and the plasma disrupts at $t = 0.9$ s. The black dashed line is the TCI

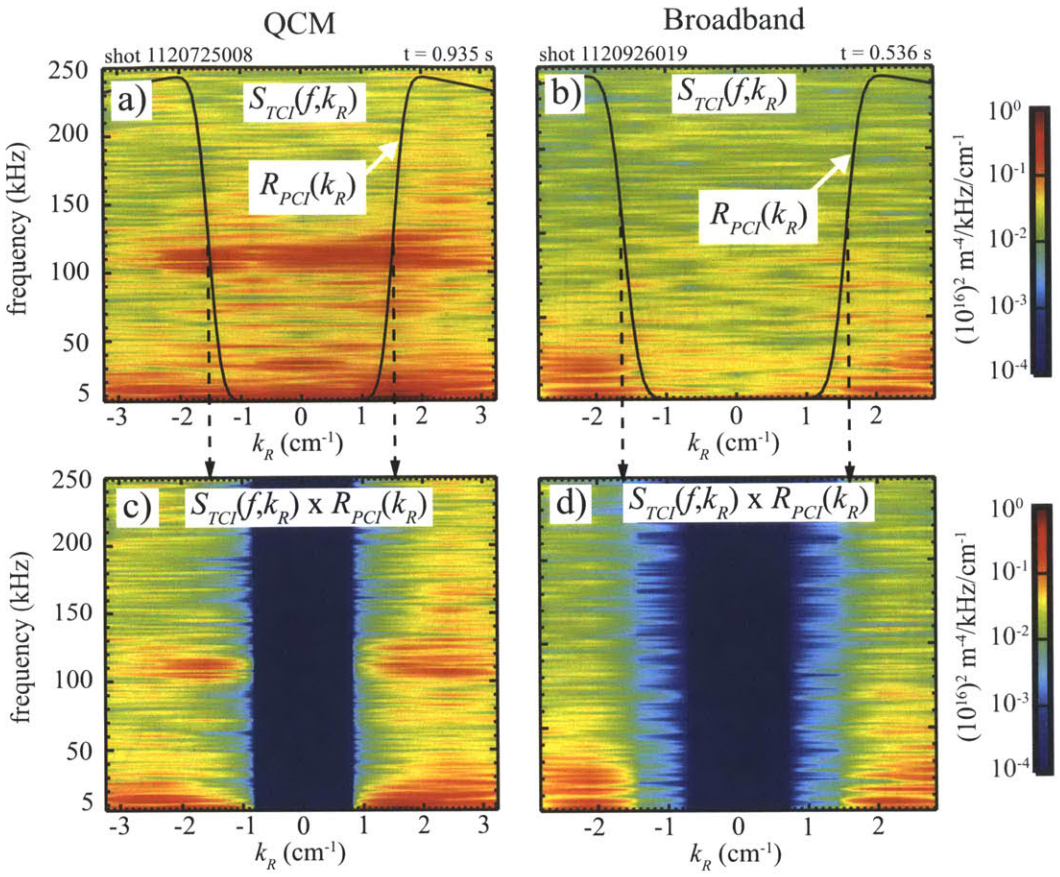

Figure 5-11: (a-b) TCI $S(f, k_R)$ spectra with PCI wavenumber range overlaid for (a) QCM and (b) broadband fluctuations. (c-d) TCI spectra after multiplication by R_{PCI} for (c) QCM and (d) broadband fluctuations.

fluctuation level, and the red, blue, and green solid lines are the PCI fluctuation levels using the flat, Gaussian, and Bessel TCI response models, respectively. The PCI fluctuation levels agree very well with the TCI fluctuation levels, especially for the Gaussian and Bessel function models. There is some disagreement in the brief H-mode period from 0.71 s $\leq t \leq$ 0.79 s, possibly due to changes in alignment which will affect the wavenumber responses of both diagnostics. There is also disagreement following the H-mode period when the fluctuations begin to approach the TCI noise floor. The TCI noise floor is calculated by integrating fluctuations measured prior to plasma breakdown, using Equation 5.13 with no PCI wavenumber response applied to the TCI spectra (i.e. $R_{PCI} = 1$). Since PCI is a dedicated fluctuation diagnostic

with over ten years of optimization, its noise floor is very small and is not included in the figure.

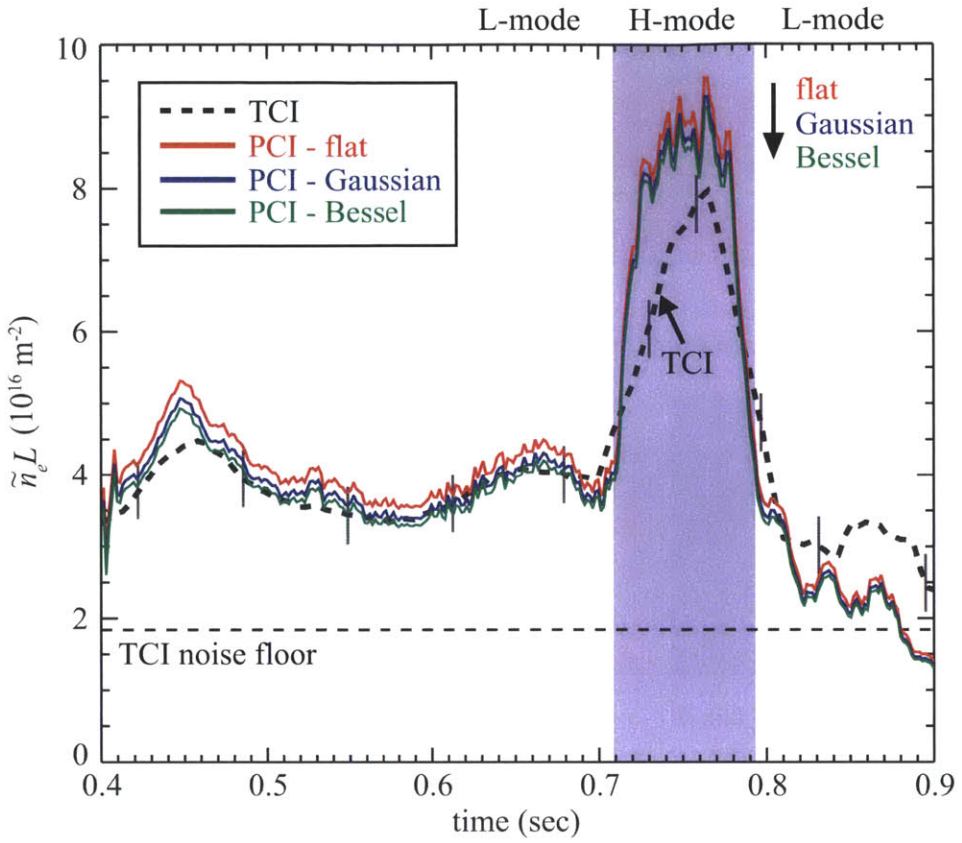

Figure 5-12: Filtered PCI and TCI spectra integrated over broadband turbulence (50-150 kHz). The black dashed line is the TCI fluctuation level, and the red, blue, and green solid lines are the PCI fluctuation levels with the flat, Gaussian, and Bessel TCI wavenumber responses. The PCI noise floor is very small and is not included.

For the quasi-coherent mode fluctuation amplitude, a simple constant frequency range of integration cannot be applied to Equations 5.12 and 5.13 because the frequency of the QCM changes over the course of the discharge. The QCM mode is shown in a single-chord PCI autopower spectrum in Figure 5-13. The black lines denote the ranges used for the frequency integration.

The result of applying Equations 5.12 and 5.13 to the QCM spectra are shown in Figure 5-14. The spectra are integrated over the frequency ranges shown in Figure 5-13, where the QCM is strongest. The black dashed line is the TCI fluctuation level, and the red, blue, and green solid lines are the PCI fluctuation levels using the

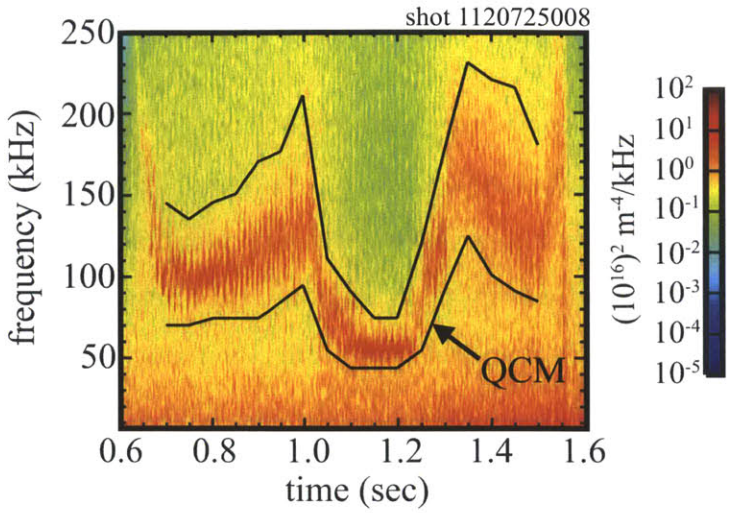

Figure 5-13: Single-chord PCI autopower spectrum showing the QCM used for quantitative comparisons to TCI. The black lines denote the ranges used for the frequency integration.

flat, Gaussian, and Bessel TCI response models, respectively. As with the broadband fluctuations, the PCI fluctuation levels agree very well with the TCI fluctuation levels, especially for the Gaussian and Bessel function models.

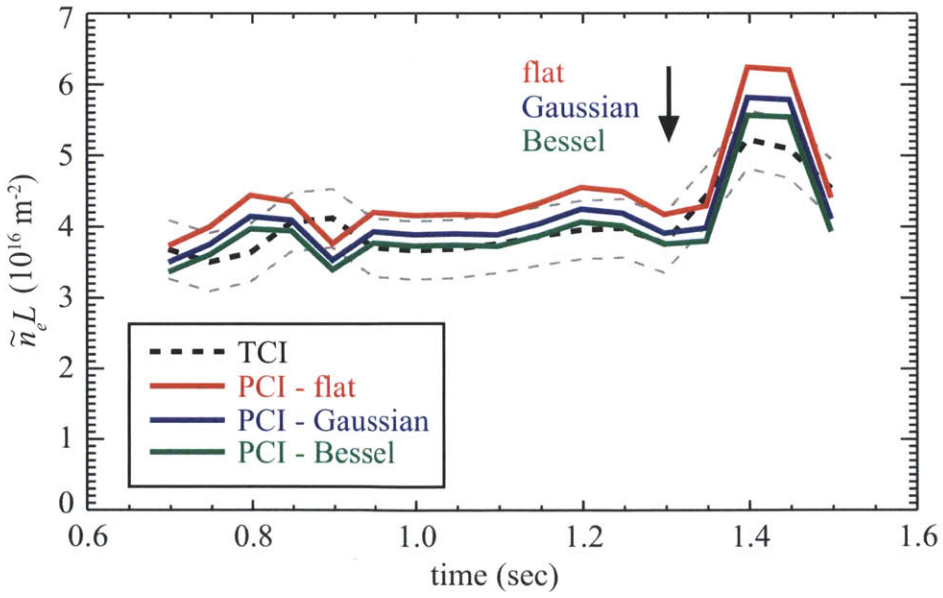

Figure 5-14: Filtered PCI and TCI spectra integrated over the QCM frequency range. The PCI noise floor is very small and is not included.

5.4 Discussion

The results of the previous section provide promising conclusions about the accuracy of the PCI calibration and wavenumber response. The need for an empirical adjustment to the PCI wavenumber response theory, combined with the relative imprecision of the absolute and wavenumber response calibration procedures, has been very unsettling for the transport model validation community. Now, by applying the PCI wavenumber response to an independent measurement of the same quantity with TCI, the PCI absolute calibration and wavenumber response model has been partially validated.

The quantitative comparison results also provide confidence in the TCI wavenumber response models. The quantitative agreement was found to be mostly independent of the choice of the TCI wavenumber response model. Reasonable Gaussian and Bessel function models, when applied to the PCI fluctuation spectra, were still shown to agree with the measured TCI fluctuation levels. The flat wavenumber response model, when applied to the PCI spectra, returned fluctuations that were only slightly higher than the measured TCI fluctuation amplitudes. This suggests that the TCI wavenumber response is nearly flat, and is well-described by both the Gaussian and Bessel function models. The Bessel function model appears to return the best results.

Unfortunately, the quantitative comparison performed in this Chapter is limited to only the low-k_R region of the PCI wavenumber response. Since the Gaussian and Bessel function models are nearly identical at low k_R (see Figure 5-7), the results of the comparison to TCI cannot determine whether one model is preferable over the other. The form of the PCI high-k_R response region remains unverified.

In summary, this analysis has verified two aspects of the PCI calibration: the absolute calibration, and the shape of the low-k_R region of the wavenumber response for $|k_R| \lesssim 3$ cm^{-1}. The remainder of the PCI wavenumber response function remains unverified, as shown in Figure 5-15.

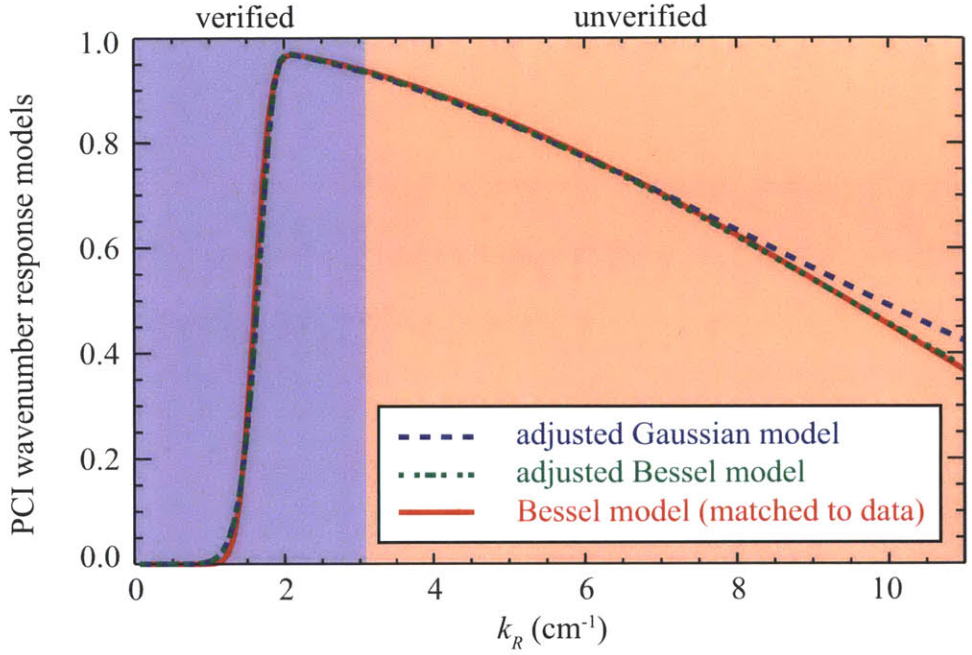

Figure 5-15: Verified and unverified regions of PCI wavenumber response models. The absolute calibration has also been verified. The data-matched (solid red) curve is plotted from data given in Appendix C.

Chapter 6

Measurements in MC/MH Experiments

Previous experiments on Alcator C-Mod exhibited an increase in the plasma rotation with the application of 50 MHz ion cyclotron radio frequency (ICRF) power in L-mode plasmas; the increased rotation was found to be due to mode-conversion flow drive.[67] However, when the plasma transitioned from L- to I-mode, the plasma rotation did not increase further, even though the intrinsic rotation of I-mode plasmas should have added to the rotation.[80] Large neoclassical tearing modes (NTMs) were observed during the I-mode phase of the discharges, so it was hypothesized that the appearance of NTMs somehow limits the maximum rotation that can be achieved in I-mode plasmas. To test this hypothesis, additional high-performance I-mode experiments were conducted at Alcator C-Mod to try and characterize mode-conversion/minority-heating (MC/MH) plasmas by searching for NTMs.[67]

During the experiments, the phase-contrast imaging and two color interferometry diagnostics each detected a quasi-periodic series of fluctuations that do not have the expected behavior of an NTM. The series of modes appear to correlate with changes in the electron temperature profile during the sawtooth cycle. This chapter describes the experiment and the measurements made by PCI and TCI, and characterizes the observed fluctuations.

6.1 Experiment and Measurements

The discharge of interest is Alcator C-Mod shot 1120927023. The discharge has a toroidal magnetic field of $B_T = 5.1$ T and plasma current of $I_p = 1.0$ MA, with about 4.25 MW of coupled ICRF power. The plasma contained approximately a 10% He-3 minority fraction and a 4% H fraction. About 1.25 MW of the ICRF power was at 50 MHz in an attempt to drive mode-conversion plasma flows. The remaining 3 MW of ICRF power was at 80 MHz and was necessary to access the high-performance I-mode regime. Unfortunately, the experiment found that the available ICRF power at 50 MHz was insufficient to drive any significant plasma flows; the observed changes in rotation are the result of increased intrinsic (not driven) rotation due to increased stored energy.[80] Off-axis minority ion heating was still strong enough to drive large sawtooth events, which greatly alter the core electron temperature profile on a $20-30$ ms timescale. Time traces of the plasma line-integrated electron density, on-axis electron temperature, average toroidal rotation, and applied ICRF power are given in Figure 6-1.

In the I-mode phase of the discharge when the ICRF power is on ($t = 0.85 - 1.2$ s), a series of modes are periodically observed in PCI and TCI fluctuation spectra. The modes seem to be correlated to the sawtooth cycle, only appearing in the quasi-steady phase between crashes. There are three distinct types of sawtooth events in the I-mode phase, which can be seen clearly in the on-axis electron temperature trace given in Figure 6-2. The three types of sawtooth events are categorized based on the time they occur: early in the RF phase, in the middle of the RF phase, and in the late RF phase of the discharge. The electron density fluctuations are observed in the PCI and TCI spectra in each quasi-steady period between crashes, as shown in the shaded regions in Figure 6-2. An example of the fluctuation measurements from each of the three different types of sawtooth events are now given.

The first type of sawtooth appears early in the I-mode/RF phase of the discharge from $t = 0.942 - 1.010$ s. An example is shown in Figure 6-3. There is a very brief flattening in the on-axis electron temperature, $T_e(0)$, when the modes appear.

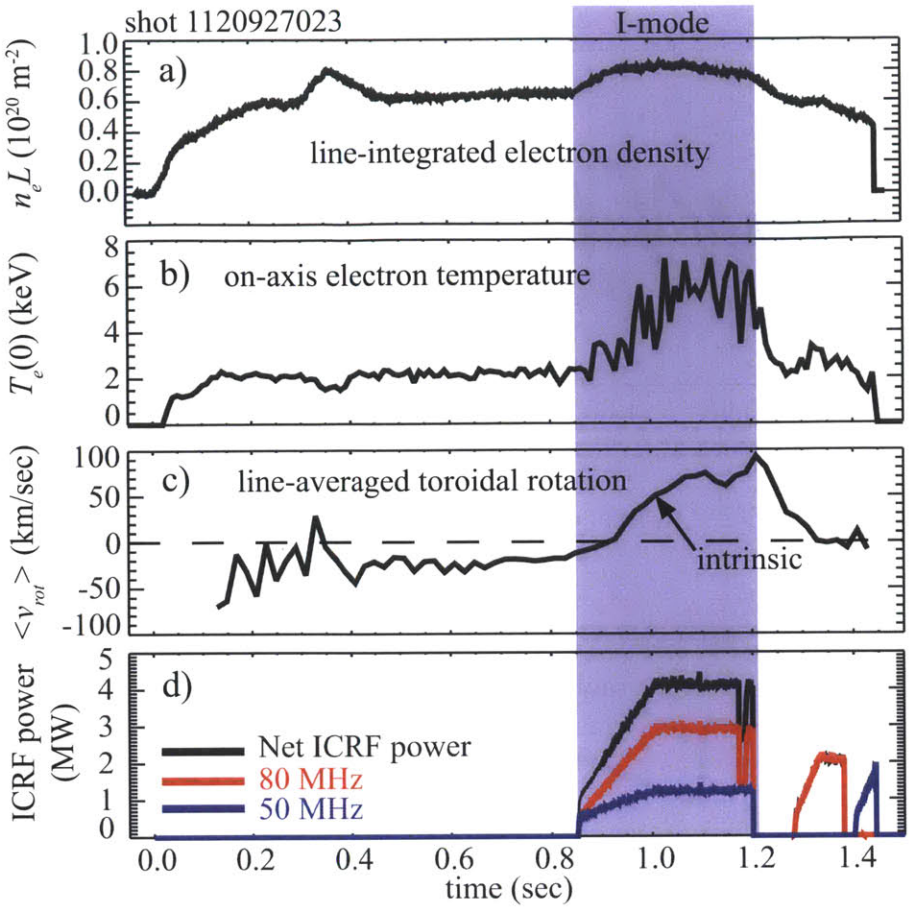

Figure 6-1: Plasma parameters. (a) Line-integrated electron density measured by TCI. (b) On-axis electron temperature measured by Thomson scattering. (c) Line-averaged plasma rotation measured by impurity spectroscopy. (d) Applied ICRF power.

An example of the second type of sawtooth is shown in Figure 6-4. This sawtooth occurs when the plasma has fully accessed I-mode in the middle of the RF phase from $t = 1.010 - 1.180$ s. Following a crash, the on-axis temperature grows and then steadies for almost 10 ms. During the period of steady on-axis temperature, the modes appear in the PCI and TCI spectra. Following the steady period, there is a small crash, a gradual temperature rise, and then another large crash. (The small crash may be partial magnetic reconnection,[81] but this has not been further investigated.)

Notice that the observed modes during the steady period between crashes are

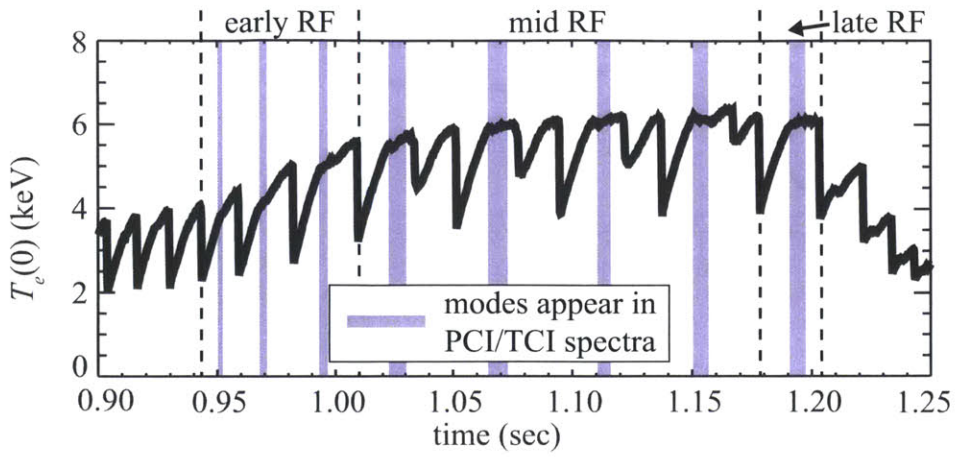

Figure 6-2: On-axis electron temperature during I-mode.

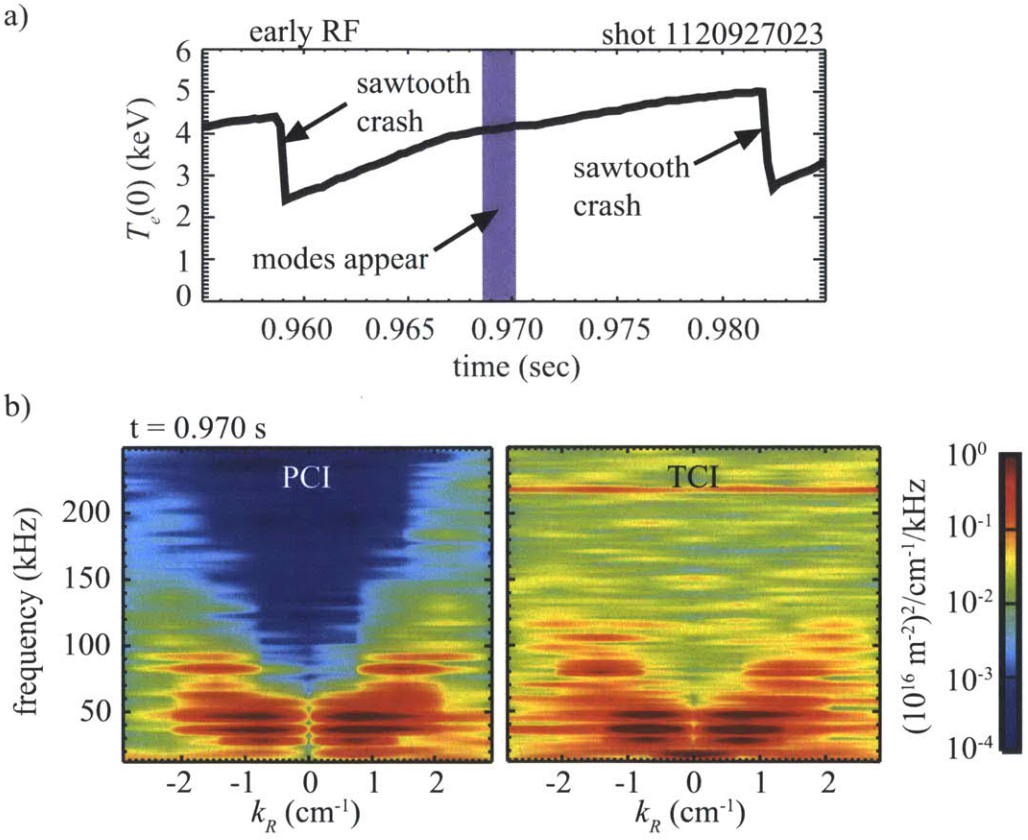

Figure 6-3: (a) On-axis electron temperature during single sawtooth period. (b) PCI and TCI $S(f, k_R)$ spectra during the highlighted period.

similar in Figures 6-3 and 6-4, but appear to be have been shifted in frequency. Figure 6-5 shows the line-averaged toroidal plasma rotation, and there is a clear difference

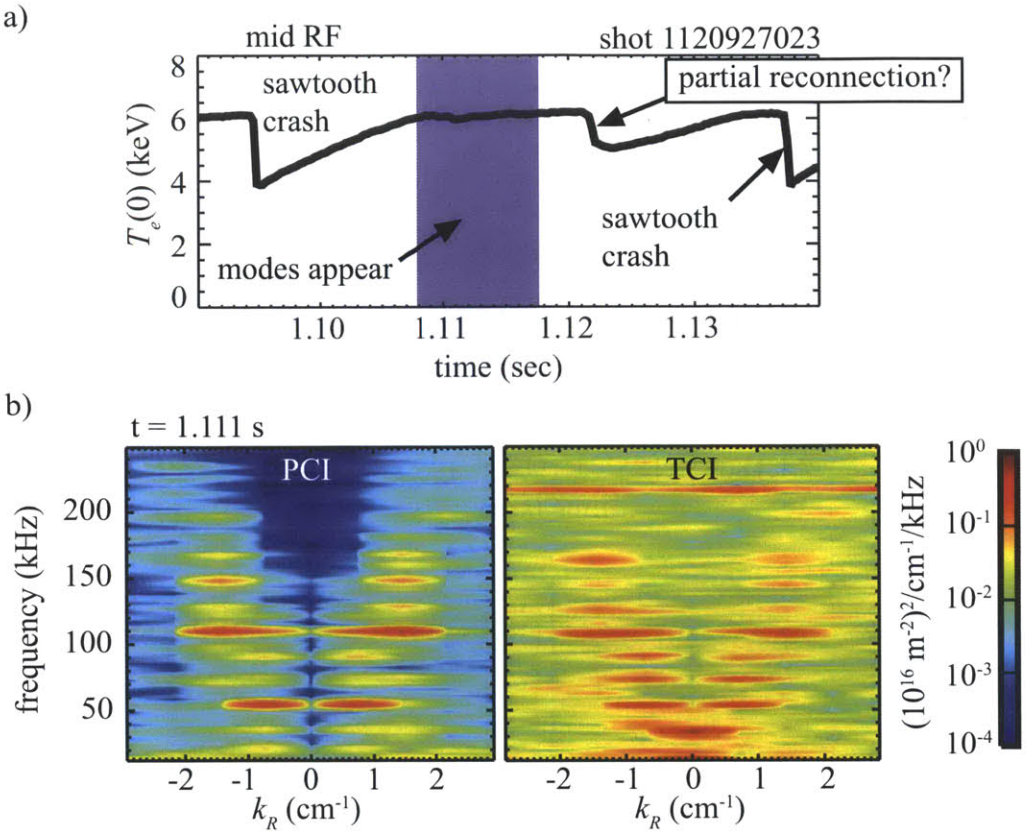

Figure 6-4: (a) On-axis electron temperature during single sawtooth period. (b) PCI and TCI $S(f, k_R)$ spectra during the highlighted period.

in rotation between the two time points shown in Figures 6-3 and 6-4. The increased rotation suggests that the frequency shift is due to a Doppler shift. The observed Doppler shift will be used to partially localize the modes radially.

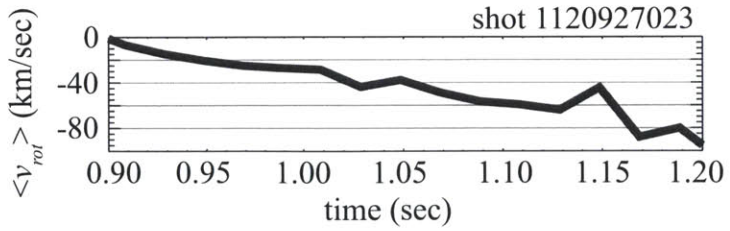

Figure 6-5: Average toroidal rotation in the discharge of interest.

The final type of sawtooth in the discharge of interest occurs late in the RF phase. An example is shown in Figure 6-6. Following a crash, the on-axis electron

temperature gradually increases before reaching a plateau for almost 10 ms. During the plateau, the modes again appear in the PCI and TCI fluctuation spectra.

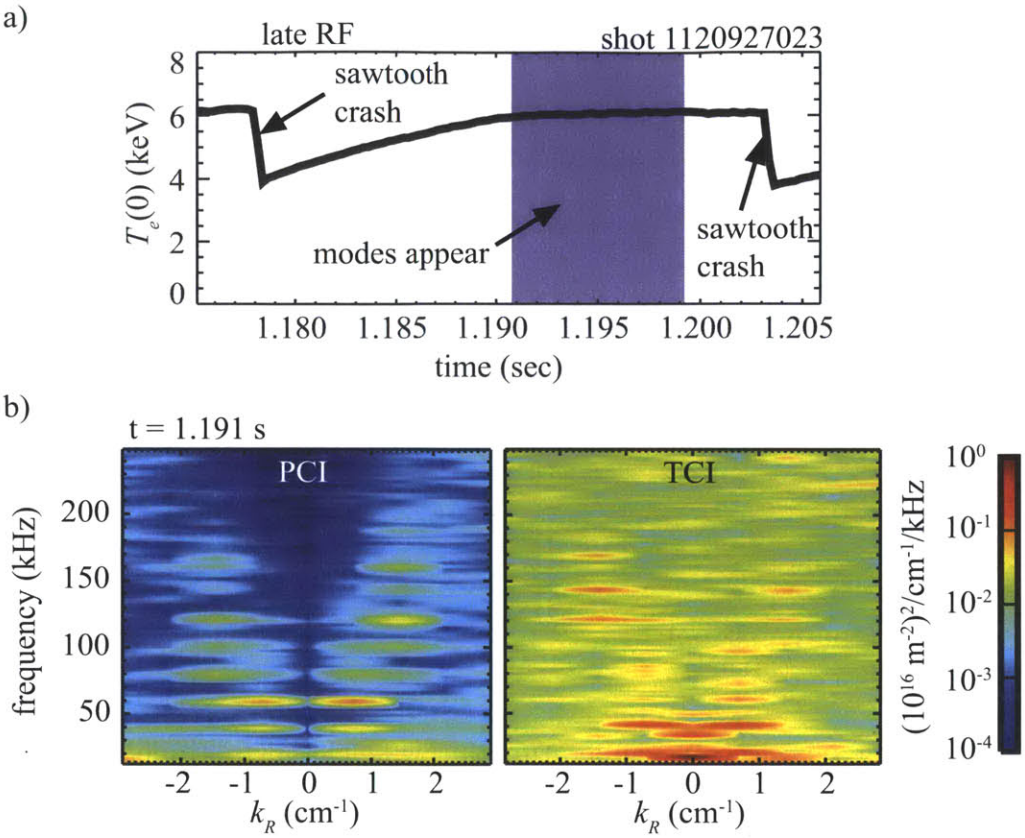

Figure 6-6: (a) On-axis electron temperature during single sawtooth period. (b) PCI and TCI $S(f, k_R)$ spectra during the highlighted period.

The remainder of this chapter will attempt to characterize these modes.

6.2 Core Localization

Two-color interferometry and phase-contrast imaging are both line-integrated diagnostics, and thus they simultaneously measure fluctuations occurring in the edge and in the core. Absent additional information, it is impossible to determine where measured fluctuations are spatially located. Despite this limitation, data from other diagnostics can provide additional information about the spatial location of the observed fluctuations.

It should be noted that the PCI diagnostic on Alcator C-Mod does have the ability to distinguish between fluctuations occurring above or below the midplane by partially masking the phase plate.[82] PCI was not configured to make those measurements for the discharge of interest, and the masked configuration still would not provide profile localization.

6.2.1 Reflectometry

O-mode reflectometry is used to measured qualitative electron density fluctuations in Alcator C-Mod. Reflectometers send RF radiation into the plasma at a certain frequency, and the radiation propagates into the plasma until it reaches the cut-off layer. The cut-off layer is the location where its frequency matches the electron plasma frequency, which is a function of the electron density. When the propagating wave reaches the cut-off layer, it is reflected, and the reflected wave is detected. Information about local electron density fluctuations is derived from the collected signals.

Alcator C-Mod has reflectometers at a variety of frequencies. For the discharge of interest, data was collected from reflectometers at 60, 75, and 88 GHz. Reflectometers at 112 and 140 GHz were unavailable. Cut-off locations for all five reflectometers are shown in Figure 6-7. The 88 GHz reflectometer measures fluctuations just inside the last-closed flux surface (LCFS) in the region $0.95 \leq r/a \leq 1.0$, and the 60 and 75 GHz reflectometers measure fluctuations outside of the LCFS in the scrape-off layer (SOL). The 112 GHz reflectometer would have provided useful measurements from $0.5 \leq r/a \leq 0.7$, but it was not available during the 2012 Alcator C-Mod run campaign. The 140 GHz reflectometer density cut-off layer is higher than any density achieved during the discharge of interest, and thus would not have provided any valuable measurements even if it had been operational.

The fluctuation measurements from the three available reflectometry channels are shown in Figure 6-8(b-d), and the fluctuation spectrum measured by a single PCI chord is shown in Figure 6-8(a). The series of coherent features that are visible in the PCI fluctuation spectra do not appear in any reflectometry channels. This is evidence that the fluctuations are not localized to the edge/SOL ($r/a > 0.95$).

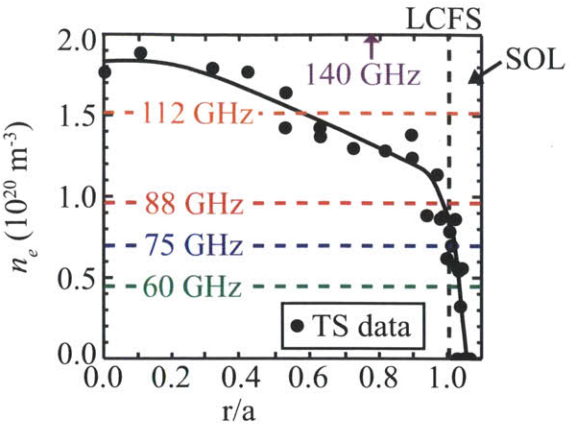

Figure 6-7: Reflectometer cut-off locations. The density profile is fit with Thomson scattering (TS) data. The 140 GHz cut-off location is at $n_e \sim 2.42 \times 10^{20}$ m^{-3}.

6.2.2 Magnetics

Magnetic field pick-up coils are located around the edge of Alcator C-Mod and can measure electromagnetic fluctuations. The coils are typically only sensitive to the fields at the edge of the plasma because magnetic field lines in the core do not penetrate out to the edge. The exception is during sawtooth events which exhibit extremely large electromagnetic activity. Except briefly during sawtooth events, magnetic pick-up coils provide information about edge electromagnetic fluctuations, which can provide some insight into electron density fluctuations.

Figure 6-9 shows an autopower spectrum from an edge magnetic field pick up coil. There are low frequency oscillations which are related to magnetohydrodynamic (MHD) activity and probably neoclassical tearing modes, and there are occasionally high-frequency bursts of fluctuations during sawtooth events. However, there are no quasi-periodic, coherent features present during the steady period between sawtooth events, when coherent modes are observed by PCI and TCI. The absence of electromagnetic fluctuations suggests that the observed electron density fluctuation measurements are localized to the core plasma.

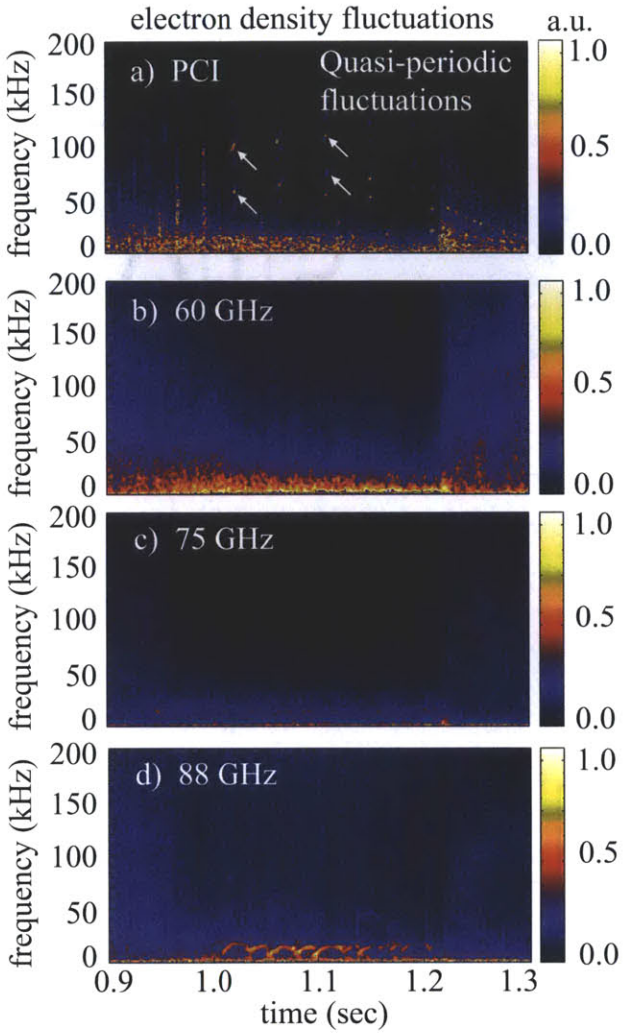

Figure 6-8: Electron density fluctuations measured by (a) PCI (cross-correlation between two adjacent chords), (b) the 60 GHz reflectometer, (c) the 75 GHz reflectometer, and (d) the 88 GHz reflectometer.

6.2.3 Plasma Rotation

As the plasma transitions from L-mode into I-mode, its rotation frequency increases as a result of the increase in the stored energy of the plasma.[80] The increased rotation results in a Doppler shift in the observed fluctuation frequencies (see Figures 6-3, 6-4, and 6-6). With knowledge of the plasma rotation profile and the magnitude of the Doppler shift in the PCI and TCI signals, the fluctuations can be partially localized.

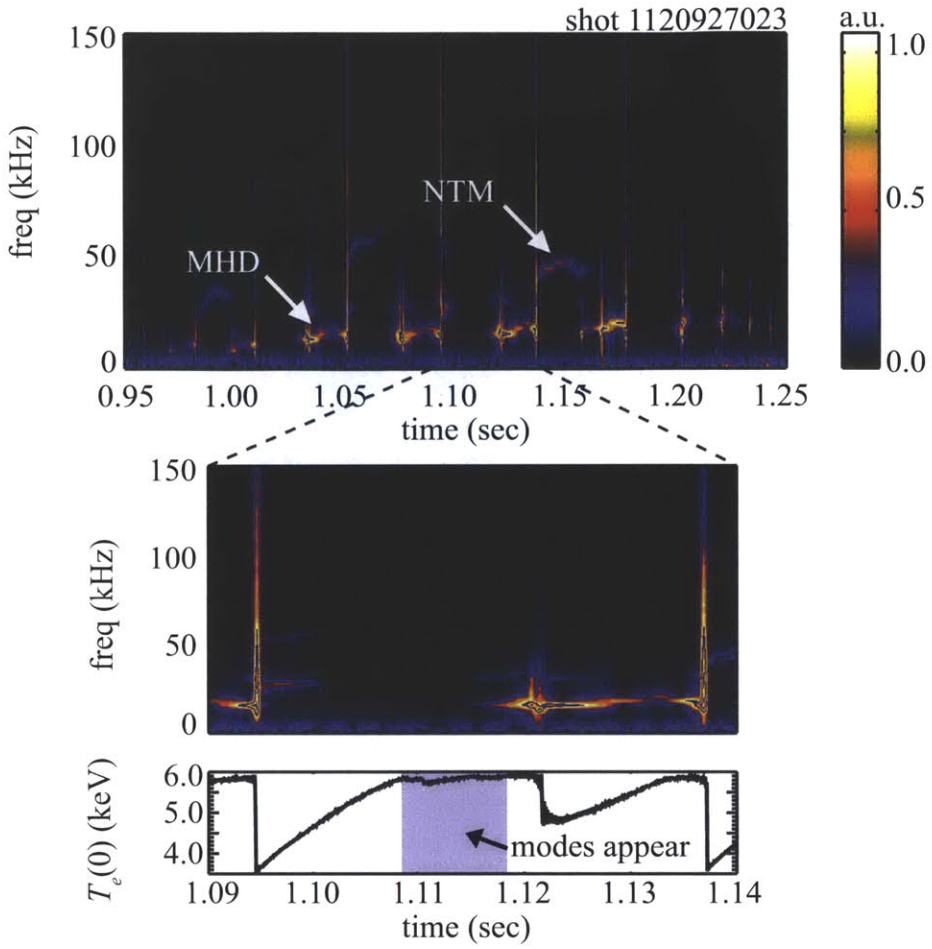

Figure 6-9: Magnetics fluctuations measured by edge pick-up coils.

The observed frequency of a Doppler shifted wave is,

$$f = \left(1 - \frac{v_{rot}}{c}\right) f_0 \tag{6.1}$$

where f is the observed frequency in the lab frame, f_0 is the true frequency of the wave in the rotating frame, v_{rot} is the plasma rotation velocity relative to the lab frame, and c is the speed of the wave in the rotating frame. The quantities f_0 and c are not known, and v_{rot} and f are known. The effect of the Doppler shift can thus be analyzed proportionally. The observed Doppler shift, δf, is the difference between f

and f_0, and is related to the plasma rotation velocity using Equation 6.1,

$$\begin{aligned} \delta f &= f - f_0 = -\frac{v_{rot}}{c} f_0 \propto v_{rot} \\ \Delta(\delta f) &\propto \Delta v_{rot}. \end{aligned} \tag{6.2}$$

The last line is the change in the observed Doppler shift, which can be detected by PCI and TCI measurements by following the time evolution of a specific fluctuation. It is assumed that the fluctuation has a fixed wavenumber ($\propto f_0/c$) in the rotating frame.

Equation 6.2 says that the change in the observed Doppler shift of the fluctuation is proportional to the change in the rotation velocity of the plasma. The rotation velocity is related to the plasma rotation frequency, f_{rot},

$$v_{rot} = 2\pi R f_{rot}$$

so at a fixed major radius, $v_{rot} \propto f_{rot}$. From Equation 6.2, at a given major radius the observed Doppler shift will be proportional to the change in the plasma rotation frequency,

$$\Delta(\delta f) \propto \Delta f_{rot} \text{ (fixed } R). \tag{6.3}$$

Equation 6.3 is used to partially localize PCI and TCI measurements in the following way. First, one of the Doppler-shifted coherent fluctuations shown in Figures 6-3, 6-4, and 6-6 is selected. Figure 6-10 shows the selected mode appearing at several times throughout the discharge. The low frequency, low-k_R modes are hard to distinguish from each other, but the first mode appearing at $|k_R| \approx 1.4$ cm^{-1} is clearly visible at each time point. Figure 6-10 shows the time evolution of the fluctuation. There is some ambiguity at $t = 0.970$ s, but it should be noted that the mode in the black box is nearly an order of magnitude larger than other features occurring at lower frequencies at the same k_R. The boxed mode is also much more well-defined in k_R-space than other fluctuations near the same k_R. The well-defined k_R and relative mode strength removes some of the ambiguity about the frequency of the first

$|k_R| \approx 1.4$ cm^{-1} mode. The measured frequencies of the chosen fluctuation are 80 kHz ($t_1 = 0.970$ s), 110 kHz ($t_2 = 1.111$ s), and 122 kHz ($t_3 = 1.191$ s).

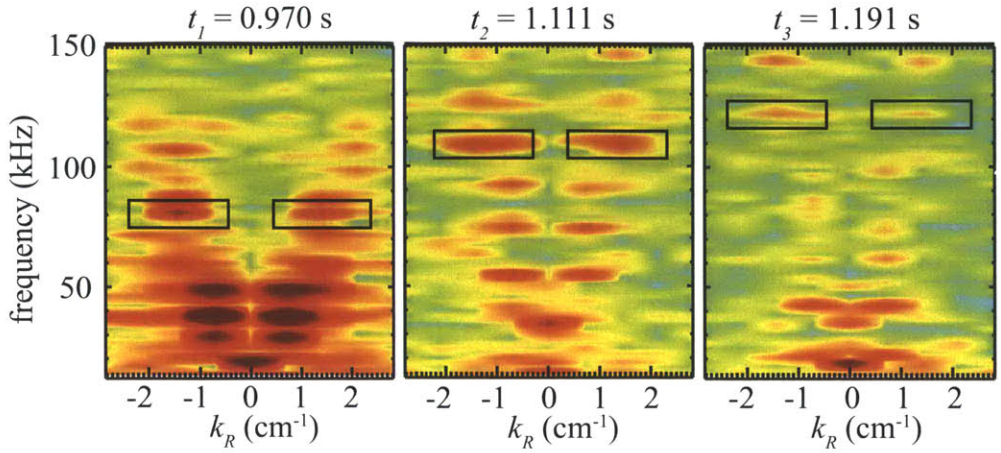

Figure 6-10: TCI fluctuation spectra with identified modes for Doppler shift analysis.

Profiles of the plasma rotation frequency, f_{rot}, are available from high-resolution x-ray crystal spectroscopy measurements of the line emission from argon impurities.[21, 22] The profiles are shown at several time points of interest in Figure 6-11. The plasma rotation tends to increase as the observed mode frequency increases.

Finally, the approximate radial location of the fluctuations can be determined by examining the Doppler shift. Equation 6.3 can be recast in terms of unknown constants at each major radial location,

$$\Delta(\delta f) = C_i \Delta f_{rot} \text{ (fixed } R_i). \tag{6.4}$$

The measured change in the Doppler shift frequency, $\Delta(\delta f)$, is calculated three times at eight radial locations. The first calculation is performed between $t_1 = 0.970$ s and $t_2 = 1.111$ s, the second calculation is between $t_3 = 1.191$ s and t_1, and the final calculation is between t_3 and t_2. The calculations generate three constants, C_i, at each radial location R_i. By Equation 6.4, the constants at a given radial location should be equivalent if the fluctuation occurs at that radial location. The constants at each radial location for all three calculations are shown in Figure 6-12. Figure 6-12a shows the full range of the calculated constants, and Figure 6-12b is zoomed in to show more

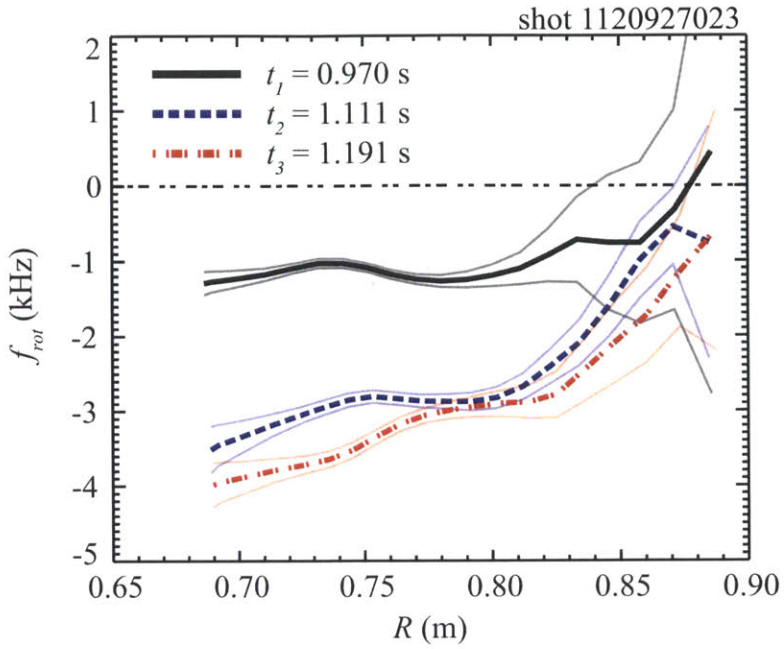

Figure 6-11: Plasma rotation profiles at three time points in the discharge of interest.

detail. The plasma rotation measurement by x-ray crystal spectroscopy is unreliable outside of about $r/a = 0.6$. The $t_3 - t_2$ calculation has high uncertainty because the measured plasma rotation frequencies at those two time points are nearly identical, and the frequency difference appears in the denominator of the error propagation equation.

For $r/a \leq 0.3$, the relationship between the expected change in Doppler shift to the measured change in frequency of the fluctuation is satisfied, suggesting that the modes are occurring deep in the plasma core, inside the sawtooth inversion radius at $r/a \sim 0.35$. Further out ($r/a \sim 0.4 - 0.5$), the fluctuations observed in the PCI and TCI spectra do not satisfy the expected Doppler shift relationship, implying that the modes are not occurring at those radial locations. However, the data cannot rule out the possibility that the Doppler shift condition is met from $r/a \sim 0.6 - 0.95$, due to inadequate plasma rotation data in that region.

The absence of magnetics fluctuations provides some evidence that the modes observed in the TCI and PCI spectra are not occurring from $0.6 \leq r/a \leq 0.95$. The 60, 75, and 88 GHz reflectometers and the magnetics data also rule out the possibility that

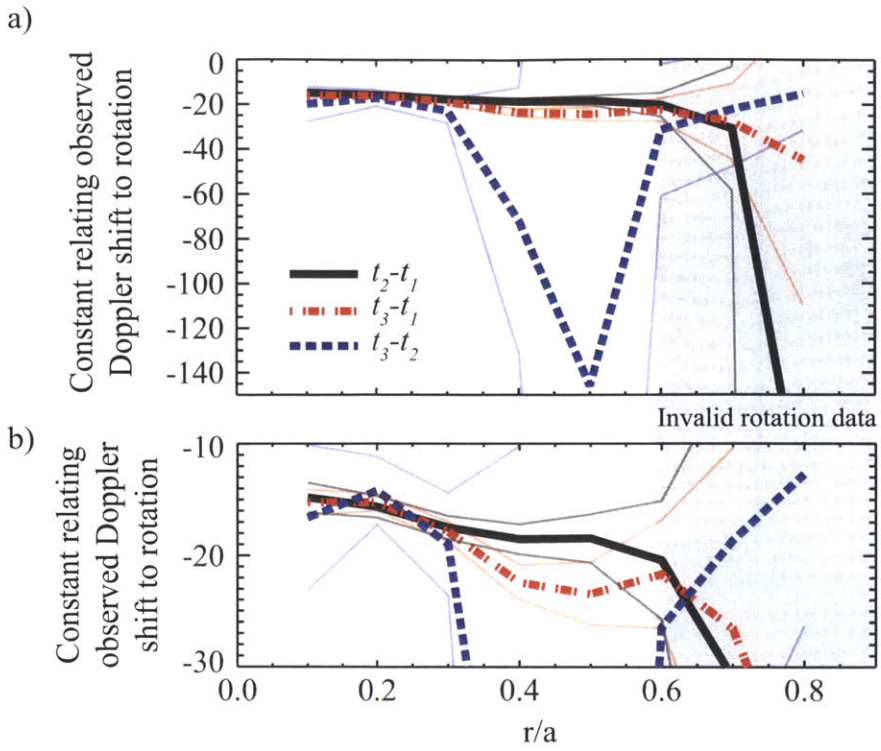

Figure 6-12: The constant factor relating the measured change in the Doppler shift of fluctuations to the change in plasma rotation. (a) Full range of the calculated constants, (b) higher detail.

the observed modes are located at the far edge or in the SOL ($r/a \geq 0.95$). Doppler shift measurements suggest that the fluctuations are located within $r/a \leq 0.4$. Taken together, the magnetics, reflectometry, and rotation measurements all indicate that the fluctuations observed in the TCI and PCI spectra are spatially localized deep into the plasma core at $r/a < 0.4$, inside of the $q = 1$ surface at $r/a \sim 0.35$.

6.3 One-Dimensional Transport Analysis

The effect of the observed fluctuations on the overall heat transport is examined using the one-dimensional experimental global transport code TRANSP.[83] TRANSP accepts a variety of different measurements as inputs and calculates the time-varying heat flux and heat diffusion profiles. For the discharge of interest, several non-standard inputs needed to be accounted for before a successful TRANSP analysis

could be performed.[1] First, the TRANSP input file had to be modified so that a Fokker-Planck solver was used to calculate the distribution functions of multiple minority species. Typically, only a single minority species is analyzed using the Fokker-Planck solver, but the MC/MH discharge of interest had approximately a 10% He-3 fraction and a 4% H fraction, and both concentrations are large enough to require the Fokker-Planck solver. Additionally, the ICRF antenna frequencies and phasing needed to be carefully adjusted to account for the input power at the non-standard 50 MHz frequency used for mode-conversion experiments.

The most important inputs for TRANSP are profiles of the electron temperature and density. Density profiles were fit to Thomson scattering data, and temperature profiles were derived from electron cyclotron emission and Thomson scattering measurements. The time resolution is limited by the Thomson scattering measurements, which is 10 ms. TRANSP also accepts ion temperature and rotation profiles, but attempts to incorporate measured profiles into TRANSP failed due to data quality issues. Instead, model profiles are used. The ion temperature profiles are constrained by measurements of the neutron rate from $D - D$ fusion reactions. The electron density and temperature profiles at three time points through a sawtooth cycle are shown in Figure 6-13. There are significant changes in the profiles, suggesting significant changes in heat transport. A fluctuation is observed in the PCI and TCI spectra at $t = 0.970$ s, but is not observed at the other time points shown in Figure 6-13.

The TRANSP simulations do not show any clear correlation between changes in the electron heat flux and the appearance of the fluctuations in the PCI and TCI spectra. Figures 6-14, 6-15, and 6-16 show electron heat flux profiles (due to conduction) through a single sawtooth for each of the three types of sawtooth events identified above. In the early RF phase (Figure 6-14), the heat flux in the core region is approximately the same before and during the period when the fluctuations are observed in the TCI and PCI spectra. Near the edge, the heat flux during the fluctuation period is larger (more positive), but does not decrease when the fluctuations

[1]The author thanks Paul Bonoli for successfully modifying the TRANSP input files for the discharge of interest.

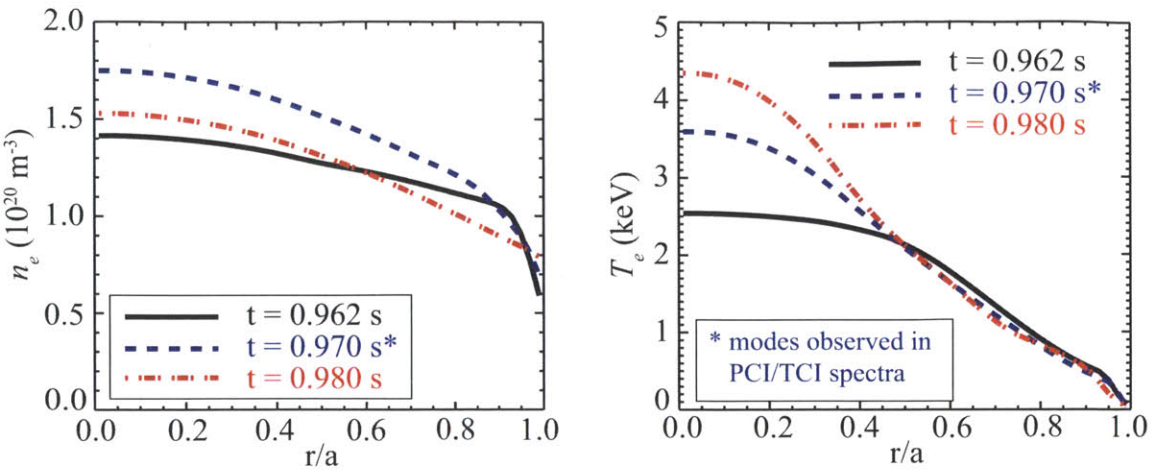

Figure 6-13: Electron temperature and density profiles used for TRANSP analysis.

vanish. There is no correlation between the observed heat flux and the presence of the electron density fluctuations. In the mid (Figure 6-15) and late (Figure 6-16) RF phases, the heat flux profiles generally increase with time in both the core and the edge, regardless of whether or not there is an observed electron density fluctuation. It appears that there is no correlation between enhanced electron thermal transport and the presence of the electron density fluctuations observed in the PCI and TCI spectra.

6.4 Linear Stability Analysis

The previous section provides evidence that the observed fluctuations do not contribute to electron thermal transport, but clearly there is a feature within the plasma which experiences rapid growth and decay. The fluctuations appear to be a series of coherent modes, which suggest that they are some sort of electromagnetic or magnetohydrodymanic (MHD) mode. However, it has not yet been ruled out that the features are destabilized drift-wave turbulence such as the trapped electron mode (TEM).

The drive terms which can destabilize drift-wave turbulence include the electron density gradient, the electron temperature gradient, and the ion temperature

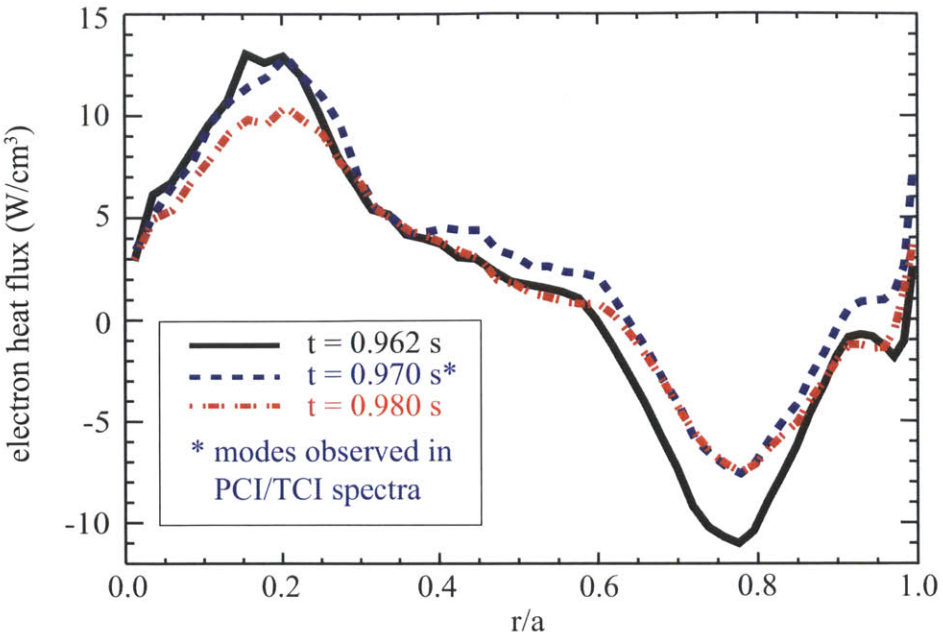

Figure 6-14: Heat flux profiles through a single early RF sawtooth cycle.

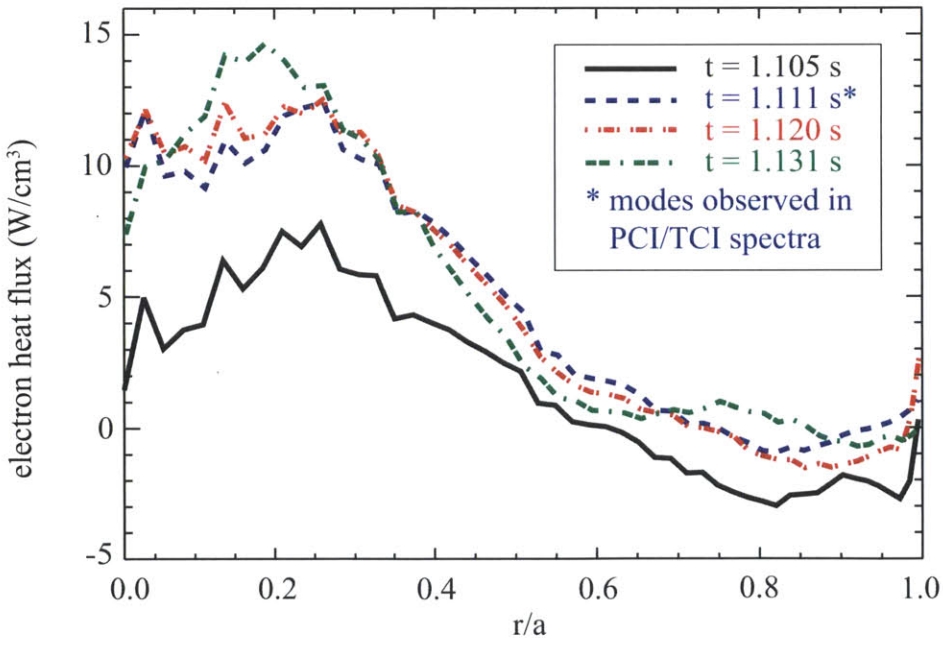

Figure 6-15: Heat flux profiles through a single mid RF sawtooth cycle.

gradient.[84] Measurements of the ion temperature profile were not very reliable for the discharge of interest, but electron temperature and density profiles are available

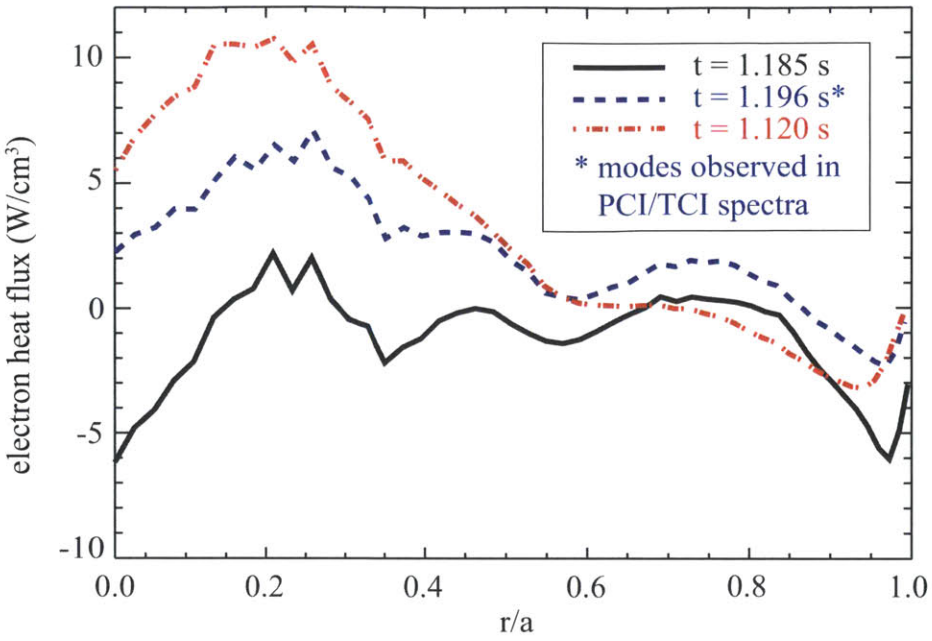

Figure 6-16: Heat flux profiles through a single late RF sawtooth.

using Thomson scattering and electron cyclotron emission measurements. The experimental profiles are used as inputs to the TRANSP one-dimensional global transport code, and TRANSP maps the profiles onto a grid appropriate for linear stability analysis.

The potential drivers of drift-wave turbulence are shown in Figures 6-17 and 6-18. Figure 6-17 are the gradients of the electron density and temperature calculated from the data in Figure 6-13. The gradients are clearly larger at $t = 0.970$ s when the mode appears than at the time point before the mode appears. It is tempting to hypothesize that the modes are drift-wave turbulence destabilized by the changing electron temperature and density profiles through the sawtooth cycle. However, the gradient continues to increase even after the modes disappear at 0.980 s. Similarly, Figure 6-18 shows the normalized electron density and temperature gradient scale lengths calculated from the data in Figure 6-17. The scale length is defined as,

$$L_x = \left(\frac{d \ln x}{dr} \right)^{-1}.$$

The normalized gradient scale length drive terms also increase when the mode appears, but continue to increase after the mode vanishes.

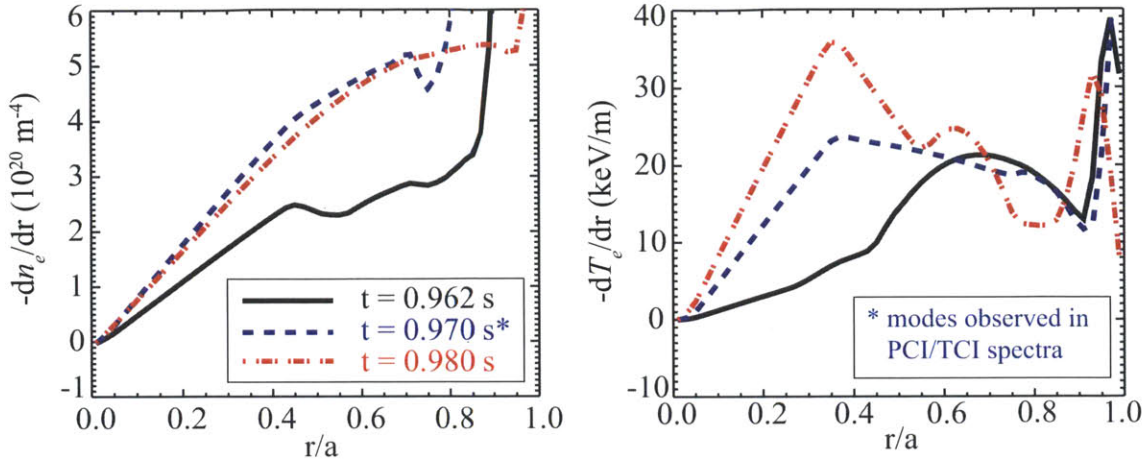

Figure 6-17: Electron temperature and density gradients which may drive drift-wave turbulence.

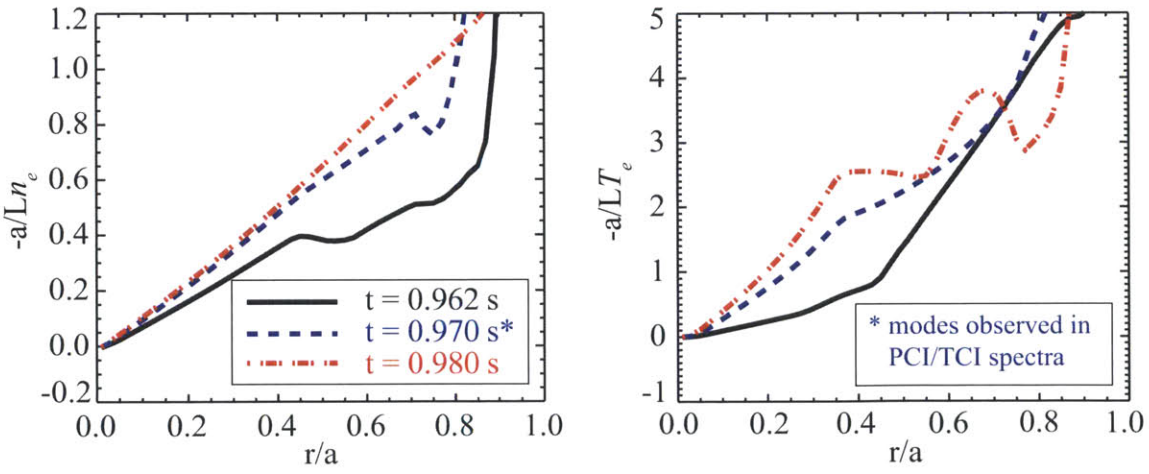

Figure 6-18: Electron temperature and density gradient scale lengths.

Because of the behavior of the drive terms in Figures 6-17 and 6-18, it is unlikely that the observed features in the PCI and TCI spectra are destabilized drift-wave turbulence. In an effort to rule out the possibility that the features are the result of destabilized turbulence, the linear gyrokinetic stability of drift-wave turbulence is calculated. GYRO[12] is a Eulerian solver for the nonlinear gyrokinetic-Maxwell

equations[10, 11] which form the basis of gyrokinetic theory. The code can be used to determine the linear stability of drift-wave turbulence at a given radial location.

The results of linear stability analysis[2] of an early RF sawtooth ($t = 0.962 - 0.98$ s) from $r/a = 0.3 - 0.8$ is shown in Figure 6-19. The real frequency and the growth rate are averaged over low-k turbulence, for $k_y\rho_s \leq 0.2$. k_y is the poloidal wave number and ρ_s is the ion sound gyro radius, which is defined as $\rho_s = c_s/\Omega_{ci}$, where $c_s = \sqrt{T_e/m_i}$ and $\Omega_{ci} = eB/m_i$.

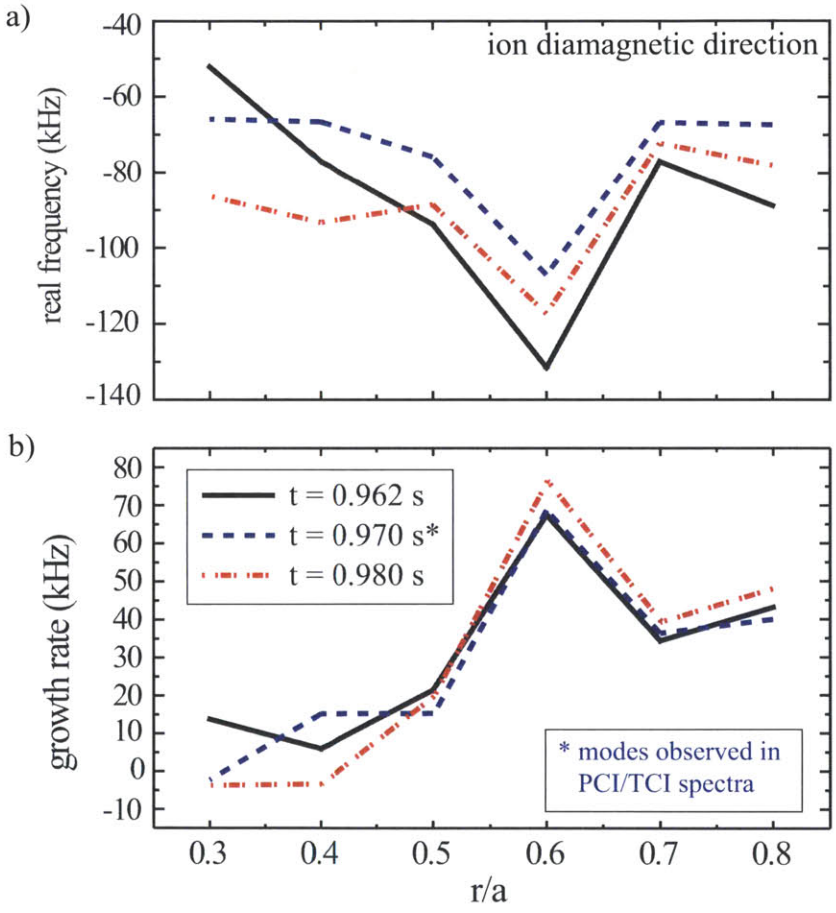

Figure 6-19: (a) Real frequency and (b) growth rate from gyrokinetic linear stability analysis, averaged from $k_y\rho_s < 0.2$.

Not surprisingly, the growth rate of the turbulence in Figure 6-19 does not change significantly through the sawtooth cycle. No clear trend is visible in the growth rate of the turbulence, and the growth rates themselves are very small. This implies that

[2]The author thanks Choongki Sung for performing the linear stability analysis.

there is no significant drift-wave turbulence present in the core plasma, and particularly, there is no destabilized turbulence when the fluctuations appear in the PCI and TCI spectra. Drift-wave turbulence is not the cause of the observed fluctuations.

6.5 Discussion

While the identities of the fluctuations observed in the PCI and TCI spectra have not been determined, they have been well-characterized. The fluctuations appear only during brief quiescent phases while the plasma recovers from large sawtooth events, and they are only observed during the I-mode phase of the discharge while 50 MHz and 80 MHz ICRF heating is turned on. The fluctuations do not appear to extend beyond $|k_R| \approx 2$ cm^{-1}, or above $f \approx 200$ kHz.

The fluctuations appear to be a series of discrete modes which are probably localized deep into the plasma core, inside of the sawtooth inversion radius. The modes do not appear on edge magnetics signals, but this does not rule out the possibility that they are electromagnetic because the edge pick-up coils are insensitive to core magnetics. Transport analysis shows that the fluctuations do not affect electron heat transport, and linear stability analysis shows that the modes are not related to drift-wave turbulence.

The modes appear to be a fairly benign feature occurring deep in the core of quiescent ICRF mode-conversion/minority-heated I-mode plasmas.

Chapter 7

Conclusion

The two-color interferometer diagnostic on Alcator C-Mod has been successfully upgraded to measure line-integrated electron density fluctuations. The new system has been used to verify the low-k_R response and absolute calibration of the phase-contrast imaging diagnostic, improving the confidence of quantitative validation studies conducted between PCI and turbulence codes like GYRO. While the present TCI system has contributed in a small way to the field of plasma fluctuation diagnostics and gyrokinetic transport model validation, with additional upgrades the system has the potential to be considerably better. The following chapter summarizes the new TCI capabilities, outlines some additional applications, and discusses possible improvements.

7.1 Summary of New Capabilities

The time resolution of the two-color interferometry system has been increased from 2 kHz to up to 10 MHz by upgrading the phase demodulation electronics and digitizers. The uncertainty in the line-integrated electron density is comparable to the uncertainty of the previous system, as determined by calculating the RMS value of pre-plasma phase shift signals. Standard line-integrated electron density measurements have not been adversely affected by the electronics upgrade.

The increased time resolution of the TCI system now enables measurements

of spatially-resolved line-integrated electron density fluctuations. Nine operational chords provide the spatial resolution, and signed major-radial wavenumbers have been resolved from $|k_R| \lesssim 3$ cm^{-1} with $\Delta k_R \sim 0.7$ cm^{-1}. The relatively low number of chords (9), combined with the fairly small beam width through the plasma ($\sim$ 10 cm), severely limits the resolution and the maximum resolvable fluctuation wavenumber. However, this thesis has proven that useful spatially-resolved fluctuation measurements can still be made despite these limitations.

Quoted uncertainties in the measured fluctuations are approximately $\pm 4.1 \times 10^{15}$ m^{-2}, which is approximately $\sim 5 - 20\%$ of typical fluctuation levels. This is fairly high, but the analysis used to calculate the uncertainty is very conservative, and in reality the uncertainty is usually much smaller. Regardless of the uncertainty due to the phase demodulators, the more important issue limiting the performance of TCI as a fluctuation diagnostic is the high level of uncorrelated noise. The uncorrelated noise is probably due to lack of beam power through the optics system. Uncorrelated noise levels are typically near the levels of the larger fluctuations present in the plasma, and thus prevent some fluctuations from being detected.

Despite the issues with limited spatial resolution and high noise levels, the diagnostic has been successfully compared to phase-contrast imaging. Qualitative comparisons show that many of the same fluctuations are detected by both systems. Quantitative comparisons have increased the confidence in the PCI absolute calibration and low-k_R response function. PCI is frequently used for quantitative comparisons between experiments and theoretical predictions with gyrokinetic codes like GYRO. These comparisons use a synthetic PCI diagnostic, and therefore rely heavily on accurate wavenumber response functions and absolute calibration factors. While TCI most likely lacks sufficient spatial resolution and has too much noise to be used as a code validation diagnostic in its present form, the partial verification of the PCI response function and absolute calibration is a useful contribution to validation efforts with PCI.

7.2 Additional Applications

The first generation TCI fluctuation diagnostic described in this thesis has been shown to be useful for quantitative comparisons to PCI, for measurements of coherent modes, and for measurements of strong long wavelength fluctuations. With some additional upgrades, the system could be used for a variety of other purposes. The full PCI wavenumber response and absolute calibration could be verified, and detailed measurements of long wavelength turbulence with high sensitivity could be made. Quantitative measurements of changes in turbulence (ITG/TEM) across different plasma confinement regimes could be studied. With the creation of a synthetic GYRO diagnostic for TCI, quantitative turbulence code validation studies could be performed.

PCI has been considered the standard quantitative electron density fluctuation diagnostic for several years, but its utility has been limited by its nonlinear wavenumber response function and by uncertainty in its calibration. The simpler TCI diagnostic could approach or even surpass the performance of PCI, because TCI can access low-k_R fluctuations. Additionally, the absolute calibration of TCI is well-known from very basic plasma physics theory. Further upgrades are still needed to fully realize the potential of TCI as a fluctuation diagnostic; several of these required changes are now described.

7.3 Potential Upgrades

In Chapter 4 it was pointed out that the upgraded two-color interferometer has noise levels which approach the level of electron density fluctuations. The noise levels could be reduced with an increase in the laser throughput, improving beam alignment, and adjusting the CO_2 beam profile. The present system employs a 50/50 beam splitter immediately following the output of the CO_2 laser, with half the power diverted to a power detector to monitor the stability of the laser. The laser stability can be monitored with less power, so an 80/20 beam splitter was briefly installed to increase

the laser throughput. Unfortunately, issues arose with other optical components in response to the increased laser power, and the 50/50 splitter was re-installed before the new system could be tested. With upgraded optics, increasing the laser power through the system would almost certainly reduce the noise level. Additionally, the system alignment should be improved by robustly eliminating beam shear, which occurs when the plasma and reference beams are not perfectly co-axial when they are rejoined on the detector plane. Eliminating beam shear would reduce beam incoherence on the detector face and, as a result, increase the signal levels. Adjustments to the CO_2 beam profile could also improve system performance by reducing crosstalk between adjacent channels.

Another issue with the present TCI system is a frequent CO_2 laser cavity instability which causes large levels of coherent noise. Future TCI systems could benefit from using the same laser cavity to create both the primary probe beam and the secondary beam for vibration subtraction. Since the noise oscillation is common to the primary and secondary beam, the coherent noise would be eliminated with the vibration subtraction. Several different methods employing the same laser cavity could be used. FIR lasers can laze simultaneously at multiple wavelengths, as is done on the Large Helical Device.[36] The near infrared (IR) Nd:YAG laser can be frequency doubled, yielding two beams in the IR and the visible. A frequency-doubled Nd:YAG laser has been employed with moderate success on the tangential TCI system on Alcator C-Mod.[85]

Apart from high levels of uncorrelated and coherent noise, the present TCI system lacks high spatial resolution and fails to detect fluctuations at high wavenumbers. These limitations arise because the number of detectors in the detector array is low and the major-radial width of the CO_2 beam is small. Increasing the number of detectors and the width of the beam, while simultaneously decreasing the spacing between adjacent detectors, will increase the wavenumber range while also improving the wavenumber resolution. When combined with increased beam power, such an upgrade to the detection system would allow TCI to approach the performance of phase-contrast imaging, and could be used to verify the PCI high-k_R response. With

levels of performance similar to PCI, TCI could also be used as another diagnostic for quantitative comparisons to predictive turbulent transport codes like GYRO. Additionally, increasing the number of chords could potentially provide the capability to invert the line-integrated measurements to generate electron density profiles.

In summary, the following upgrades would significantly improve the capabilities of the TCI line-integrated electron density fluctuation diagnostic:

- Increase laser power through the system;
- Improve laser alignment - remove beam shear and ensure co-linearity of plasma and reference beams;
- Adjust CO_2 beam profile to reduce crosstalk between channels;
- Derive primary and secondary beams from the same laser cavity;
- Increase number of detectors;
- Decrease spacing between detectors;
- Decrease major-radial dimension of detectors;
- Increase major-radial range of detector array.

Appendix A

TCI Analysis Routine

The changes to the two-color interferometer electronics described in Chapter 3 represented a dramatic change in how the phase is calculated from the detector signals. Previously the phase was calculated with a combination of analog and digital fringe-counting electronics, with the resulting phase measurement being digitized directly. A post-processing routine existed primarily to ensure that the data was of sufficient quality to merit permanent storage in the form of a line-integrated density signal, and to provide the vibration subtraction. The new electronics now store signals proportional to the sine and cosine of the measured phase shift, requiring much more intricate post-shot processing and data analysis to provide line-integrated density signals.

A major component of this thesis project was developing the post-shot processing routine to accurately and efficiently reconstruct the measured phase of both the CO_2 and HeNe laser signals. The result was a complete overhaul of the previous TCI analysis routine. As the sole developer of the new TCI analysis routine, the author feels obligated to provide an in-depth written record of how the routine is designed and operated. That is the purpose of this Appendix.

Calling Procedure

The TCI analysis routine is run automatically after each Alcator C-Mod discharge, but can also be run manually from a terminal. The current version is

```
ftci_analysis_05.pro
```

and can be found in the

```
/usr/local/cmod/codes/electrons/tci
```

directory. TCI data is digitized at rates up to 10 MHz for several seconds, so a significant amount of data must be processed. Therefore, the routine should be run from a high-performance machine such as `alcdaq` or `psfcstor1`.

The routine requires three input arguments and also accepts a variety of keywords. The three input arguments are the C-Mod shot number and two arrays specifying which CO_2 and HeNe chords to write and which to ignore. For example,

```
IDL> ftci_analysis,1120927018,[1,1,1,1,1,1,1,1,0,0],[1,0,0,1]
```

will write the first eight CO_2 chords of shot 1120927018 using HeNe chords 1 and 4 for vibration subtraction. The zeros in the CO_2 chord array force those chords to be written to the MDSplus tree as an array of zeros. The zeros in the HeNe chord array simply mean those chords are omitted from the subroutine which fits the HeNe data for vibration subtraction; data for HeNe chords 2 and 3 will still be written to the MDSplus tree in this example.

The processed data can be accessed in the MDSplus `ELECTRONS` node:

```
\ELECTRONS::TOP.FTCI.RESULTS:
```

in the nodes given in Table A.1. For example, to read in the line-integrated density for chord 04 (the signal commonly used for plasma control):

```
IDL> nl04 = mdsvalue('\ELECTRONS::TOP.FTCI.RESULTS:NL_04')
```

There are many optional keywords which are outlined in Table A.2. The uses of these keywords will be described within the discussion of the program flow below.

Node	Description
NL_XX	Line-integrated electron density for chord XX (01-10)
PHS_XX	Line-integrated electron density with dc component subtracted (set by `nsmooth` keyword)
AMP_XX	Amplitude of raw CO_2 signals
DNL_YY	Line-integrated electron density from differential system for chord YY (01-09)
DPHS_YY	Line-integrated electron density from differential system with dc component subtracted (set by `nsmooth`)
H_PHS_ZZ	Phase from HeNe chord ZZ (01-04)
H_AMP_ZZ	Amplitude from HeNe chord ZZ
FRMS	Root-mean-square of the pre-plasma PHS_XX signals
FSUB	Root-mean-square of the pre-plasma NL_XX signals
DRMS	Root-mean-square of the pre-plasma DPHS_YY signals
DSUB	Root-mean-square of the pre-plasma DNL_YY signals
GC	Final "good" CO_2 chords (replaces input CO_2 array)
GH	Final "good" HeNe chords (replaces input HeNe array)
TIME	Timebase for all signals
RAD	Major-radial locations of NL signals

Table A.1: Node names for TCI data.

Program Flow

After checking input parameters and setting a variety of default values, the TCI analysis routine first calculates the beginning and end time of the plasma discharge. Magnetics signals are checked for existence; if none exist then the routine will only analyze and write 100 ms of data to the MDSplus tree. The reason for this is simply to limit the time required for the analysis routine to run when analyzing TCI test shot data. If magnetics signals exist, then the plasma current is loaded into the program. The discharge is defined to be in the plasma state when the total plasma current exceeds 40 kA, thus setting the starting and ending times of the plasma.

The first data the routine writes is a preliminary NL_04 signal for rapid display to the scientists and engineers in the control room. The preliminary signal is just the analog feedback signal with a relatively low time resolution. However, if the `debug` keyword is set then *no* signals are ever written to the MDSplus tree.

Next, the routine loads in the fast TCI time signal, truncates it to include only

Keyword	Description
`calib`	Incorporate calibration data into phase calculation
`file`	Calibration file
`noopt`	Turns off the optimization process in the vibration subtraction subroutine
`nsmooth`	Sets the level of dc subtraction for PHS and DPHS signals
`dig_thres`	Voltage threshold for subroutine which fixes random digitizer faults
`atan_thres`	Threshold for allowable number of ATAN "jumps" before a given chord is skipped
`raw_co2`	Writes the 'raw' (unsubtracted) CO_2 data to the PHS MDSplus nodes
`splinefit`	Forces cubic spline interpolation of the HeNe data for vibration subtraction
`parabolic`	Forces parabolic fitting of the HeNe data for vibration subtraction
`linear`	Forces linear fitting of the HeNe data for vibration subtraction
`debug`	Does not write any data to the MDSplus tree, but otherwise runs the same

Table A.2: Optional input keywords for TCI analysis routine.

times up to 50 μs before and after the plasma, and then writes the resulting array to the MDSplus tree.

The routine next checks whether or not to load a calibration file. If a calibration file is desired, the routine searches for and loads in the file specified by the `file` keyword. If the `file` keyword is not set, the default file is

`/home/ckasten/idl/tci/calibration/070312/calib.save`

which is the most recent calibration data taken to date. The data in this file was collected on 03 July 2012. The routine checks the calibration file for missing data and then stores the data in a useful format.

Next the routine loads, analyzes, and writes the HeNe data. First the raw sine and cosine data for a single HeNe channel is loaded and immediately truncated according to the plasma starting and ending times. The data is then checked for digitizer faults. During the implementation of the TCI system the digitizers were found to

occasionally rail randomly during data acquisition. While infrequent enough to not be a major concern, the arbitrarily large spikes in the data signals can complicate subsequent data analysis. Thus, when a fault is detected the data point of interest is taken to be the average of the adjacent data points. The threshold voltage that defines a digitizer fault can be set with the input keyword `dig_thres` and by default is 2.5 V. If the gain of the amplifiers is ever changed significantly, this value will need to change.

After loading, truncating, and checking a single channel of HeNe sine and cosine data, the routine finally calculates the time-varying phase signal. IDL provides an arctangent function that can resolve all four quadrants from $-180°$ to $+180°$, so the phase is calculated by,

$$\phi = \tan^{-1}\left(\frac{\sin\phi}{\cos\phi}\right).$$

In practice, the phase calculation is much more complicated due to discontinuities introduced by the IDL arctangent function's limited phase range. In Chapter 2 it was shown that a 10.6 μm CO_2 laser will have a phase shift of about 6 rads ($\sim 360°$) due to vibration. Thus, in even the best circumstances the entire range of the arctangent function will be needed to calculate the CO_2 phase shift. The HeNe channels will always exceed the arctangent function range due to its enhanced sensitivity to vibration. A robust algorithm was developed to reconstruct the true phase measurement by correcting the discontinuities in the output of the IDL arctangent function. The subroutine is described in Section 3.4, and an example of the raw phase calculated by the arctangent function and corrected phase is shown in Figure 3-11.

On occasion, poor alignment or loss of signal due to a disruption may result in very noisy data where the phase oscillates rapidly, giving many discontinuities. A threshold of 10^5 discontinuities has been set to limit the time the phase reconstruction takes to run. This threshold can be adjusted with the `atan_thres` keyword. When greater than 10^5 events are detected, the data is flagged as poor and the phase signal is written as -1.

Once the phase has been properly calculated, an arbitrary offset is subtracted so

that the pre-plasma phase shift is zero. The amplitude of the signal is computed by taking the square root of the sum of the squares of the sine and cosine signals. The phase and amplitude are written to the H_PHS_ZZ and H_AMP_ZZ nodes, respectively. The process is repeated for all four HeNe channels.

Next, the routine repeats the process for the CO_2 signals. Only the desired chords from the input array are written, and if bad data is encountered those signals are written as arrays of -1s. Once the phase has been properly calculated, the component from vibration must be subtracted to compute the line-integrated density. If the keyword `noopt` is not set (or is left as the default), a vibration subtraction optimization routine is called. This routine shifts the effective major-radial position of the HeNe channels relative to the CO_2 channels and searches for the minimum value of the pre-plasma root-mean-square (RMS) phase. When this value is found, the channel position is set to the value that resulted in the minimum pre-plasma RMS phase. If the `noopt` keyword is set, then the default chord positions are used. The full HeNe data is spatially fit according to the desired function (`linear`, `splinefit`, or `parabolic`) and interpolated onto the required CO_2 chord positions. The vibration subtraction is then performed according to Equation 2.47 for each CO_2 chord.

Once the plasma-induced phase shift is calculated, the line-integrated density is computed with Equation 2.33. One additional subroutine is called to remove unphysical density values resulting from lost fringes during violent plasma phenomena such as disruptions. Unphysical values are defined to be line-integrated densities above 4.5×10^{20} m^{-2} or below -1×10^{20} m^{-2}; values exceeding this range are written as -1.

Next the PHS_XX signals are calculated by subtracting off a smoothed signal, which removes the dc component and any low-frequency electronics and vibrational noise. The smoothing level is set by the `nsmooth` keyword. The default value of `nsmooth` is 800, corresponding to smoothing below 2.5 kHz for 2 MHz digitization. If the `raw_co2` keyword is set, then the CO_2 phase signals are written to the PHS_XX nodes without any vibration subtraction or smoothing.

Next, two values useful for determining the alignment and performance of the

diagnostic are calculated: the average pre-plasma root-mean-square phase value for each chord and the average pre-plasma root-mean-square value of the smoothed and subtracted signals. All the quantities are then written to the MDSplus tree.

After the fast line-integrated densities are written to the tree, down-sampled versions of the densities are written. These signals are written at 2 kHz instead of 2 MHz bandwidth and as a result they load much more quickly. Scientists and engineers who are not concerned with line-integrated density fluctuation measurements should use these signals, which are stored in the old TCI MDSplus node:

```
\ELECTRONS::TOP.TCI.RESULTS:NL_XX
```

Finally the routine writes the differential signals in the same way it wrote the line-integrated density signals. If the routine does not detect a plasma, the differential signals are not analyzed or written. Vibration subtraction, although much less important in the differential system than the standard system, is still performed.

Appendix B

Differential Interferometry

The differential interferometry system was briefly introduced in Chapter 3. The principle of differential interferometry is to use an adjacent plasma-viewing interferometer chord as the reference to demodulate any given chord. The result is that no common phase shifts are detected, so the resulting signal is proportional to the line-integrated major-radial electron density gradient,

$$\frac{\Delta\phi_p}{\Delta R} \propto \int \frac{\Delta n_e}{\Delta R} dz \sim \int \frac{dn_e}{dR} dz$$

where $\Delta\phi_p$ is the measured phase difference between two adjacent chords.

Differential interferometry has been used as a plasma diagnostic for the first time on the Madison Symmetric Torus (MST) reversed-field pinch experiment,[86, 87] and more recently a system was installed on the Helically Symmetric Experiment (HSX) stellarator.[88] The system on MST uses far infrared (FIR) laser beams and HSX employs a bias-tuned Gunn diode oscillator as the radiation source, whereas the system on Alcator C-Mod uses CO_2 beams. Regardless of the radiation source, the operational principles are similar. By using a "reference" beam that uses the same optics and nearly an identical path length as the probe beam, the effects of vibration are greatly minimized. The system on MST has been successfully used to measure magnetic fluctuation-induced particle transport.[89]

One additional advantage of differential interferometry, apart from the absence

of vibrational effects, is the potential for core-localized measurements of the electron density gradient. A geometric effect enters into the equation when the major-radial derivative is transformed into a minor-radial derivative (in the case of circular geometry). As a result, the phase-shift integral becomes weighted strongly toward the core plasma for chords traversing near the core.[89] Applying this method to non-circular plasmas such as those in Alcator C-Mod would require some additional analysis and would rely on accurate equilibrium reconstructions, but could in principle provide core-localized electron density gradient measurements.

One potentially important side effect of differential interferometry is the introduction of a low-k_R cutoff into the multi-chord fluctuation spectra. Fluctuations with a wavelength significantly longer than the spacing between the two adjacent chords cannot be detected because they induce the same phase shift in both channels. The phase shift from these fluctuations is lost in the demodulation process, and the result is a low-k_R cutoff in the fluctuation spectra. An example spectrum is shown in Figure B-1; there is a clear low-k_R cutoff.

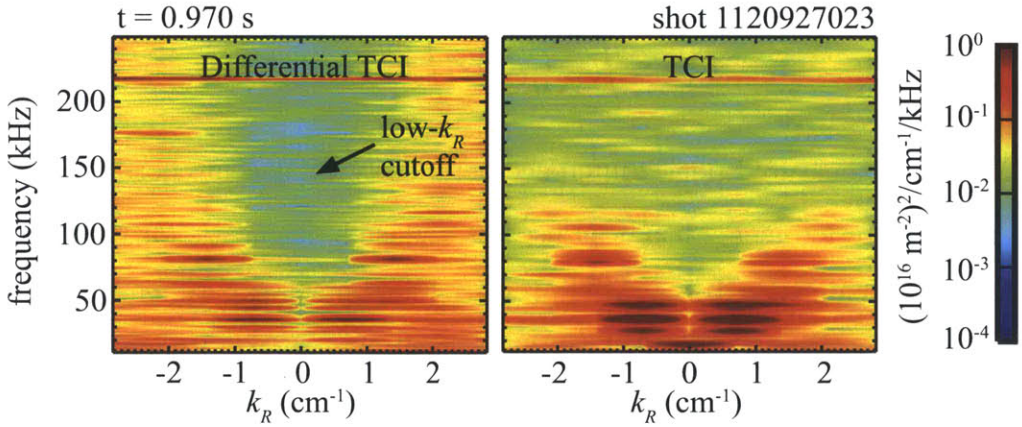

Figure B-1: Sample $S(f, k_R)$ spectrum from differential TCI compared to standard TCI system.

The differential interferometry system on Alcator C-Mod has not been characterized here, due to time and space limitations. Nevertheless, Figure B-2 shows quantitative data from the differential system. The black lines are the signals calculated from the differential system between the indicated chords. The gray lines are

calculated by subtracting the two standard interferometer signals from the indicated chords. It is clear that the differential measurement has much lower fluctuation levels. However, it is not clear whether the lower fluctuation levels are due to reduced vibrational effects, or simply because the differential system is less sensitive to (real) low-k_R fluctuations; these are equivalent explanations when the vibrational effects dominate the low-k_R response.

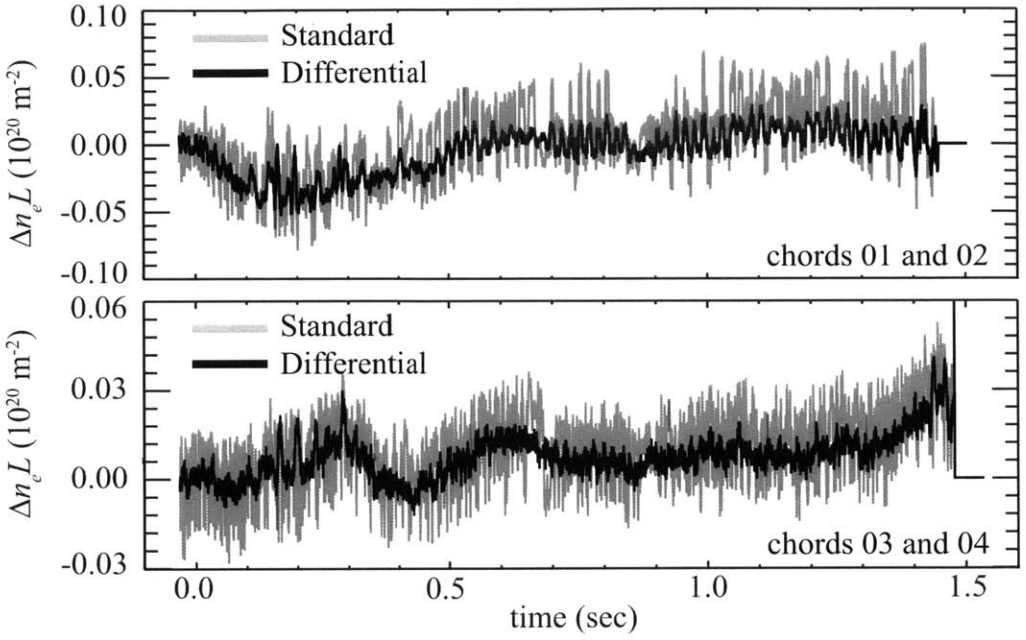

Figure B-2: Comparison between standard and differential measurements.

Appendix C

PCI Calibration Data

Table C.1 contains the "data-matched" phase-contrast imaging data used for the "Bessel model (matched to data)" curves in Figures 5-6, 5-7, and 5-15. This is the PCI wavenumber response data used in the analysis routines which computed the (filtered) quantitative fluctuation levels in Section 5.3. The data was provided to the author from a member of the PCI research group,[79] and is most likely not derived from the measurements shown in Figure 5-5; the measurements from which these data are derived were not available to the author. Only general features of the PCI calibration procedure are discussed in the literature,[43, 44, 75] so the procedure was described as best as possible in Section 5.1. For more information about the PCI calibration, the reader is encouraged to contact the PCI diagnostic research group at Alcator C-Mod.

Table C.1: PCI calibration data used for the quantitative comparisons between PCI and TCI in Chapter 5.

k_R (cm^{-1})	R_{PCI} (a.u.)	k_R (cm^{-1})	R_{PCI} (a.u.)	k_R (cm^{-1})	R_{PCI} (a.u.)
0.078125	0.00000000	6.796875	0.71925233	13.515625	0.15705991
0.156250	0.00000000	6.875000	0.71337677	13.593750	0.15093495
0.234375	2.1086513e-15	6.953125	0.70746104	13.671875	0.14484335
0.312500	6.8345222e-14	7.031250	0.70150597	13.750000	0.13878582
0.390625	1.7991723e-12	7.109375	0.69551240	13.828125	0.13276303
0.468750	3.8914874e-11	7.187500	0.68948118	13.906250	0.12677569
0.546875	6.9182043e-10	7.265625	0.68341314	13.984375	0.12082448
0.625000	1.0114278e-08	7.343750	0.67730913	14.062500	0.11491005

Table C.1: (continued)

k_R (cm^{-1})	R_{PCI} (a.u.)	k_R (cm^{-1})	R_{PCI} (a.u.)	k_R (cm^{-1})	R_{PCI} (a.u.)
0.703125	1.2168354e-07	7.421875	0.67117002	14.140625	0.10903307
0.781250	1.2057000e-06	7.500000	0.66499666	14.218750	0.10319421
0.859375	9.8490388e-06	7.578125	0.65878990	14.296875	0.09739410
0.937500	6.6410856e-05	7.656250	0.65255063	14.375000	0.09163339
1.015625	0.00037022	7.734375	0.64627969	14.453125	0.08591271
1.093750	0.00170974	7.812500	0.63997797	14.531250	0.08023267
1.171875	0.00655819	7.890625	0.63364635	14.609375	0.07459391
1.250000	0.02096559	7.968750	0.62728569	14.687500	0.06899701
1.328125	0.05611492	8.046875	0.62089689	14.765625	0.06344259
1.406250	0.12652005	8.125000	0.61448082	14.843750	0.05793123
1.484375	0.24230092	8.203125	0.60803838	14.921875	0.05246351
1.562500	0.39860579	8.281250	0.60157045	15.000000	0.04704000
1.640625	0.57178939	8.359375	0.59507792	15.078125	0.04166127
1.718750	0.72918573	8.437500	0.58856169	15.156250	0.03632788
1.796875	0.84636112	8.515625	0.58202265	15.234375	0.03104036
1.875000	0.91755066	8.593750	0.57546171	15.312500	0.02579925
1.953125	0.95244557	8.671875	0.56887975	15.390625	0.02060509
2.031250	0.96567073	8.750000	0.56227768	15.468750	0.01545839
2.109375	0.96874365	8.828125	0.55565641	15.546875	0.01035966
2.187500	0.96799683	8.906250	0.54901684	15.625000	0.00530941
2.265625	0.96605562	8.984375	0.54235986	15.703125	0.00030811
2.343750	0.96376811	9.062500	0.53568640	15.781250	0.00464375
2.421875	0.96135161	9.140625	0.52899735	15.859375	0.00954568
2.500000	0.95885094	9.218750	0.52229362	15.937500	0.01439725
2.578125	0.95627380	9.296875	0.51557612	16.015625	0.01919798
2.656250	0.95362156	9.375000	0.50884575	16.093750	0.02394744
2.734375	0.95089471	9.453125	0.50210343	16.171875	0.02864519
2.812500	0.94809364	9.531250	0.49535006	16.250000	0.03329081
2.890625	0.94521878	9.609375	0.48858656	16.328125	0.03788389
2.968750	0.94227054	9.687500	0.48181382	16.406250	0.04242402
3.046875	0.93924934	9.765625	0.47503276	16.484375	0.04691080
3.125000	0.93615564	9.843750	0.46824429	16.562500	0.05134386
3.203125	0.93298987	9.921875	0.46144930	16.640625	0.05572282
3.281250	0.92975250	10.000000	0.45464871	16.718750	0.06004732
3.359375	0.92644400	10.078125	0.44784342	16.796875	0.06431699
3.437500	0.92306484	10.156250	0.44103434	16.875000	0.06853150
3.515625	0.91961553	10.234375	0.43422236	16.953125	0.07269051
3.593750	0.91609656	10.312500	0.42740838	17.031250	0.07679371
3.671875	0.91250843	10.390625	0.42059331	17.109375	0.08084076
3.750000	0.90885168	10.468750	0.41377804	17.187500	0.08483138
3.828125	0.90512683	10.546875	0.40696347	17.265625	0.08876527
3.906250	0.90133441	10.625000	0.40015049	17.343750	0.09264215

Table C.1: (continued)

k_R (cm^{-1})	R_{PCI} (a.u.)	k_R (cm^{-1})	R_{PCI} (a.u.)	k_R (cm^{-1})	R_{PCI} (a.u.)
3.984375	0.89747499	10.703125	0.39333999	17.421875	0.09646174
4.062500	0.89354911	10.781250	0.38653286	17.500000	0.10022378
4.140625	0.88955735	10.859375	0.37972999	17.578125	0.10392802
4.218750	0.88550028	10.937500	0.37293226	17.656250	0.10757422
4.296875	0.88137849	11.015625	0.36614055	17.734375	0.11116215
4.375000	0.87719257	11.093750	0.35935574	17.812500	0.11469159
4.453125	0.87294313	11.171875	0.35257870	17.890625	0.11816232
4.531250	0.86863078	11.250000	0.34581031	17.968750	0.12157415
4.609375	0.86425614	11.328125	0.33905143	18.046875	0.12492689
4.687500	0.85981985	11.406250	0.33230294	18.125000	0.12822036
4.765625	0.85532253	11.484375	0.32556568	18.203125	0.13145438
4.843750	0.85076485	11.562500	0.31884053	18.281250	0.13462882
4.921875	0.84614744	11.640625	0.31212833	18.359375	0.13774350
5.000000	0.84147098	11.718750	0.30542992	18.437500	0.14079831
5.078125	0.83673615	11.796875	0.29874617	18.515625	0.14379311
5.156250	0.83194361	11.875000	0.29207791	18.593750	0.14672779
5.234375	0.82709405	11.953125	0.28542597	18.671875	0.14960223
5.312500	0.82218817	12.031250	0.27879119	18.750000	0.15241635
5.390625	0.81722668	12.109375	0.27217440	18.828125	0.15517006
5.468750	0.81221028	12.187500	0.26557642	18.906250	0.15786329
5.546875	0.80713969	12.265625	0.25899806	18.984375	0.16049597
5.625000	0.80201564	12.343750	0.25244015	19.062500	0.16306805
5.703125	0.79683885	12.421875	0.24590348	19.140625	0.16557948
5.781250	0.79161007	12.500000	0.23938886	19.218750	0.16803024
5.859375	0.78633004	12.578125	0.23289709	19.296875	0.17042029
5.937500	0.78099951	12.656250	0.22642895	19.375000	0.17274963
6.015625	0.77561924	12.734375	0.21998524	19.453125	0.17501826
6.093750	0.77019000	12.812500	0.21356673	19.531250	0.17722618
6.171875	0.76471256	12.890625	0.20717420	19.609375	0.17937342
6.250000	0.75918770	12.968750	0.20080841	19.687500	0.18145999
6.328125	0.75361619	13.046875	0.19447013	19.765625	0.18348594
6.406250	0.74799883	13.125000	0.18816011	19.843750	0.18545133
6.484375	0.74233642	13.203125	0.18187910	19.921875	0.18735620
6.562500	0.73662976	13.281250	0.17562785	20.000000	0.18920062
6.640625	0.73087964	13.359375	0.16940708	-	-
6.718750	0.72508690	13.437500	0.16321753	-	-

Bibliography

[1] J.H. Irby, E.S. Marmar, E. Sevillano, and S.M. Wolfe. Two-color interferometer system for Alcator C-MOD. *Rev. Sci. Instrum.*, 59:1568, 1988.

[2] C.P. Kasten, J.H. Irby, R. Murray, A.E. White, and D.C. Pace. A new interferometry-based electron density fluctuation diagnostic on Alcator C-Mod. *Rev. Sci. Instrum.*, 83:10E301, 2012.

[3] I.H. Hutchinson, H. Becker, P. Bonoli, N. Diatchenko, S. Fairfax, C. Fiore, R. Granetz, M. Greenwald, D. Gwinn, S. Hakkarainen, D. Humphreys, J. Irby, B. Lipschultz, E. Marmar, D.B. Montgomery, C. Park, R. Parker, N. Pierce, R. Pillsbury, M. Porkolab, J. Ramos, J. Rice, J. Schultz, D. Sigmar, F. Silva, Y. Takase, J. Terry, E. Thibeault, and S. Wolfe. The physics and engineering of Alcator C-MOD. Technical Report DOE/ET-51013-254, PFC/RR-88-11, Plasma Fusion Center, Massachusetts Institute of Technology, 1988.

[4] I. H. Hutchinson, R. Boivin, F. Bombarda, P. Bonoli, S. Fairfax, C. Fiore, J. Goetz, S. Golovato, R. Granetz, M. Greenwald, S. Horne, A. Hubbard, J. Irby, B. LaBombard, B. Lipschultz, E. Marmar, G. McCracken, M. Porkolab, J. Rice, J. Snipes, Y. Takase, J. Terry, S. Wolfe, C. Christensen, D. Garnier, M. Graf, T. Hsu, T. Luke, M. May, A. Niemczewski, G. Tinios, J. Schachter, , and J. Urbahn. First results from Alcator C-Mod. *Phys. Plasmas*, 1:1511, 1994.

[5] General Fusion. *http://www.generalfusion.com/magnetic_fusion.html.* 2010.

[6] F.F. Chen. *Introduction to Plasma Physics and Controlled Fusion Volume 1: Plasma Physics*, pages 30–34. Plenum Press, 1984.

[7] B.B. Kadomtsev and O.P. Pogutse. Trapped particles in toroidal magnetic systems. *Nucl. Fusion*, 11:67, 1971.

[8] A.J. Wootton, B.A. Carreras, H. Matsumoto, K. McGuire, W.A. Peebles, Ch.P. Ritz, P.W. Terry, and S.J. Szeben. Fluctuations and anomalous transport in tokamaks. *Phys. Fluids B*, 2(12), 1990.

[9] E.J. Doyle, W.A. Houlberg, Y. Kamada, V. Mukhovatov, T.H. Osborne, A. Polevoi, G. Bateman, J.W. Connor, J.G. Cordey, T. Fujita, X. Garbet, T.S. Hahm, L.D. Horton, A.E. Hubbard, F. Imbeaux, F. Jenko, J.E. Kinsey, Y. Kishimoto, J. Li, T.C. Luce, Y. Martin, M. Ossipenko, V. Parail, A. Peeters, T.L.

Rhodes, J.E. Rice, C.M. Roach, V. Rozhansky, F. Ryter, G. Saibene, R. Sartori, A.C.C. Sips, J.A. Snipes, M. Sugihara, E.J. Synakowski, H. Takenaga, T. Takizuka, K. Thomsen, M.R.Wade, H.R.Wilson, ITPA Transport Physics Topical Group, ITPA Confinement Database and Modeling Topical Group, and ITPA Pedestal and Edge Topical Group. Chapter 2: Plasma confinement and transport. *Nucl. Fusion*, 47, 2007.

[10] P.H. Rutherford and E.A. Frieman. Drift instabilities in general magnetic field configurations. *Phys. Fluids*, 11(3), 1968.

[11] E.A. Frieman and L. Chen. Nonlinear gyrokinetic equations for lowfrequency electromagnetic waves in general plasma equilibria. *Phys. Fluids*, 25:502, 1982.

[12] J. Candy and R.E. Waltz. An Eulerian gyrokinetic-Maxwell solver. *J. Comput. Phys.*, 186:545, 2003.

[13] D.G. Whyte, A.E. Hubbard, J.W. Hughes, B. Lipschultz, J.E. Rice, E.S. Marmar, M. Greenwald, I. Cziegler, A. Dominguez, T. Golfinopoulos, N. Howard, L. Lin, R.M. McDermott, M. Porkolab, M.L. Reinke, J. Terry, N. Tsujii, S. Wolfe, S. Wukitch, Y. Lin, and the Alcator C-Mod Team. I-mode: an H-mode energy confinement regime with L-mode particle transport in Alcator C-Mod. *Nucl. Fusion*, 50(10):105005, 2010.

[14] M. Keilhacker, G. Becker, K. Bernhardi, A. Eberhagen, M. ElShaer, G. Fubmann, O. Gehre, J. Gernhardt, G.v. Gierke, E. Glock, G. Haas, F. Karger, S. Kissel, O. Klüber, M. Kornherr, K. Lackner, G. Lisitano, G.G. Lister, J. Massig, H.-M. Mayer, K. McCormick, D. Meisel, E. Meservey, E.R. Müller, H. Murmann, H. Niedermeyer, W. Poschenrieder, H. Rapp, B. Richter adn H. Röhr, F. Ryter, F. Schneider, G. Siller, P. Smeulders, F. Söldner, E. Speth, A. Stäbler, K. Steinmetz, K.-H. Steuer, Z. Szymanski, G. Venus, O. Vollmer, and F. Wagner. Confinement studies in L and H-type ASDEX discharges. *Plasma Phys. Control. Fusion*, 26(1A):49, 1984.

[15] M. Greenwald, R. Boivin, P. Bonoli, R. Budny, C. Fiore, J. Goetz, R. Granetz, A. Hubbard, I. Hutchinson, J. Irby, B. LaBombard, Y. Lin, B. Lipschultz, E. Marmar, A. Mazurenko, D. Mossessian, T. Sunn Pedersen, C.S. Pitcher, M. Porkolab, J. Rice, W. Rowan, J. Snipes, G. Schilling, Y. Takase, J. Terry, S. Wolfe, J. Weaver, B. Welch, and S. Wukitch. Characterization of enhanced D_α high-confinement modes in Alcator C-Mod. *Phys. Plasmas*, 6(5), 1999.

[16] P. Koert, S.J. Wukitch, W.K. Beck, Y. Lin, J. Doody, and N.P. Mucic. New Alcator C-Mod rotated 10° 4-strap ICRF antenna. Technical Report PSFC/JA-09-17, Plasma Science and Fusion Center, Massachusetts Institute of Technology, 2009.

[17] M. Porkolab, C. Fiore, M. Greenwald, J.C. Hosea, A. Hubbard, I. Hutchinson, J. Irby, E. Nelson-Melby, E. Marmar, C.K. Phillips, J. Reardon, J. Rice,

G. Schilling, J. Terry, S. Wolfe, S. Wukitch, J.R. Wilson, and the Alcator Team. ICRF heating in Alcator C-Mod: present status and future prospects. Technical Report PSFC/JA-99-18, Plasma Science and Fusion Center, Massachusetts Institute of Technology, 1999.

[18] Y. Lin. *Experimental application and numerical study of reflectometry in the Alcator C-Mod tokamak.* PhD thesis, Massachusetts Institute of Technology, Cambridge, MA, 2001.

[19] J.W. Heard, C. Watts, R.F. Gandy, P.E. Phillips, G. Cima, R. Chatterjee, A. Blair, A. Hubbard, C.W. Domier, and N.C. Luhmann, Jr. High resolution electron cyclotron emission temperature profile and fluctuation diagnostic for Alcator C-Mod. *Rev. Sci. Instrum.*, 70(1), 1999.

[20] C. Sung, A.E. White, J.H. Irby, R. Leccacorvi, R. Vieira, C.Y. Oi, W.A. Peebles, and X. Nguyen. Design of a correlation electron cyclotron emission diagnostic for Alcator C-Mod. *Rev. Sci. Instrum.*, 83:10E311, 2012.

[21] A. Ince-Cushman, J.E. Rice, M. Bitter, M.L. Reinke, K.W. Hill, M.F. Gu, E. Eikenberry, Ch. Broennimann, S. Scott, Y. Podpaly, S.G. Lee, and E.S. Marmar. Spatially resolved high resolution x-ray spectroscopy for magnetically confined fusion plasmas (invited). *Rev. Sci. Instrum.*, 79:10E302, 2008.

[22] M. L. Reinke, Y. A. Podpaly, M. Bitter, I. H. Hutchinson, J. E. Rice, L. Delgado-Aparicio, C. Gao, M. Greenwald, K. Hill, N. T. Howard, A. Hubbard, J. W. Hughes, N. Pablant, A. E. White, and S. M. Wolfe. X-ray imaging crystal spectroscopy for use in plasma transport research. *Rev. Sci. Instrum.*, 83(11):113504, 2012.

[23] J.W. Hughes, D. Mossessian, K. Zhurovich, M. DeMaria, K. Jensen, and A. Hubbard. Thomson scattering upgrades on Alcator C-Mod. *Rev. Sci. Instrum.*, 74(3):1667, 2003.

[24] R. Nazikian and L. E. Sharp. CO_2 laser scintillation interferometer for the measurement of density fluctuations in plasma confinement devices. *Rev. Sci. Instrum.*, 58(11):2086–2091, 1987.

[25] D.R. Baker and S.T. Lee. Dual laser interferometer for plasma density measurements on large tokamaks. *Rev. Sci. Instrum.*, 49:919, 1978.

[26] D.R. Baker. CO_2 interferometer operation in Doublet III. *Rev. Sci. Instrum.*, 51:1304, 1980.

[27] T.N. Carlstrom, D.R. Ahlgren, and J. Crosbie. Real-time, vibration-compensated CO_2 interferometer operation on the DIII-D tokamak. *Rev. Sci. Instrum.*, 59(7):1063, 1988.

[28] Y. Kawano, A. Nagashima, S. Ishida, T. Fukuda, and T. Matoba. CO2 laser interferometer for electron density measurement in JT60U tokamak. *Rev. Sci. Instrum.*, 63:4971, 1992.

[29] A. Canton, P. Innocente, S. Martini, L. Tasinato, and O. Tudisco. Spatially scanned two-color mid-infrared interferometer for FTU. *Rev. Sci. Instrum.*, 72:1085, 2001.

[30] O. Gornostaeva, B.H. Deng, E. Garate, H. Gota, J. Kinley, J. Schroeder, and M. Tuszewski. Two-color CO_2/HeNe laser interferometer for C-2 experiment. *Rev. Sci. Instrum.*, 81:10D516, 2010.

[31] P. Acedo, H. Lamela, M. Sánchez, T. Estrada, and J. Sánchez. CO2 (λm = 10.6μm) He-Ne (λc = 633nm) two-color laser interferometry for low and medium electron density measurements in the TJ-II stellarator. *Rev. Sci. Instrum.*, 75:4671, 2004.

[32] K. Tanaka, A.L. Sanin, L.N. Vyacheslavov, T. Akiyama, K. Kawahata, T. Tokuzawa, Y. Ito, and S. Okajima. Precise density profile measurements by using a two color YAG/CO_2 laser imaging interferometer on LHD. *Rev. Sci. Instrum.*, 75:3429, 2004.

[33] P. Innocente and S. Martini. A two color multichord infrared interferometer for RFX. *Rev. Sci. Instrum.*, 63:4996, 1992.

[34] P. Innocente, S. Martini, and Ch. Ferrer Roca. An infrared vibration compensated interferometer for the MST experiment. *Rev. Sci. Instrum.*, 63:4999, 1992.

[35] P. Kornejew, M. Hirsch, T. Bindermann, A. Dinklage, H. Dreier, and H.J. Hartfub. Design of multichannel laser interferometry for W7-X. *Rev. Sci. Instrum.*, 77:10F128, 2006.

[36] K. Kawahata, T. Akiyama, R. Pavlichenko, K. Tanaka, T. Tokuzawa, Y. Ito, S. Okajima, K. Nakayama, and K. Wood. Two-color far infrared laser interferometer. *Rev. Sci. Instrum.*, 77:10F132, 2006.

[37] G. Braithwaite, N. Gottardi, G. Magyar, J. O'Rourke, J. Ryan, and D. Véron. JET polariinterferometer. *Rev. Sci. Instrum.*, 60:2825, 1989.

[38] R. Prentice, T. Edlington, R.T.C. Smith, D.L. Trotman, R.J. Wylde, and P. Zimmermann. A two color mm-wave interferometer for the JET divertor. *Rev. Sci. Instrum.*, 66:1154, 1995.

[39] H. Takenaga, T. Fukuda, S. Sakurai, N. Hosogane, K. Kodama, and K. Masaki. Versatile millimeter-wave interferometer with two frequencies in the divertor region of JT-60U. *Rev. Sci. Instrum.*, 69:3181, 1998.

[40] Y. Kawano, A. Nagashima, T. Hatae, and S. Gunji. Dual CO2 laser interferometer with a wavelength combination of 10.6 and 9.27 μm for electron density measurement on large tokamaks. *Rev. Sci. Instrum.*, 67:1520, 1996.

[41] T. Lehecka, W.A. Peebles, N.C. Luhmann Jr., and T.N. Carlstrom. Two-color interferometry for fusion plasma diagnostics. *Rev. Sci. Instrum.*, 59(8):1580, 1988.

[42] T.N. Carlstrom and R.T. Snider. Prototype tests of a combined CO2 laser interferometer/polarimeter for ITER (abstract). *Rev. Sci. Instrum.*, 70:694, 1999.

[43] S. Coda. *An Experimental Study of Turbulence by Phase-Contrast Imaging in the DIII-D Tokamak.* PhD thesis, Massachusetts Institute of Technology, 1997.

[44] A. Mazurenko. *Phase Contrast Imaging on the Alcator C-Mod tokamak.* PhD thesis, Massachusetts Institute of Technology, 2001.

[45] Y. Lin, S. Wukitch, A. Parisot, J.C. Wright, N. Basse, P. Bonoli, E. Edlund, L. Lin, M. Porkolab, G. Schilling, and P. Phillips. Observation and modelling of ion cyclotron range of frequencies waves in the mode conversion region of Alcator C-Mod. *Plasma Phys. Control. Fusion*, 47(8):1207, 2005.

[46] E. Nelson-Melby, M. Porkolab, P. T. Bonoli, Y. Lin, A. Mazurenko, and S. J. Wukitch. Experimental observations of mode-converted ion cyclotron waves in a tokamak plasma by phase contrast imaging. *Phys. Rev. Lett.*, 90:155004, Apr 2003.

[47] M. Porkolab, J.C. Rost, N. Basse, J. Dorris, E. Edlund, L. Lin, Y. Lin, and S. Wukitch. Phase contrast imaging of waves and instabilities in high temperature magnetized fusion plasmas. *Plasma Phys. Control. Fusion*, 51:065006, 2009.

[48] A. Mazurenko, M. Porkolab, D. Mossessian, J.A. Snipes, X.Q. Xu, and W.M. Nevins. Experimental and theoretical study of quasicoherent fluctuations in enhanced D_α plasmas in the Alcator C-Mod tokamak. *Phys. Rev. Lett.*, 89(22):225004, 2002.

[49] Y. Lin, J.E. Rice, S.J. Wukitch, M.J. Greenwald, A.E. Hubbard, A. Ince-Cushman, L. Lin, E.S. Marmar, M. Porkolab, M.L. Reinke, N. Tsujii, J.C. Wright, and Alcator C-Mod Team. Observation of ion cyclotron range of frequencies mode conversion plasma flow drive on Alcator C-Mod. *Phys. Plasmas*, 16:056102, 2009.

[50] N. Tsujii, M. Porkolab, P.T. Bonoli, J.C. Wright, S.J. Wukitch, E.F. Jaeger, and R.W. Harvey. ICRF mode conversion studies with phase contrast imaging and comparisons with full-wave simulations. *AIP Conf. Proc.*, 1406:293, 2011.

[51] N. Tsujii, M. Porkolab, P. T. Bonoli, Y. Lin, J. C. Wright, S. J. Wukitch, E. F. Jaeger, D. L. Green, and R. W. Harvey. Measurements of ion cyclotron

range of frequencies mode converted wave intensity with phase contrast imaging in Alcator C-Mod and comparison with full-wave simulations. *Phys. Plasmas*, 19(8):082508, 2012.

[52] N.P. Basse, E.M. Edlund, D.R. Ernst, C.L. Fiore, M.J. Greenwald, A.E. Hubbard, J.W. Hughes, J.H. Irby, L. Lin, Y. Lin, E.S. Marmar, D.A. Mossessian, M. Porkolab, J.E. Rice, J.A. Snipes, J.A. Stillerman, J.L. Terry, S.M. Wolfe, S.J. Wukitch, K. Zhurovich, G.J. Kramer, and D.R. Mikkelson. Characterization of core and edge turbulence in L- and enhanced D_α H-mode Alcator C-Mod plasmas. *Phys. Plasmas*, 12(5):2512, 2005.

[53] L. Lin, M. Porkolab, E.M. Edlund, J.C. Rost, M. Greenwald, N. Tsujii, J. Candy, R.E. Waltz, and D.R. Mikkelsen. Studies of turbulence and transport in Alcator C-Mod ohmic plasmas with phase contrast imaging and comparisons with gyrokinetic simulations. *Plasma Phys. Control. Fusion*, 51:065006, 2009.

[54] L. Lin, M. Porkolab, E.M. Edlund, J.C. Rost, C.L. Fiore, M. Greenwald, Y. Lin, D.R. Mikkelsen, N. Tsujii, and S.J. Wukitch. Studies of turbulence and transport in Alcator C-Mod H-mode plasmas with phase contrast imaging and comparisons with GYRO. *Phys. Plasmas*, 16:012502, 2009.

[55] M. Porkolab, J. Dorris, P. Ennever, C. Fiore, M. Greenwald, A. Hubbard, Y. Ma, E. Marmar, Y. Podpaly, M. L. Reinke, J. E. Rice, J. C. Rost, N. Tsujii, D. Ernst, J. Candy, G. M. Staebler, and R. E. Waltz. Transport and turbulence studies in the linear ohmic confinement regime in Alcator C-Mod. *Plasma Phys. Control. Fusion*, 54(12):124029, 2012.

[56] P.W. Terry. Suppression of turbulence and transport by sheared flow. *Rev. Mod. Phys.*, 72:109, Jan 2000.

[57] Y. Lin, J.E. Rice, S.J. Wukitch, M.J. Greenwald, A.E. Hubbard, A. Ince-Cushman, L. Lin, M. Porkolab, M.L. Reinke, and N. Tsujii. Observation of ion-cyclotron-frequency mode-conversion flow drive in tokamak plasmas. *Phys. Rev. Lett.*, 101:235002, 2008.

[58] Y. Lin, J.E. Rice, S.J. Wukitch, M.L. Reinke, M.J. Greenwald, A.E. Hubbard, E.S. Marmar, Y. Podpaly, M. Porkolab, N. Tsujii, and the Alcator C-Mod team. ICRF mode conversion flow drive on Alcator C-Mod. *Nucl. Fusion*, 51:063002, 2011.

[59] F.W. Perkins. Heating tokamaks via the ion-cyclotron and ion-ion hybrid resonances. *Nucl. Fusion*, 17(6):1197, 1977.

[60] P.L. Colestock and R.J. Kashuba. The theory of mode conversion and wave damping near the ion cyclotron frequency. *Nucl. Fusion*, 23(6):763, 1983.

[61] P.T. Bonoli, P. O'Shea, M. Brambilla, S.N. Golovato, A.E. Hubbard, M. Porkolab, Y. Takase, R.L. Boivin, F. Bombarda, C. Christensen, C.L. Fiore, D. Garnier, J. Goetz, R. Granetz, M. Greenwald, S.F. Horne, I.H. Hutchinson, J. Irby, D. Jablonski, B. LaBombard, B. Lipschultz, E. Marmar, M. May, A. Mazurenko, G. McCracken, R. Nachtrieb, A. Niemczewski, H. Ohkawa, D.A. Pappas, J. Reardon, J. Rice, C. Rost, J. Schachter, J.A. Snipes, P. Stek, K. Takase, J. Terry, Y. Wang, R.L. Watterson, B. Welch, and S.M. Wolfe. Electron heating via mode converted ion bernstein waves in the Alcator C-Mod tokamak. *Phys. Plasmas*, 4:1774, 1997.

[62] A. Parisot. *Mode Conversion Current Drive Experiments on Alcator C-Mod.* PhD thesis, Massachusetts Institute of Technology, 2007.

[63] T.H. Stix and D.G. Swanson. Propagation and mode conversion for waves in nonuniform plasmas. Technical Report PPPL-1903, Princeton Plasma Physics Laboratory, 1982.

[64] N.J. Fisch. Theory of current drive in plasmas. *Rev. Mod. Phys.*, 59(1), 1987.

[65] Y. Lin, S. Wukitch, P. Bonoli, E. Nelson-Melby, M. Porkolab, J.C. Wright, N. Basse, A.E. Hubbard, J. Irby, L. Lin, E.S. Marmar, A. Mazurenko, D. Mossessian, A. Parisot, J. Rice, and S. Wolfe. Investigation of ion cyclotron range of frequencies mode conversion at the ion-ion hybrid layer in Alcator C-Mod. *Phys. Plasmas*, 11:052466, 2004.

[66] Y. Lin, M.L. Reinke, J.E. Rice, S.J. Wukitch, and R. Granetz. ICRF mode conversion flow drive experiments on Alcator C-Mod. *AIP Conf. Proc.*, 1406:285, 2011.

[67] Y. Lin, S. Wukitch, M. Reinke, S. Wolfe, R. Granetz, J. Rice, A. Hubbard, K. Liao, W. Rowan, N. Tsujii, P. Ennever, C. Kasten, and A. White. Study of ICRF mode conversion flow drive and NTMs in high performance I-mode plasmas. *Alcator C-Mod Mini-Proposal*, 721, 2012.

[68] I.H. Hutchinson. *Principles of Plasma Diagnostics.* Cambridge University Press, second edition, 2002.

[69] F.F. Chen. *Introduction to Plasma Physics and Controlled Fusion Volume 1: Plasma Physics*, pages 104, 122–126. Plenum Press, 1984.

[70] B.W. Rice. *Poloidal Magnetic Field Measurements on the Microwave Tokamak Experiment Using Far-Infrared Interferometry.* PhD thesis, University of California at Davis, 1992.

[71] T. Luke. *Measurement of Particle Transport Coefficients on Alcator C-Mod.* PhD thesis, Massachusetts Institute of Technology, Cambridge, MA, 1994.

[72] M.A. Van Zeeland and T.N. Carlstrom. Phase error correction method for a vibration compensated interferometer. *Rev. Sci. Instrum.*, 75(10):3423, 2004.

[73] Ch.P. Ritz, E.J. Powers, T.L. Rhodes, R.D. Bengtson, K.W. Gengle, Hong Lin, P.E. Phillips, and A.J. Wootton. Advanced plasma fluctuation analysis techniques and their impact on fusion research. *Rev. Sci. Instrum*, 59(8):1739, 1988.

[74] R. V. Bravenec and W. M. Nevins. System for simulating fluctuation diagnostics for application to turbulence computations. *Rev. Sci. Instrum.*, 77(1):015101, 2006.

[75] L. Lin. *Turbulence and Transport Studies with Phase Contrast Imaging in the Alcator C-Mod tokamak and Comparisons with Gyrokinetic Simulations.* PhD thesis, Massachusetts Institute of Technology, 2009.

[76] J.C. Rost, L. Lin, and M. Porkolab. Development of a synthetic phase contrast imaging diagnostic. *Phys. Plasmas*, 17:062506, 2010.

[77] R.V. Bravenec and A.J. Wootton. Effects of limited spatial resolution on fluctuation measurements. *Rev. Sci. Instrum.*, 66(1):802, 1995.

[78] Naoto Tsujii. Phase Contrast Imaging on Alcator C-Mod. *Alcator C-Mod internal report*, 2012.

[79] P. Ennever. Private communication, January 17, 2013.

[80] J.E. Rice, J.W. Hughes, P.H. Diamond, Y. Kosuga, Y.A. Podpaly, M.L. Reinke, M.J. Greenwald, Ö.D. Gürcan, T.S. Hahm, A.E. Hubbard, E.S. Marmar, C.J. McDevitt, and D.G. Whyte. Edge temperature gradient as intrinsic rotation drive in Alcator C-Mod tokamak plasmas. *Phys. Rev. Lett.*, 106:215001, May 2011.

[81] M.T. Beidler and P.A. Cassak. Model for incomplete reconnection in sawtooth crashes. *Phys. Rev. Lett.*, 107:255002, December 2011.

[82] L. Lin, E. M. Edlund, M. Porkolab, Y. Lin, and S. J. Wukitch. Vertical localization of phase contrast imaging diagnostic in Alcator C-Mod. *Rev. Sci. Instrum.*, 77(10):10E918, 2006.

[83] J.P.H.E. Ongena, M. Evrard, and D. McCune. Numerical transport codes. *Trans. Fusion Sci. Technol.*, 49, 2006.

[84] G.R. Tynan, A. Fujisawa, and G. McKee. A review of experimental drift turbulence studies. *Plasma Phys. Control. Fusion*, 51:113001, 2009.

[85] J.H. Irby, R. Murray, P. Acedo, and H. Lamela. A two-color interferometer using a frequency doubled diode pumped laser for electron density measurements. *Rev. Sci. Instrum.*, 70:699, 1999.

[86] W.X. Ding, D.L. Brower, B.H. Deng, and T. Yates. Electron density measurement by differential interferometry. *Rev. Sci. Instrum.*, 77:10F105, 2006.

[87] L. Lin, W.X. Ding, D.L. Brower, W.F. Bergerson, and T.F. Yates. Differential interferometry for measurement of density fluctuations and fluctuation-induced transport. *Rev. Sci. Instrum.*, 81:10D509, 2010.

[88] C.B. Deng and D.L. Brower. Core density gradient fluctuation measurement by differential interferometry in the helically symmetric experiment stellarator. *Rev. Sci. Instrum.*, 83:10E308, 2012.

[89] W.X. Ding, D.L. Brower, and T. Yates. Measurement of magnetic fluctuation-induced particle flux. *Rev. Sci. Instrum.*, 79:10E701, 2008.